

Doctoral Dissertation

**Ridging Resistance and Formability in the  
AISI 430 Transformable Ferritic Stainless  
Steel**

Javad Mola

Materials Design Laboratory

Graduate Institute of Ferrous Technology

Pohang University of Science and Technology

2011

# **Ridging Resistance and Formability in the AISI 430 Transformable Ferritic Stainless Steel**



# **Ridging Resistance and Formability in the AISI 430 Transformable Ferritic Stainless Steel**

by

Javad Mola

Materials Design Laboratory

Graduate Institute of Ferrous Technology

Pohang University of Science and Technology

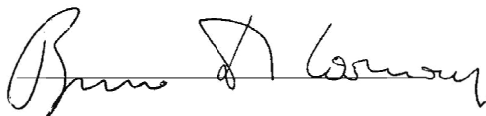
A dissertation submitted to the faculty of Pohang University of Science and Technology in partial fulfillments of the requirements for the degree of Doctor of Philosophy in the Materials Design Program of Graduate Institute of Ferrous Technology.

Pohang, South Korea

October 18<sup>th</sup>, 2011

Approved by

Professor Bruno C. De Cooman

A handwritten signature in black ink, appearing to read 'Bruno C. De Cooman', written over a horizontal line.

Major Advisor

# Ridging Resistance and Formability in the AISI 430 Transformable Ferritic Stainless Steel

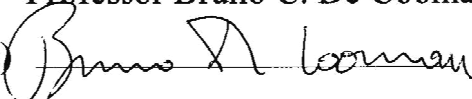
Javad Mola

This dissertation is submitted for the degree of Doctor of Philosophy at the Graduate Institute of Ferrous Technology of Pohang University of Science and Technology. The research reported herein was approved by the committee of Thesis Appraisal.

October 18<sup>th</sup>, 2011

## Dissertation Review Committee

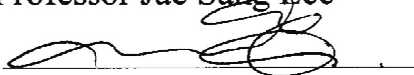
Chairman: Professor Bruno C. De Cooman

(Signature) 

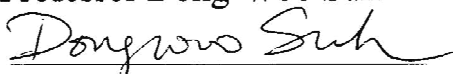
Member: Professor Sung-Joon Kim

(Signature) 

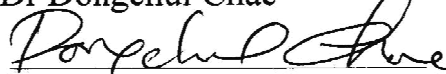
Member: Professor Jae Sang Lee

(Signature) 

Member: Professor Dong-Woo Suh

(Signature) 

Member: Dr Dongchul Chae

(Signature) 

DFT                      Javad Mola  
20080965              Ridging Resistance and Formability in the AISI 430 Transformable  
                                 Ferritic Stainless Steel  
                                 Graduate Institute of Ferrous Technology, 2011, 170 pages  
                                 Advisor: Professor Bruno C. De Cooman  
                                 Text in English

## ABSTRACT

Ferritic stainless steel sheets are commonly used in applications involving cold forming operations such as deep drawing to reach the final shape. Therefore, they are required to have good forming characteristics. Furthermore, they must maintain a good surface smoothness in order to remain visually appealing. Occurrence of a surface defect termed ridging during cold forming operations of ferritic stainless steel sheets is one of the factors restricting the use of this family of stainless steels in certain applications. Parts having undergone severe ridging need an extra polishing step which adds to their manufacturing cost.

The present work primarily aimed at achieving an acceptable combination of ridging resistance and formability in the AISI 430 transformable ferritic stainless steel. For this, initially three different compositional variants of the AISI 430 were analyzed and differences in their microstructural evolution, which is of relevance to the ridging resistance, were studied. Hot rolled strips of the three compositions were subsequently cold rolled with and without the standard batch annealing step to see the influence of eliminating the batch annealing step on the ridging resistance and formability which is the subject of chapter 5. Cold rolling of unannealed hot strips which contained a small fraction of  $\alpha'$  martensite was found to be associated with an enhanced ridging resistance but a lower r-value. The composition dependence of the ridging resistance was mainly justified based on the austenite fraction and the evolution of austenite fraction during hot rolling.

Based on the observation of an enhanced ridging resistance in the presence of a small fraction of  $\alpha'$  during cold rolling (chapter 5), chapter 6 deals with the effect of deliberate introduction of approximately 15% and 35% fresh  $\alpha'$  martensite in the hot rolled strip by annealing at two different intercritical annealing temperatures. The

ridging resistance was found to increase with the  $\alpha'$  fraction so that the hot strip containing 35%  $\alpha'$  was almost ridging-free. Nevertheless, the r-value which can be used as a measure of formability was not satisfactory.

Although the presence of  $\alpha'$  martensite was found to be beneficial to the ridging resistance, it must eventually transform to ferrite to obtain fully ferritic sheets. Chapter 7 discusses the thermal restoration mechanisms (recrystallization and recovery) in the cold rolled sheets containing  $\alpha'$  martensite.

Due to the observation of a high ridging resistance but a low r-value in the single step cold rolled hot strips containing  $\alpha'$ , double step cold rolling with an intermediate annealing step of  $\alpha'$ -containing hot strips was performed in order to see how the ridging resistance and the formability are influenced. As reported in chapter 8, double step cold rolling improved the r-values of the  $\alpha'$ -containing microstructure by an amount proportional to the intermediate annealing time.

Chapter 9 introduces a novel method to stabilize austenite in the AISI 430 grade, a concept which can be extended to a variety of other ferritic and martensitic grades as well. The quenching and partitioning (Q&P) processing, formerly applied to certain Advanced High Strength Steel (AHSS) grades only, is shown to be ideally suitable for the stainless steels. It is based on quenching the intercritical austenite to a temperature below the martensite start temperature in order to martensitically transform a controlled fraction of the high temperature austenite and obtain a smaller fraction of austenite to which the interstitial atoms C and N can diffuse from the supersaturated  $\alpha'$ . The austenite enrichment with C and N reduces the martensite start temperature of the remaining austenite, stabilizing it at room temperature. The presence of austenite can bring about the Transformation Induced Plasticity (TRIP) effect and have other possible implications for the mechanical properties improvement.

# CONTENTS

<b>I. Introduction to Ferritic Stainless Steels</b>	<b>1</b>
1.1. Microstructure and Constitution	1
1.2. Properties and Applications	2
1.3. Ridging	3
1.4. References	6
<b>II. Experimental Procedure</b>	<b>10</b>
2.1. Dilatometry	10
2.2. Scanning Electron Microscopy (SEM)	10
2.3. Transmission Electron Microscopy (TEM)	11
2.4. Electron Probe Micro-Analysis (EPMA)	11
2.5. Tensile Test	11
2.6. Ridging Resistance by Profilometry	13
<b>III. Alloy System and Processing Technology</b>	<b>16</b>
3.1. Material	16
3.2. Conventional Production Technology of AISI 430	19
3.3. References	25
<b>IV. Anisotropic Dimensional Change in Rough Rolled Bars</b>	<b>27</b>
4.1. Introduction	28
4.2. Experimental procedure	31
4.3. Results and Discussion	33
4.3.1. Phase fractions: Thermo-Calc vs. image analysis	33
4.3.2. Dilatometric phase fraction analysis	35
4.3.3. CTE phase fraction analysis	39
4.3.4. Martensite dilatation phase fraction analysis	43
4.3.5. Conversion of the dilatometry-based results into phase fractions	48
4.4. Conclusions	52
4.5. References	53

<b>V. Cold Rolling of Unannealed Hot Strips</b>	<b>57</b>
5.1. Introduction	57
5.2. Experimental Procedure	57
5.3. Results	60
5.4. Discussion	68
5.4.1. The $\gamma$ -Phase Fraction Evolution	68
5.4.2. Texture Bands Observation	79
5.4.3. Effect of the Processing Route on the Ridging Resistance	80
5.4.4. Effect of the Composition on the Ridging Resistance	80
5.4.5. Alloy Design for a Reduced Ridging	84
5.5. Correlation between the r-value and texture	86
5.6. Conclusions	90
5.7. References	91
<b>VI. Cold Rolling of <math>\alpha+\alpha'</math> Dual-Phase Microstructure</b>	<b>96</b>
6.1. Introduction	96
6.2. Experimental Procedure	96
6.3. Results and Discussion	98
6.3.1. Ridging Resistance	99
6.3.2. r-value	105
6.4. Conclusions	107
<b>VII. Thermal Restoration Mechanisms in Fully Ferritic and Dual-Phase (<math>\alpha+\alpha'</math>) Microstructures</b>	<b>109</b>
7.1. Introduction	109
7.2. Experimental Procedure	110
7.3. Results and Discussion	111
7.4. Conclusions	121
7.5. References	121

<b>VIII. Recrystallization Behavior in Fully Ferritic and Dual-Phase (<math>\alpha+\alpha'</math>) Microstructures</b>	<b>124</b>
8.1. Introduction	124
8.2. Experimental Procedure	124
8.3. Results and Discussion	126
8.4. Conclusions	137
8.5. References	138
<b>IX. Quenching and Partitioning (Q&amp;P) Processing of AISI 430</b>	<b>141</b>
9.1. Introduction	141
9.2. Experimental Procedure	142
9.3. Results and Discussion	143
9.4. Conclusions	150
9.5. References	150
<b>X. General Conclusions</b>	<b>154</b>
<b>Appendix</b>	<b>157</b>
<b>Acknowledgements</b>	<b>168</b>
<b>Publications</b>	<b>169</b>
<b>Curriculum Vitae</b>	<b>170</b>

# Chapter I

## Introduction to Ferritic Stainless Steels

### 1.1. Microstructure and Constitution

Ferritic stainless steels are iron-base alloys which contain a minimum of approximately 11% Cr and possess a fully ferritic matrix in the final form. This requires maintaining the ratio of ferrite stabilizing elements to austenite stabilizers high enough so that a fully ferritic matrix can be achieved at the final annealing temperature. Ferritic stainless steels can be classified in two large groups of transformable and non-transformable grades depending on whether or not the  $\alpha \leftrightarrow \gamma$  transformation takes place during the thermo-mechanical processing. Cr, C, and N are the main alloying elements controlling microstructure in the ferritic stainless steels. Fig. 1.1 demonstrates the effect of C on the equilibrium phase diagram of the Fe-Cr system. In the absence of C, austenite does not form in Fe-Cr alloys containing more than about 13.5% Cr. In the presence of 500 ppm of C, however, the  $\alpha + \gamma$  dual phase region is extended so that the transformation takes place in alloys containing up to about 19%Cr. Presence of austenite prevents the excessive grain growth during high temperature processing of ferrite. Besides, its transformation to martensite and the subsequent recovery/recrystallization of martensite is another grain refinement mechanism in the ferritic stainless steels.



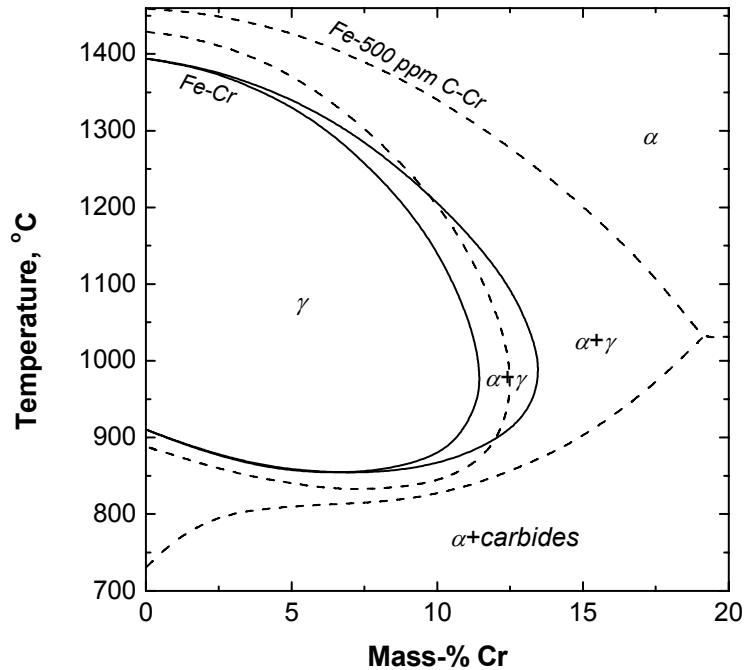


**Fig. 1.1.** Equilibrium Fe-Cr binary phase diagram and Fe-0.05C-Cr pseudo-binary phase diagram according to Thermo-Calc with a TCFE6 database.

Unless a material has good corrosion resistance and ductility in the as-welded condition, its usefulness as a material of construction is severely limited. In ferritic stainless steels, the amount of interstitial atoms C and N is of primary importance to weldability. In low Cr ferritic grades, high C and N levels can lead to intergranular corrosion after welding. In ferritic grades of higher Cr, on the other hand, loss of ductility in the as-welded parts is the primary concern when C and N levels are high [1]. To improve the weldability, C and N are sometimes stabilized with strong carbide and nitride formers such as Ti and Nb.

## 1.2. Properties and Applications

Compared to austenitic stainless steels, ferritic grades show a higher resistance to stress-corrosion cracking and are more cost-effective than the Ni-bearing austenitic stainless steels, whose price is largely controlled by the price of Ni. Nevertheless, factors such as susceptibility to embrittlement, notch sensitivity, poor weldability and

lack of the ductility characteristic of austenitic stainless steels have been historically regarded as drawbacks of this group of stainless steels [1]. Recent technological advances in the steelmaking processes, however, have made it possible to produce stainless steels with lower interstitial levels and have paved the way for the increased popularity of this family of stainless steels. Physical properties such as magnetism, better dimensional stability (due to a lower coefficient of thermal expansion), and higher heat conductivity compared to the austenitic grades are some additional factors which favor the use of the ferritic grades in certain applications.

Ferritic stainless steels have been primarily used in the construction of automobile exhaust systems and washing machine drums [2]. Interior and exterior trim applications such as sinks and sink rims, appliance trims, roofing, range hoods and restaurant equipments are some other areas in which the ferritics have been commonly used [3].

### **1.3. Ridging**

Ridging or roping is the formation of corrugations lying parallel to the rolling direction (RD) at the surface of sheets during forming operations. It is a common surface defect in ferritic stainless steels which makes them visually unappealing. This calls for polishing operations and adds to the manufacturing cost of ferritic stainless steels.

At present, there are two main theories to account for the occurrence of ridging in ferritic stainless steels. The first theory relates ridging to the presence of chemical segregation bands of Cr and C parallel to the RD [4-5]. Such compositional bands are likely to form during two-phase ( $\alpha+\gamma$ ) hot rolling of transformable grades of stainless steels and persist in the next processing steps. In the second theory, ridges are attributed to the non-homogeneous flow of the steel during cold rolling and subsequent forming operations such as deep drawing [6-10]. The former theory does not account for the fact that ridging is less pronounced in the transformable ferritic stainless steels in which the formation of compositional bands is more likely [6, 9].

In the latter theory, the non-homogeneous flow is attributed to the presence of texture bands of  $\alpha$ -fiber orientations, i.e.  $\langle 110 \rangle // \text{RD}$ , in a matrix oriented close to the  $\gamma$ -fiber, i.e.  $\langle 111 \rangle // \text{normal direction (ND)}$ . The  $\alpha$ -fiber texture components are believed to originate from as-cast columnar grains with  $\{001\} \langle uv0 \rangle$  orientations, which survive even after numerous processing steps [6, 8-9].

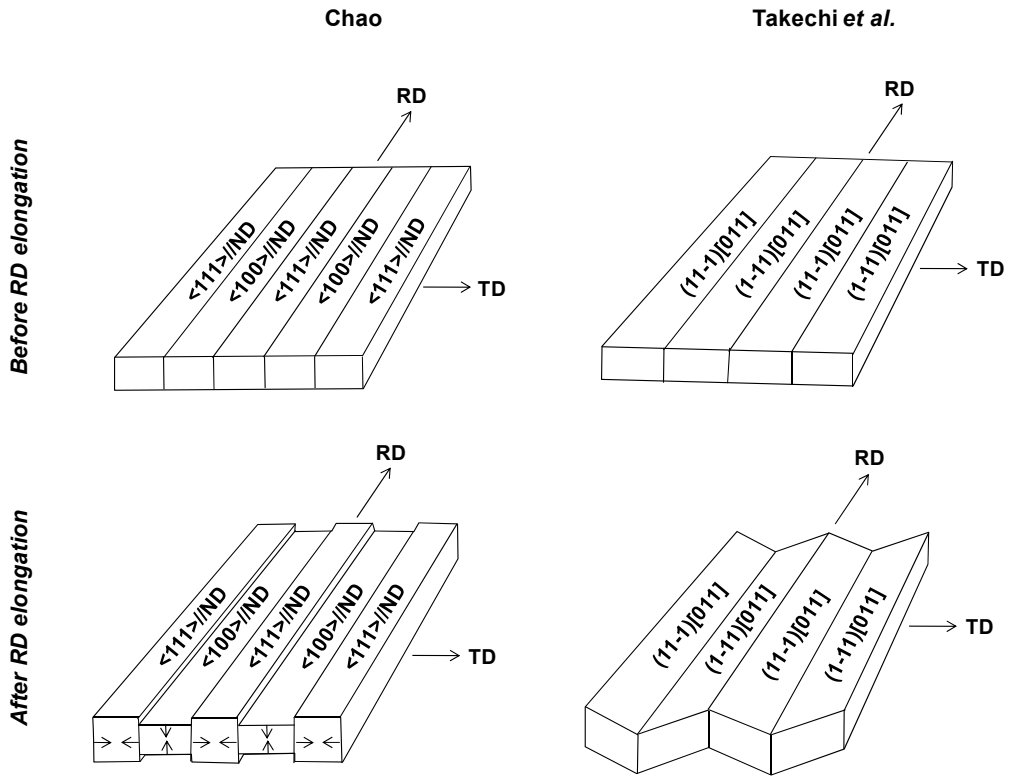


**Fig. 1.2.** Schematic representation of the ridging mechanisms proposed by Chao [11] and Takechi et al [12].

Several models have been proposed to explain the ridging mechanism. The original model of Chao [11] suggested that alternate arrangement of clusters of cube-on-face ( $\langle 100 \rangle // \text{ND}$ ) and  $\gamma$ -fiber oriented grains can lead to thickness variations after tensile straining in the RD (Fig. 1.2). This arises because upon tensile straining in the RD, the cube-on-face components show a larger strain in the thickness direction than in the transverse direction (TD). For the  $\gamma$ -fiber texture components, on the other hand, the

transverse strain would be larger than the thickness strain. Chao suggested that mixtures of  $\alpha$ -fiber and  $\gamma$ -fiber textures could behave analogously. As shown in Fig. 1.2, the Chao's model predicts a symmetric surface profile with respect to the mid-thickness plane, which is in contrast with the actual observation of an undulated surface (uniform thickness with maintained parallelism of opposite sides) after ridging. Takechi et al. [12] proposed a model which successfully reproduces the experimentally observed undulated surface profile in the sheets with severe ridging. As shown in Fig. 1.2, the alternate arrangement of bands of  $(11\bar{1})[011]$  and  $(1\bar{1}1)[011]$  symmetric variants will lead to opposite out-of-plane shear strains upon tensile straining in the RD. Similar results were obtained with the symmetric variants of the  $\{211\}\langle 011\rangle$  orientations. The Takechi's approach sounds plausible when considering cold rolled sheets in which  $\alpha$ -fiber orientations dominate the texture. This type of texture is, however, less common in annealed cold rolled sheet which questions the generality of the ridging mechanism of Takechi et al.

Wright [13] proposed a ridging mechanism based on the actual texture components commonly observed in the annealed ferritic sheets. In his model, the difference in the transverse strains of low r-value texture bands such as  $\{001\}\langle 110\rangle$  surrounded by a high r-value matrix oriented close to the  $\gamma$ -fiber results in the buckling of the low r-value bands as they show a smaller transverse contraction compared to the high r-value matrix. The more recent calculations based on the Crystal Plasticity Finite Element Method (CPFEM) of Shin et al. [6], however, have challenged the Wright's mechanism. They found that instead of buckling, the  $\{001\}\langle 110\rangle$  bands shrink in the thickness direction on both sides, i.e. a symmetric surface profile similar to that in the Chao's model (Fig. 1.2). The discrepancy arises from the strict assumption of Wright which implies that the distortion is limited to the band while according to the CPFEM calculations, the compatibility between the matrix and the band is compensated by straining of the matrix in the vicinity of the matrix/band interface without need for buckling in the band.

In their CPFEM calculations, Shin et al. [6] calculated surface profiles after a tensile strain, along the RD, of 20% for different texture colonies located in the central zone

of sheets. The matrix texture used in the calculations was the CPFEM calculated texture of an initially random aggregate of grains plane-strain compressed by 50%. Whereas the  $\{001\}\langle 110\rangle$  type colonies were associated with a symmetric surface profile with respect to the mid-thickness, i.e. no undulations, the  $\{111\}\langle 110\rangle$  and  $\{112\}\langle 110\rangle$  colonies were associated with an undulated surface profile.

Although the modeling attempts to correlate the texture and the ridging severity of ferritic stainless steel sheet have contributed to a better understanding of the ridging mechanism [6, 10-14], they remain qualitative and do not provide practical guidelines to alleviate ridging. The experimental assessment of the effect of composition on the microstructural evolution, and eventually the ridging height, needs to be further explored.

Countermeasures against ridging in ferritic stainless steels attempt to eliminate or reduce the volume fraction of the undesirable grain colonies. Hitherto proposed methods are the refinement of the solidification microstructure via electromagnetic stirring [15], the rolling of merely equiaxed grains by trimming out the columnar zone of the as-cast structure [6, 8], the cold rolling of  $\alpha'$  martensite [16], the double step cold rolling with an intermediate anneal [17-18], cross rolling [19], and un-lubricated hot rolling [20].

The elimination of annealing after hot rolling of ferritic stainless steels has been found to deteriorate the ridging resistance in the case of non-transformable ferritic stainless steels [18]. In the case of transformable grades, however, this procedure has been shown to result in weakly textured sheets having an improved ridging resistance [8].

#### 1.4. References

- [1] D. Peckner and I. M. Bernstein, *Handbook of stainless steels*. New York: McGraw-Hill, 1977.
- [2] *The Ferritic Solution Properties, Advantages, Applications*. Available: [http://www.cedinnox.es/PDF/Ferritic\\_Solution.pdf](http://www.cedinnox.es/PDF/Ferritic_Solution.pdf)

- [3] *Stainless Steel - Ferritic*. Available:  
<http://www.atimetals.com/ludlum/pages/products/xq/asp/G.3/qx/ProductLine.html>
- [4] K. Suzuki and S. Asami, "Ridging phenomenon related to the undulated segregation-pattern on transverse section in ferritic stainless steel," *Transactions of the Iron and Steel Institute of Japan*, vol. 24, pp. 359-364, 1984.
- [5] K. Suzuki, *et al.*, "Formation of ridging related to the banded segregation pattern of Cr and C on ferritic stainless steel sheet," *Transactions of the Iron and Steel Institute of Japan*, vol. 23, pp. 731-737, 1983.
- [6] H. J. Shin, *et al.*, "The effect of texture on ridging of ferritic stainless steel," *Acta Materialia*, vol. 51, pp. 4693-4706, 2003.
- [7] M. Brochu, *et al.*, "Analysis of grain colonies in type 430 ferritic stainless steels by Electron Back Scattering Diffraction (EBSD)," *ISIJ International*, vol. 37, pp. 872-877, 1997.
- [8] J. I. Hamada, *et al.*, "Effect of Initial Solidified Structure on Ridging Phenomenon and Texture in Type 430 Ferritic Stainless Steel Sheets," *ISIJ International*, vol. 43, pp. 1989-1998, 2003.
- [9] S. H. Park, *et al.*, "Evolution of microstructure and texture associated with ridging in ferritic stainless steels," *ISIJ International*, vol. 42, pp. 100-105, 2002.
- [10] P. D. Wu, *et al.*, "Analysis of ridging in ferritic stainless steel sheet," *Materials Science and Engineering A*, vol. 423, pp. 300-305, 2006.
- [11] H. C. Chao, "The mechanism of ridging in ferritic stainless steels," *Transactions of the American Society for Metals*, vol. 60, pp. 37-50, 1967.
- [12] H. Takechi, *et al.*, "The mechanism of ridging phenomenon in 17% chromium stainless steel sheets," *J. Jpn. Inst. Met.*, vol. 31, pp. 717-723, 1967.
- [13] R. N. Wright, "Anisotropic plastic flow in ferritic stainless steels and the "roping" phenomenon," *Metallurgical Transactions*, vol. 3, pp. 83-91, 1972.

- [14] O. Engler, *et al.*, "Crystal-plasticity analysis of ridging in ferritic stainless steel sheets," *Metallurgical and Materials Transactions A: Physical Metallurgy and Materials Science*, vol. 36, pp. 3127-3139, 2005.
- [15] Y. Itoh, *et al.*, "Refining of solidification structures of continuously cast type 430 stainless steel slabs by electromagnetic stirring," *Transactions of the Iron and Steel Institute of Japan*, vol. 22, pp. 223-229, 1982.
- [16] T. Tsuchiyama, *et al.*, "Ridging-free ferritic stainless steel produced through recrystallization of lath martensite," *ISIJ International*, vol. 45, pp. 923-929, 2005.
- [17] M. Y. Huh and O. Engler, "Effect of intermediate annealing on texture, formability and ridging of 17%Cr ferritic stainless steel sheet," *Materials Science and Engineering A*, vol. 308, pp. 74-87, 2001.
- [18] I. Jung, "Influence of the Cold Rolling Conditions on the Texture Development and Formability of Ti stabilized 18% Cr Ferritic Stainless Steel," MS, Graduate Institute of Ferrous Technology, POSTECH, Pohang, 2009.
- [19] M. Y. Huh, *et al.*, "Effect of through-thickness macro and micro-texture gradients on ridging of 17%Cr ferritic stainless steel sheet," *Steel Research International*, vol. 76, pp. 797-806, 2005.
- [20] H. G. Kang, *et al.*, "Effect of lubrication during hot rolling on the evolution of through-thickness textures in 18%Cr ferritic stainless steel sheet," *Steel Research International*, vol. 79, pp. 489-496, 2008.





# Chapter II

## Experimental Procedure

### **2.1. Dilatometry**

Dilatometry experiments were performed using 10 mm-long specimens with various cross sections in a precision Bahr 805A/D pushrod dilatometer (Bähr-Thermoanalyse GmbH, Hüllhorst, Germany). Prior to each experiment, the chamber was evacuated to a vacuum of better than  $6 \times 10^{-3}$  mbar. For quenching, high purity He or Ar was blown into the chamber.

### **2.2. Scanning Electron Microscopy (SEM)**

A Zeiss Ultra 55 Field Emission type SEM (Carl Zeiss NTS GmbH, Oberkochen, Germany) equipped with an Electron Backscattering Diffraction (EBSD) detector was used to examine the microstructure of etched specimens. Specimens for SEM observations were etched either chemically or electro-chemically. Chemical etching was performed at room temperature in a modified Vilella's reagent with an increased concentration of HCl, and H<sub>2</sub>O<sub>2</sub> added as a catalyst (1 gr picric acid, 20 mL HCl, 100 mL ethanol, and 0.1 mL of H<sub>2</sub>O<sub>2</sub>). Chemical etching time was less than 10 sec. Electro-etching was carried out in a solution of 60% HNO<sub>3</sub> and 40% H<sub>2</sub>O. The voltage was increased stepwise in the range of 3-5 V so as to obtain a current density of about 0.1 A/cm<sup>2</sup>. Electro-etching time was typically 30 sec.

EBSD measurements were performed using unetched specimens at an increased voltage of 20 kV. Sample preparation for EBSD consisted of SiC paper grinding, polishing using diamond paste down in size to 0.25  $\mu\text{m}$  and 40 min of colloidal silica polishing followed by a final ultrasonic cleaning stage.

### **2.3. Transmission Electron Microscopy (TEM)**

Transmission Electron Microscopy (TEM) observations were performed either in a JEOL JEM-2100 TEM with a LaB<sub>6</sub> type gun or in a field emission type Scanning TEM (JEOL, Tokyo, Japan) both operated at 200 kV. TEM foils were prepared by mechanical polishing to a thickness range of 50-100  $\mu\text{m}$ , followed by twin-jet polishing at a temperature of -10 °C, using a typical jet polishing voltage of 30 V and a typical current of 70 mA. A solution of 10% perchloric acid in 90% ethanol was used as the electrolyte. It was later confirmed that even room temperature jet polishing using a solution of 5% perchloric acid in 95% acetic acid resulted in equally good TEM specimens.

### **2.4. Electron Probe Micro-Analysis (EPMA)**

A JEOL JXA-8100 type EPMA was used to determine the elemental distribution in unetched specimens.

### **2.5. Tensile Test**

Tensile experiments were performed using a Zwick/Roell universal tensile testing machine in order to determine the general mechanical properties, r-value, and to prepare specimens for ridging resistance assessment by profilometry. Table 2.1 summarizes the sizing of tensile specimens used for different purposes.

Tensile tests for the determination of tensile strength and elongation of specimens making 0 °, 45 °, and 90 ° to rolling direction were carried out at a strain rate of 0.005 s<sup>-1</sup> until rupture. These experiments were performed using standard ASTM E8 tensile specimens.

**Table 2.1.** Type and dimension of tensile specimens used in this study.

<b>Tensile Specimen Standard</b>	<b>Measurement Type</b>	<b>Gauge Length (mm)</b>	<b>Length of Reduced Section (mm)</b>	<b>Gauge Width (mm)</b>
ASTM E8 (Standard Size)	Mechanical properties, r- value, ridging	50	60	12.5
ASTM E8 (Subsize)	Mechanical properties	25	32	6
Japanese JIS Z 2201/5	Ridging	50	60	25

The normal anisotropy, r-value, which is a commonly used measure of sheet formability, can be calculated using the following formula:

$$r = \frac{\varepsilon_w}{\varepsilon_t} = \frac{\varepsilon_w}{\varepsilon_w + \varepsilon_l} \quad (\text{Equation 2.1})$$

where  $\varepsilon_t$ ,  $\varepsilon_w$ , and  $\varepsilon_l$  are the true strains along the thickness, width, and length directions of the tensile specimens, respectively. The r-value can be calculated either automatically using an in-situ width monitor or by manual measurement of the width change after a certain tensile strain. In the automatic method, the instantaneous width change of standard ASTM E8 tensile specimens was monitored in the engineering strain range of 10-15% and the average value was reported. The strain rate for these tests was  $0.005 \text{ s}^{-1}$ .

In the manual r-value measurement method, three lines were drawn parallel to the width direction of standard ASTM E8 tensile specimens. One of the lines was drawn in the middle of the gauge and two others were drawn on its either side at a distance of 15 mm. After precise measurement of the specimen width in the marked sections, tensile tests were performed up to a strain of 15% and the average width change in the marked sections was measured. After conversion of the engineering strains to true strains, the r-values were calculated using Equation 2.1. Tensile tests for r-value

measurement were performed at a strain rate of 10 mm/min before yielding and 20 mm/min after yielding.

The r-value of the industrially processed sheet steels is usually anisotropic and varies with the sampling direction. Therefore, it is usually measured at different angles to rolling direction and the mean value is calculated. In the current project, r-value was invariably measured at 0 °, 45 °, and 90 ° to the rolling direction and the mean r-value,  $r_m$ , was calculated using the following equation:

$$r_m = \frac{r_0 + 2r_{45} + r_{90}}{4} \quad (\text{Equation 2.2})$$

$\Delta r$ , the planar anisotropy, was calculated on the basis of the following equation:

$$\Delta r = \frac{r_0 - 2r_{45} + r_{90}}{2} \quad (\text{Equation 2.3})$$

High mean r-values and  $\Delta r$  values close to zero are desirable in view of the formability. A high normal anisotropy allows high deep drawing ratios to be applied and a low  $\Delta r$  ensures that the earing will be minimized during deep drawing.

For ridging assessment, either standard ASTM E8 tensile specimens or 25 mm-wide tensile specimens prepared according to the Japanese JIS Z 2201/5 standard were taken parallel to the RD. Tensile specimens were strained 15% at a strain rate of 0.005 s<sup>-1</sup> and roughness measurements followed.

## 2.6. Ridging Resistance by Profilometry

Roughness measurements were made in the Transverse Direction (TD) of the tensile specimens strained 15% in the RD. A cutoff length ( $\lambda c$ ) of 2.5 mm was used for the roughness measurements. The roughness parameters  $R_a$  and  $R_t$  were calculated from the following equations:

$$R_a = \frac{1}{L} \int_0^L |y| dx \quad (\text{Equation 2.4})$$

$$R_t = y_{\max} - y_{\min} \quad (\text{Equation 2.5})$$

where  $y$  denotes the vertical distance from the center line and  $L$  indicates the measurement length along the measurement direction  $x$ . The ridging resistance is inversely proportional to the roughness parameters  $R_a$  and  $R_t$  which are shown schematically in Fig. 2.1.

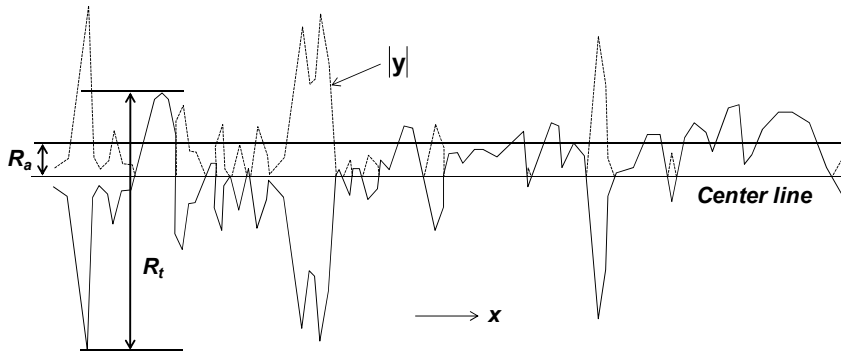


**Fig. 2.1.** Schematic representation of the roughness parameters  $R_a$  and  $R_t$ .



# Chapter III

## Alloy System and Processing Technology

### 3.1. Material

Chemical composition of the three variants of the AISI type 430 ferritic stainless steel provided in different conditions by Pohang Steel Company (POSCO, Pohang, South Korea) is given in Table 3.1. They will be referred to as “low C”, “standard”, and “Al-added” or alternatively “steel A”, “steel B”, and “steel C”, respectively. The composition of these grades is so that they partially transform to austenite in the hot rolling temperatures. The equilibrium pseudo-binary phase diagram and the austenite fraction evolution in the three steels according to the Thermo-Calc with a TCFE6 database is shown in Fig. 3.1 and Fig. 3.2. According to the phase diagrams, steels A and B are predicted to have a fully ferritic matrix with embedded  $M_{23}C_6$  and  $M_2N$  precipitates ( $M=Cr,Fe$ ) at room temperature. For steel C, however, the  $M_2N$  will be replaced by  $AlN$  because of the higher affinity of Al for N. The tensile graphs of industrial sheets of these steels before the skin pass processing indicated a much larger strain aging for steels A and B compared to the steel C (Fig. 3.3). This suggests that the solute N is responsible for the strain aging in steels A and B because the addition of the strong nitride former Al reduces the strain aging significantly. It must be noted that the Al content of steel C is more than the stoichiometric Al content required for the full stabilization of N in the form of  $AlN$ . It can therefore be implied that the

formation of  $M_2N$  in the AISI 430 is limited so that N remains in solution and leads to strain aging.

**Table 3.1.** Chemical composition of AISI 430 stainless steels used in this project.

	C	N	Cr	Mn	Ni	Si	Al	Ti	Fe
<b>Steel A (low C)</b>	0.023	0.040	16.19	0.524	0.15	0.226	0.003	-	Bal.
<b>Steel B (standard)</b>	0.040	0.036	16.13	0.388	0.13	0.294	0.003	0.008	Bal.
<b>Steel C (Al-added)</b>	0.075	0.028	16.15	0.502	0.13	0.258	0.106	-	Bal.

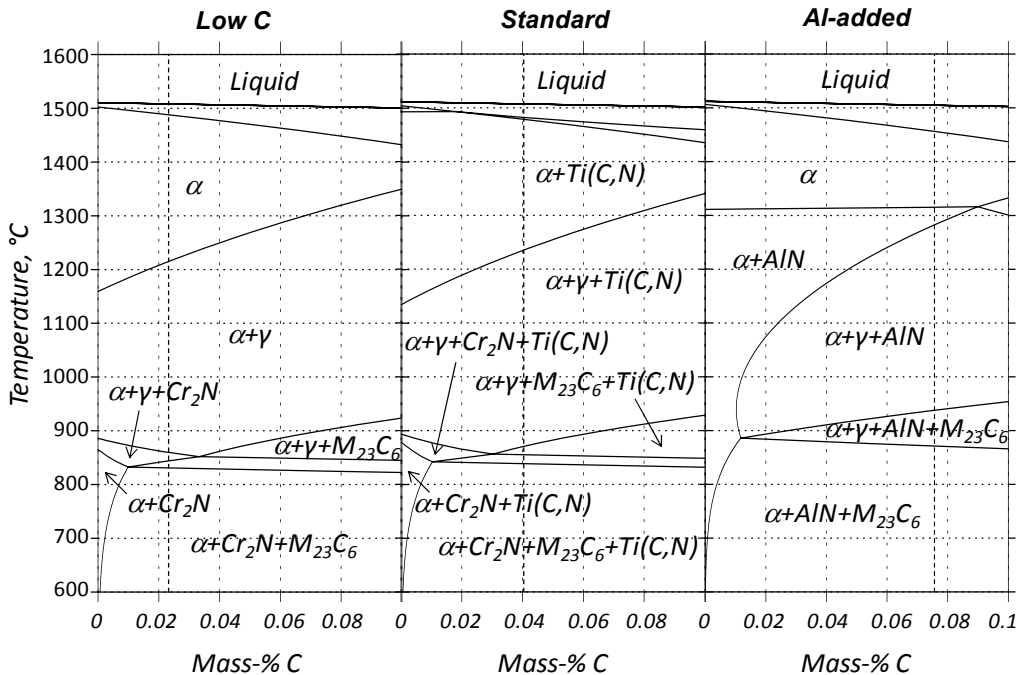


**Fig. 3.1.** Pseudo-binary equilibrium phase diagrams according to the Thermo-Calc.

The carbon content of each steel is indicated by a dashed line. For the low C and standard compositions, the AlN formation was excluded.

Steel B represents the composition of a standard AISI 430 grade. In addition to the standard composition listed in Table 3.1, other variants of standard AISI 430 with compositions very similar to steel B in Table 3.1 were used in the processing routes



discussed in chapters 6-9. Nevertheless, due to the close compositional proximity of all standard compositions used in this work, no distinction will be made among them and they will all be treated the same. It must be noted that the Ti content of the standard composition is so low that, even when fully stabilized with interstitials C and N, it does not cause a significant change in the solute interstitials content. For instance, assuming that Ti is fully stabilized in the form of TiN, the amount of stabilized N will be limited to 25 ppm.

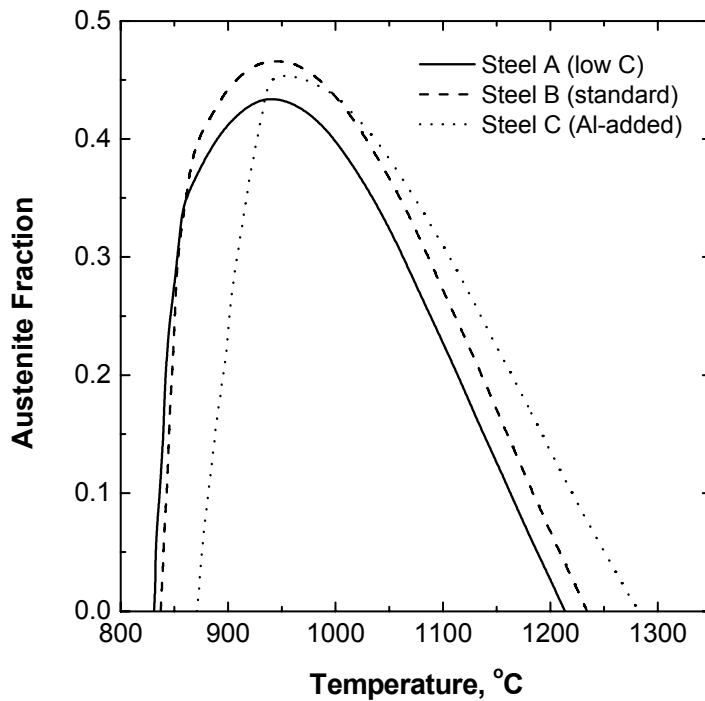


**Fig. 3.2.** Equilibrium austenite phase fractions according to the Thermo-Calc.

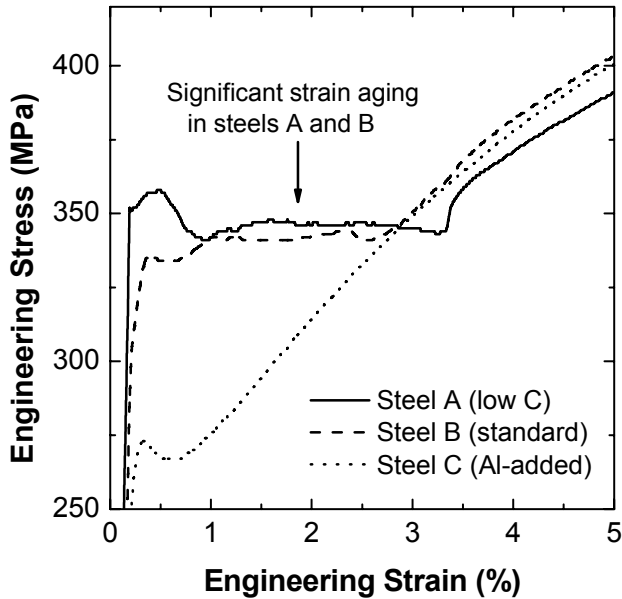


**Fig. 3.3.** Engineering stress-strain curves for the cold rolled and annealed AISI 430 sheets of different compositions.

### 3.2. Conventional Production Technology of AISI 430

The sheet production technology of the AISI 430 is schematically shown in Fig. 3.4. Continuously cast slabs with typical thicknesses in the range of 200-250 mm (Fig. 3.5) are reheated to temperatures of the order of 1200 °C at which a dual phase  $\alpha+\gamma$  microstructure is stable. The austenite fraction at this temperature is largely controlled by the content of solute interstitials. Presence of carbide and nitride forming elements at the slab reheating temperature can therefore affect the austenite fraction. The reheated slab is then rough rolled in the reversing mills to a typical thickness 30 mm. The temperature of the end of the rough rolling step is approximately 1050 °C. Finish rolling is typically performed in the temperature range of 890-950 °C during which the thickness of the rough rolled bar is reduced to about 3 mm. The fraction of austenite changes as the hot rolling proceeds. The hot rolled strip is then cooled on the run-out table to temperatures of the order of the 700 °C at which the coiling is carried out. Due to the low cooling rates involved in the coil, the coiling temperature is of importance to the microstructure of the hot strips. A prolonged exposure in the temperature range of 600-800 °C can lead to the decomposition of austenite to ferrite and precipitates

notably  $M_{23}C_6$ . Too high a coiling temperature can therefore lead to the total decomposition of austenite to ferrite and precipitates. Coiling at lower temperatures, on the other hand, ensures that the high temperature austenite decomposition will not occur. In this case, austenite will transform to martensite as the  $M_s$  temperature is reached.

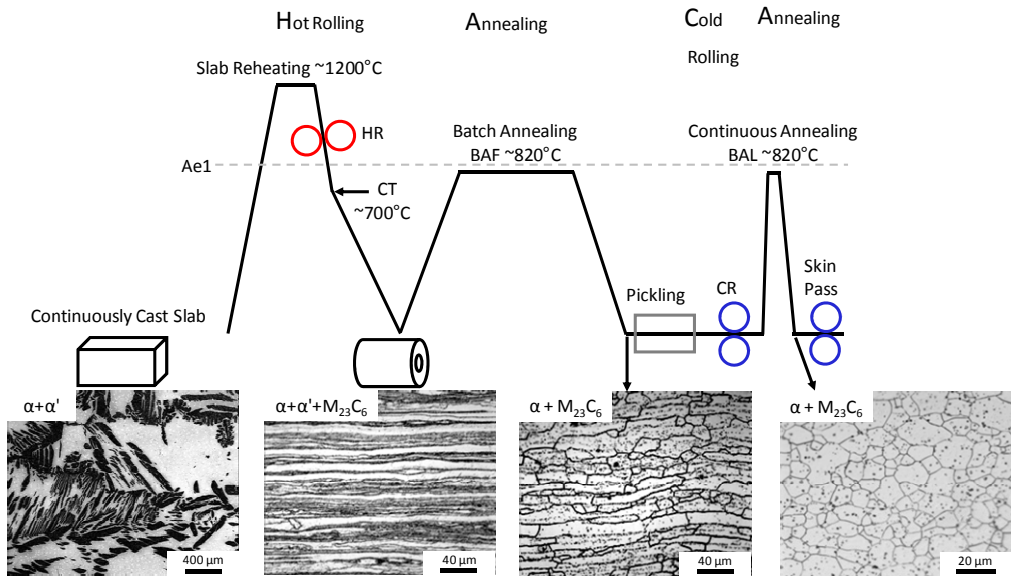


**Fig. 3.4.** Schematic of the conventional thermo-mechanical processing of the AISI 430 stainless steel and associated microstructural changes.

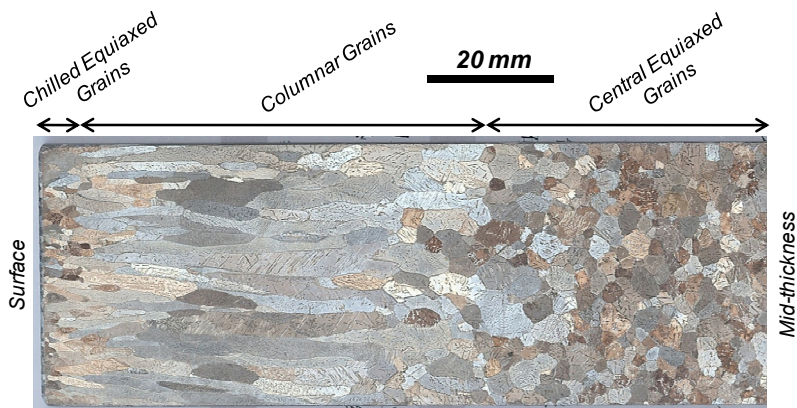


**Fig. 3.5.** Photomicrograph showing the macrostructure of a continuously cast slab of the AISI 430 stainless steel.

In addition to the coiling temperature, the alloying elements can also influence the stability of austenite and thereby control the microstructure of the hot strip. A low C/N ratio in the austenite increases the stability of austenite. This is because the N is known to retard the  $M_{23}C_6$  formation [1-2] which takes place concurrently with the austenite decomposition.

Fig. 3.6 compares the microstructure of two differently processed hot strips of standard composition with different hardness levels. The microstructure in the transformed regions of the harder hot strip was dominated by a large martensite fraction and a small fraction of fine precipitates at or very close to the  $\alpha$ - $\alpha'$  phase boundaries. In the softer hot strip, on the other hand, it was hard to find martensitic regions due to the high temperature decomposition of austenite to ferrite and precipitates. As a result, the precipitate fraction was larger and they were commonly observed in the boundaries. The difference in the microstructure and the hardness of AISI 430 hot strips of standard composition indicates a difference in their exposure time to temperatures in excess of about 600 °C where Cr diffusivity is high enough to allow for the formation of  $M_{23}C_6$  precipitates. The microstructure of the hot rolled strip is therefore closely controlled by the coiling temperature and the position in the coil which determines the cooling rate.

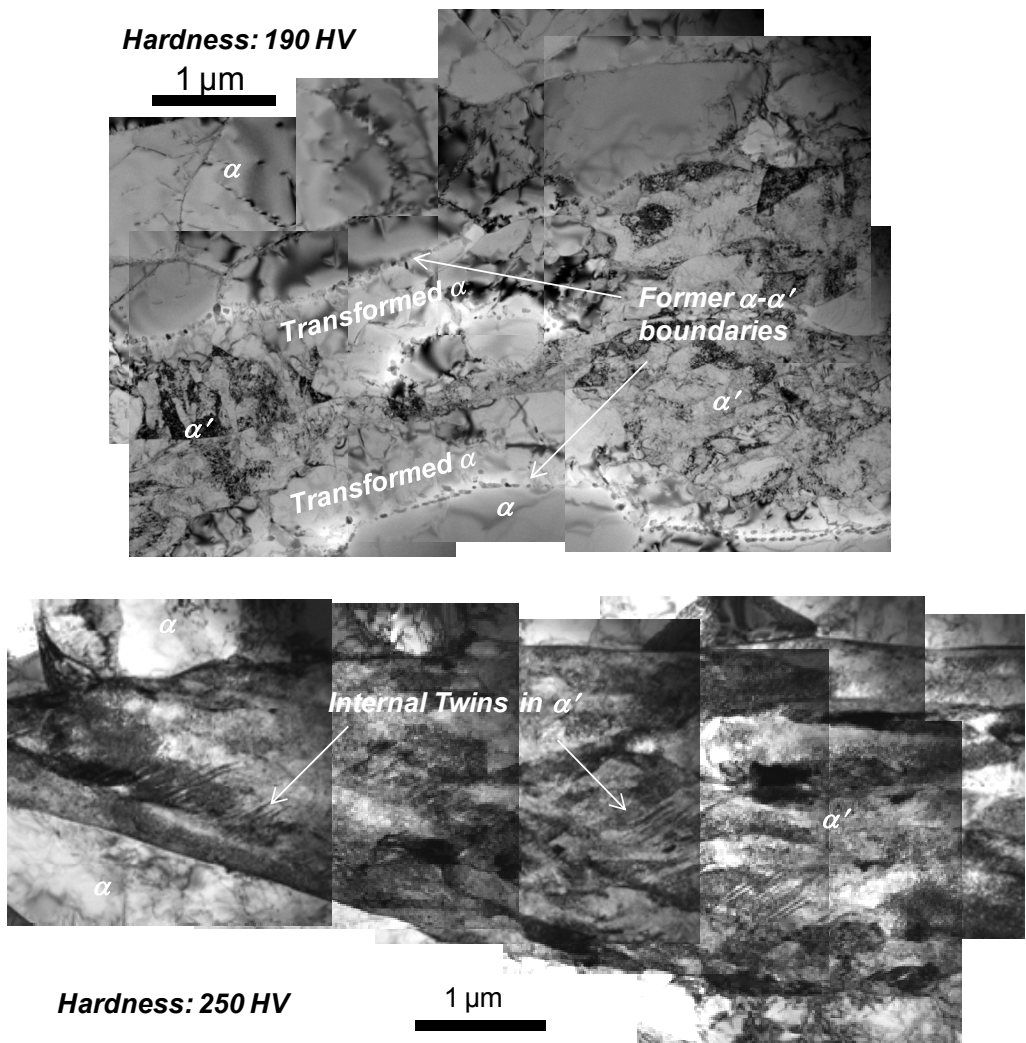


**Fig. 3.6.** TEM micrographs of two differently processed hot strips of standard AISI 430 stainless steel. In the softer hot strip (top), high temperature decomposition of austenite leads to a small martensite fraction. In contrast, the microstructure of transformed regions of the harder hot strip (bottom) is dominated by martensite.

The thermal restoration mechanisms during hot rolling of metals are governed by the stacking fault energy (SFE) where a high SFE promotes the recovery and a low SFE favors the recrystallization. It is well-known that the ferrite has a high SFE and is reluctant to recrystallize during hot rolling [3]. The ferrite at the end of the hot rolling is therefore expected to show a recovered microstructure characterized by a high

density of low angle grain boundaries. The EBSD map in Fig. 3.7 highlights the high angle and low angle boundaries in the microstructure of a hot rolled strip of standard composition. The low angle grain boundaries are observed not only in the untransformed ferrite but also in the transformed ferrite grains. This suggests that even austenite does not fully recrystallize under the hot rolling conditions so that the dislocations in the austenite are later inherited by the ferrite.

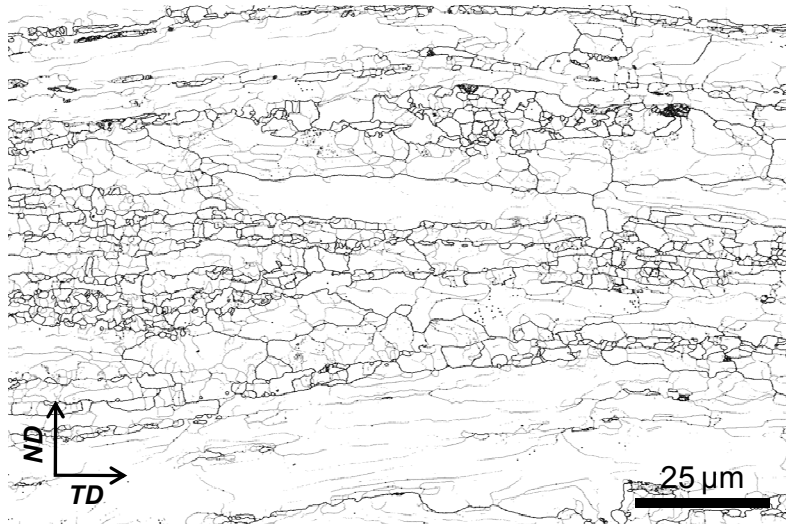


**Fig. 3.7.** EBSD map of a hot rolled strip of standard AISI 430 composition highlighting boundaries with misorientations larger than  $15^\circ$  (black) and misorientations in the range of  $2-15^\circ$  (gray).

The non-homogenous nature of the microstructure in the hot rolled strips calls for a homogenization anneal in order to obtain a homogenous microstructure composed of a dislocation free ferritic matrix and embedded  $M_{23}C_6$  carbides. This treatment is done in batch annealing furnaces where coils are held for a long time at temperatures just below the  $A_{e1}$  temperature. Fig. 3.8 shows the EBSD grain boundary maps of batch annealed hot strips of low C, standard, and Al-added compositions. The difference in the grain size is thought to be related to the fraction and the distribution of martensite in the hot strip. The finer grain size of the low C composition likely arises from its

higher N/C ratio which increases the martensite fraction of the hot strip by increasing the stability of austenite at the end of the hot rolling operations.

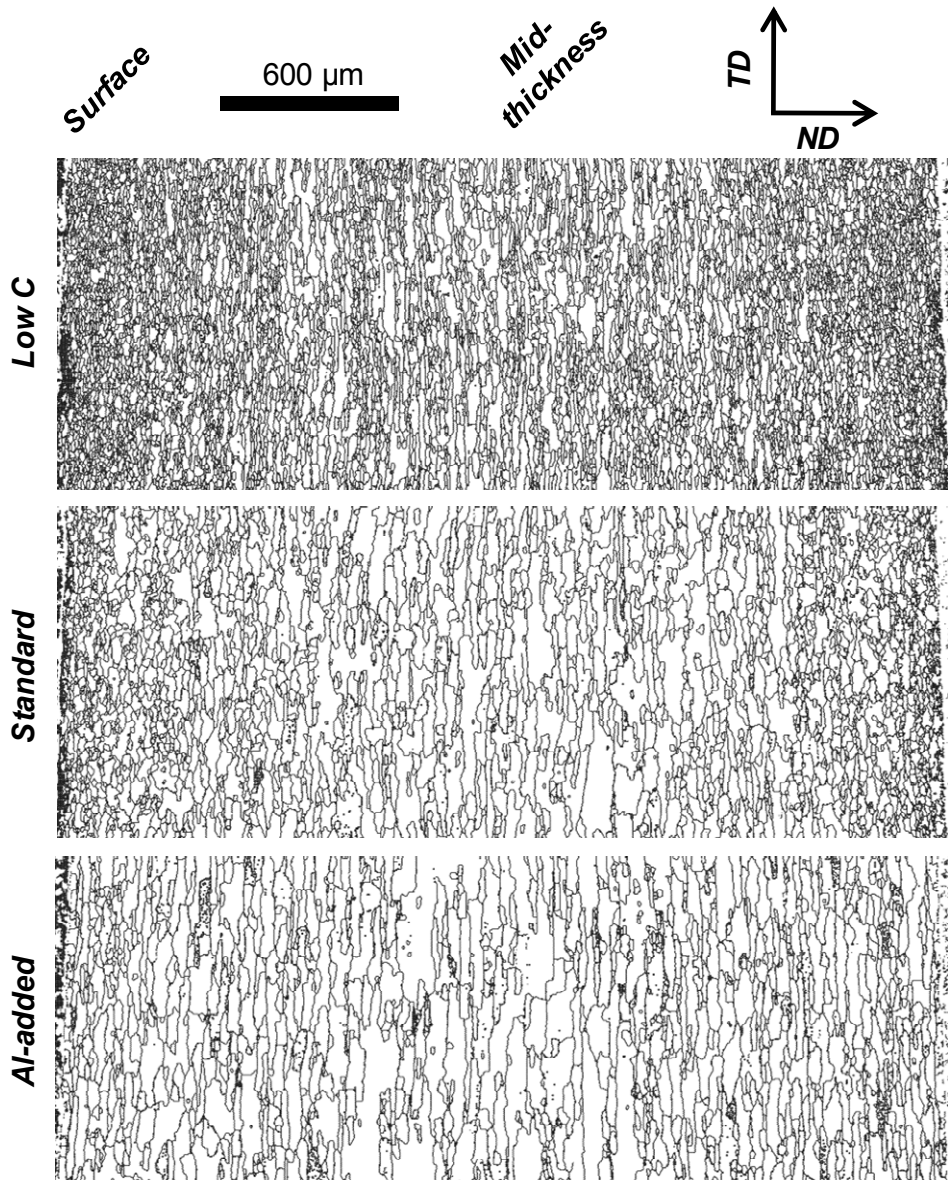


**Fig. 3.8.** EBSD maps of batch annealed hot strips of different compositions highlighting boundaries with misorientations larger than  $15^\circ$ .

After the batch annealing treatment, the hot strips are pickled to remove the surface oxide layer prior to cold rolling. After cold rolling to typical thicknesses of the order of 0.5-1 mm, a continuous annealing step follows which softens the sheets through the recrystallization of the deformed microstructure. In the continuous annealing step, it is desirable to achieve a strong  $\gamma$ -fiber texture, i.e. obtain a high density of grains with their  $\langle 111 \rangle$  type crystal axis parallel to the ND. This type of texture is known to be associated with a proper deep drawability and a high resistance to earing due to a high normal and a low planar anisotropy [4-5].

Due to the presence of solute interstitials particularly N, the recrystallization annealed sheets display strain aging which makes them susceptible to the appearance of stretcher strains during sheet forming operations. The skin pass step after the recrystallization anneal is intended to generate unlocked dislocations and ensure the absence of stretcher strains.

### 3.3. References

- [1] T. Sourmail, "Precipitation in creep resistant austenitic stainless steels," *Materials Science and Technology*, vol. 17, pp. 1-14, 2001.
- [2] F. B. Pickering, "Some beneficial effects of nitrogen in steels," in *High Nitrogen Steels*, Lille, France, 1988, pp. 10-31.
- [3] J. S. Hinton and J. H. Beynon, "Restoration processes during hot deformation in the  $\delta$ -ferrite and austenite dual phase region of AISI430 ferritic stainless steel," *ISIJ International*, vol. 47, pp. 1465-1474, 2007.
- [4] R. K. Ray, *et al.*, "Transformation textures in steels," *ISIJ International*, vol. 34, pp. 927-942, 1994.
- [5] B. C. De Cooman and J. G. Speer, *Fundamentals of Steel Product Physical Metallurgy*. Warrendale: Association for Iron and Steel Technology, 2011.





## Chapter IV

# Anisotropic Dimensional Change in Rough Rolled Bars

Anisotropic dimensional changes in a 16%Cr ferritic stainless steel possessing a banded structure of  $\alpha+\alpha'$  obtained by hot rolling were studied. Considerable anisotropic transformation plasticity was observed during both the austenitization and the martensite formation reactions. Anisotropy was also observed in case of the Coefficient of Thermal Expansion (CTE), over a wide annealing temperature range. The observations are shown to be due to the geometrical arrangement of the phases, with ferrite acting as a constraint against the in-rolling-plane straining of the pancaked  $\gamma$  thus encouraging exaggerated dimensional changes along the normal direction. Assuming isotropic dimensional change within the rolling plane and combining the dilatometric results in the rolling and normal directions, the measured dilatation and CTE can be used to determine the volume fraction of  $\alpha'$ . This alternative phase analysis method is shown to have advantages compared to a conventional image analysis method especially at low annealing temperatures where there are still residues of the tempered martensite.

#### 4.1. Introduction

Dilatometry is a powerful tool for the analysis of phase transformations in steels. Phase fraction analysis in the intercritical range of carbon steels using the lever rule and kinetics study of the formation and decomposition of austenite are common dilatometric investigations [1-3]. De Andrés *et al.* [4] have reviewed applications of dilatometry to the analysis of solid state phase transformations in steels with an emphasis on the construction of continuous heating and cooling diagrams. In contrast to carbon steels, dilatometry is rarely used to study transformations in stainless steels since austenitic grades do not transform and ferritic grades only partially transform or do not transform at all. The method is therefore not well known when it comes to using it for detailed transformation studies in stainless steels.

During austenite decomposition in carbon steels with homogeneous microstructures, the dilatometric cooling curve has often been found not to follow the heating curve after the complete decomposition of the austenite into the ferrite and pearlite. In other words, at the end of each cycle with, in principle, similar initial and final microstructures, a permanent contraction along the axis of cylindrical specimens is recorded. In the case of homogenous microstructures, development of a radial thermal gradient is usually identified as the cause of the non-isotropic length change since the expansion, due to the decomposition of the hard austenite, is easier to accommodate along the radius of the specimens. Expressed differently, the non-transformed  $\gamma$  is believed to act as a constraint against the axial stretching of the phase boundary [5].

Suh *et al.* [6] have shown that carbon steel specimens with a non-homogenous structure consisting of the compositional bands created by hot rolling can display different dilatational characteristics along the rolling (RD) and the normal (ND) directions. This difference decreases by increasing the cooling rate from the austenitization temperature. Microstructural examination of the dilatometric specimens after cooling at different rates indicated that the initial banded structure is retained at low cooling rates whereas cooling rates above a certain level induce random nucleation of ferrite and a considerably reduced anisotropy.

In another study of the anisotropic dilatation [7], artificially made roll bonded steel composites consisting of alternating layers of low- and high-Mn low alloy steels with known bandwidths, were tested by dilatometry along the RD and ND directions. Cycling of the ND-oriented specimens from room temperature to above the  $A_{c3}$  and down to below the  $M_s$  temperatures of both constituents brought about a permanent expansion whereas the RD-oriented specimens cycled similarly experienced a permanent contraction. This behavior was rationalized by the coupling between plastic deformation and phase transformations [8].

Farooque *et al.* [9] have evaluated the dimensional anisotropy of a commercial hot extruded 18 mass-%Ni maraging steel cycled through the martensitic transformation and austenite reversion reactions. While the specimen oriented along the transverse direction of the rod experienced a permanent expansion, the longitudinal specimen contracted after each cycle. These observations were attributed to the interdendritic segregation of alloying elements during solidification which leads to the formation of bands with different martensite start and austenite reversion temperatures. While the longitudinal specimen retained its circular cross section after numerous cycles, cross section of the transverse specimen eventually became elliptical. This was ascribed to the positioning of the fibroid bands parallel to the extrusion direction with the consequence of radial contraction of the transverse specimen in the direction parallel to the extrusion direction and radial expansion normal to it. Interestingly, the initial expansion due to cycling of the transverse specimen changed to a contraction by introducing a cold rolling step prior to the cycle, which caused the bands to stretch along the axis of the specimen. It was only after an extensive homogenization treatment that the anisotropic behavior vanished and instead comparable contractions were measured along both the longitudinal and the transverse directions, presumably due to the radial thermal gradient.

In another study of the anisotropic dimensional change performed on a non-transforming duplex stainless steel with a nearly constant phase fraction from the room temperature up to the annealing temperature of 900 °C, Siegmund *et al.* [10] measured the permanent strain after annealing of the longitudinal and transverse

specimens taken from a forged rod with a uniaxially anisotropic microstructure. In the absence of any transformation plasticity, the longitudinal specimen expanded with each cycle whereas the transverse specimen shrank. The results were interpreted in view of the dissimilar Coefficients of Thermal Expansion (CTE) of  $\gamma$  and  $\alpha$ , coexisting in a banded structure, which upon heating, led to the development of compressive micro-stresses in  $\gamma$  and tensile micro-stresses in  $\alpha$  parallel to the bands, and those of opposite signs on cooling. When the micro-stresses exceeded the yield strength of the weaker phase, they could lead to the plastic strain. During heating,  $\alpha$ , the weaker phase at high temperatures elongated in tension whereas during cooling,  $\gamma$ , the weaker phase at low temperatures yielded in tension which added to the already existing positive strain. Similar observations were made by Fischer *et al.* [11] in the case of longitudinal and transverse duplex stainless steel specimens taken from a forged rod cycled in the range 17-925 °C. Whereas the longitudinal specimen monotonically increased in length with an elongation of 50% after 1000 cycles, the transverse specimen contracted by 8%.

Using X-ray diffraction, Mary *et al.* [12] quantified the residual stresses in the  $\alpha$  and  $\gamma$  phases present in the banded microstructure of a hot rolled duplex stainless steel. At surface, residual compressive stresses were measured in both phases along the rolling direction after mechanical polishing, but they were smaller in the case of  $\gamma$ . Compressive stresses were a result of thermal and mechanical effects of polishing on the surface and decreased by using a less vigorous surface preparation technique. After electropolishing, which led to the removal of the mechanically damaged surface and amplified the thermal effects, the compressive stresses in  $\gamma$  turned to tensile while  $\alpha$  still exhibited compressive stresses. The thermal stresses, also predicted by the finite element method, mainly arise from the CTE difference of  $\alpha$  and  $\gamma$ .

The previous reports on anisotropic dimensional change dealt with single phase steels [5-6], steels with two phases with similar CTEs [7-9], or non-transformable dual-phase steels [10-11]. In the present study, the dimensional change anisotropy in a standard AISI 430 grade with a banded structure of  $\alpha+\alpha'$  after hot rolling is reported. Since the fraction of  $\gamma$  is of relevance to the optimization of the processing conditions

of 16%Cr ferritic stainless steels to achieve a desirable combination of ridging resistance and formability [13], a method is presented here which combines the dilatometric results from differently oriented dilatometric specimens and lays a more meaningful base for the phase fraction analysis in the presence of planar anisotropy.

#### **4.2. Experimental procedure**

The chemical composition of the standard AISI 430 grade bars used in the dilatometric studies is given in Table 3.1. Thermo-Calc was used to calculate the equilibrium austenite fractions using the TCFE4 database.

Dilatometry experiments were performed in a precision Bahr 805 pushrod quench dilatometer under a vacuum of better than  $6 \times 10^{-3}$  mbar during the heating and soaking steps. For quenching, high purity He was blown into the chamber to achieve a cooling rate of 20 °C/s. The annealing schemes simulated with the dilatometer are summarized in Fig. 4.1. Annealing cycles in the temperature range of 850 °C to 1200 °C were evaluated. The holding time was 2 min. 10 mm-long cylindrical specimens with a diameter of 4 mm or flat specimens of the same length with a square cross section of 3.5 mm×3.5 mm, machined from the mid-thickness of the 30 mm-thick hot rolled bars, were utilized in the dilatometry tests after the section independence of the dilatometric results was confirmed with a few trial runs. Machining of specimens from the mid-thickness of bars prevented the through thickness non-homogeneities from affecting the results. Two series of differently oriented specimens with their axes parallel to the ND and RD, as schematically illustrated in Fig. 4.2, were studied. The average of three dilatometric measurements is reported.

Optical microscopy and image analysis of samples mechanically polished according to standard metallographic techniques were carried out after chemical etching with a modification of Vilella's reagent with an increased concentration of HCl and the addition of H<sub>2</sub>O<sub>2</sub> as a catalyst. This solution was found to produce an adequate contrast to differentiate between the martensite and the ferritic matrix during the analysis of the optical micrographs.

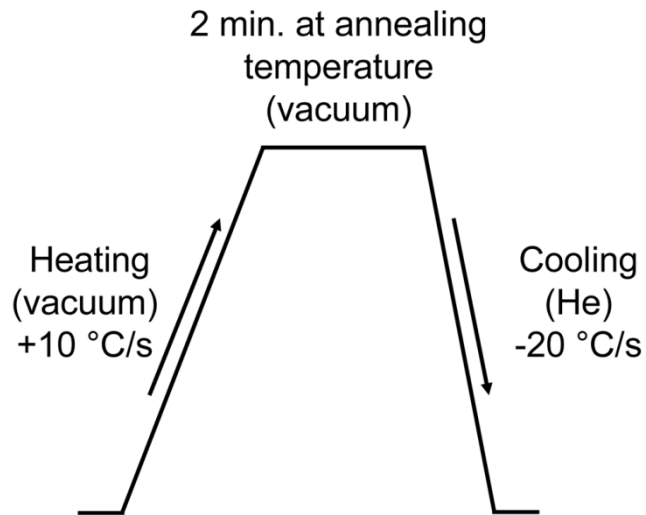


**Fig. 4.1.** Schematic showing the thermal cycle used for the dilatometry. Annealing temperatures from 850 °C to 1200 °C were used. Temperature increments were typically 50 °C.

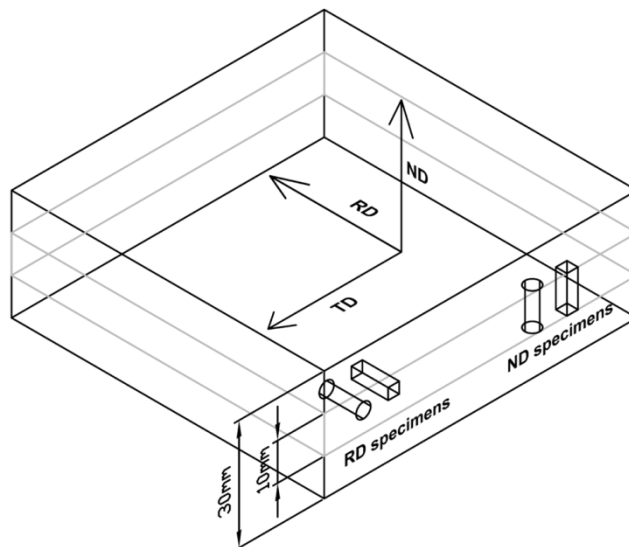


**Fig. 4.2.** Schematic representation of the dilatometry sampling from the hot rolled bar.

A Bruker D8 Advance X-ray diffractometer with a Cu tube was utilized to measure the lattice parameters of  $\alpha$  and  $\gamma$  at temperatures up to 1025 °C during heating and

cooling at an identical rate of 1 °C/s. To ensure temperature equalization, the sample temperature was stabilized for 1 min at each temperature, prior to the measurements. Measurements were performed using an evacuated heating stage equipped with a radiation heater. Using a step size of 0.02 ° and a dwell time per step of 0.1 sec, the lattice parameters were calculated on the basis of the (110)<sub>α</sub> and (111)<sub>γ</sub> peaks.

EBSD was used to compare the image quality maps of dilatometry specimens after annealing at two different temperatures of 850 °C and 1000 °C.

### 4.3. Results and Discussion

#### 4.3.1. Phase fractions: Thermo-Calc vs. image analysis

Typical microstructures of bars obtained after 85% hot rolling reduction of slabs are shown in Fig. 4.3. Since hot rolling is performed in the  $\gamma+\alpha$  range, the room temperature structure basically consisted of bands of  $\alpha'$  martensite (dark) in a ferritic matrix. The bands of  $\alpha'$  are stretched along the RD and to a lesser extent along the TD. Calculated  $\gamma$  phase fractions based on Thermo-Calc and the  $\alpha'$  fractions obtained from image analysis are shown in Fig. 4.4. According to the equilibrium Thermo-Calc calculations, the stability range of  $\gamma$  is from 840 °C to 1240 °C. The maximum  $\gamma$  fraction is reached in the vicinity of 950 °C.

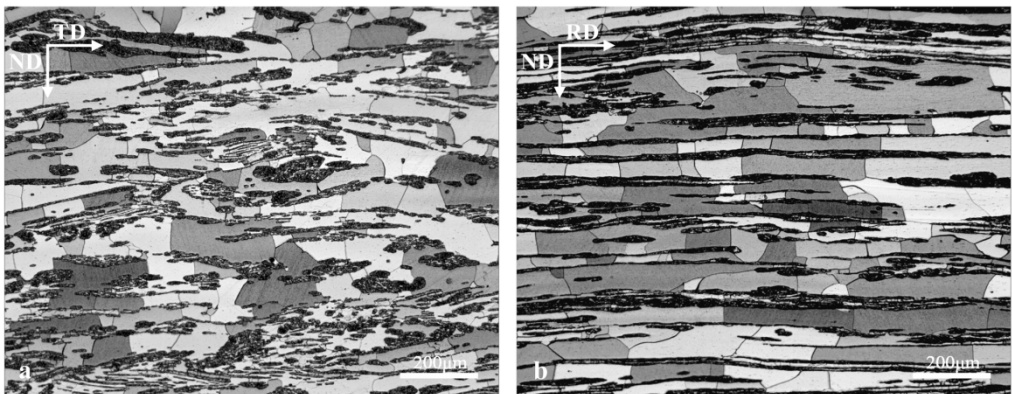


**Fig. 4.3.** Optical micrographs of the as-hot rolled material used in the dilatometry experiments showing bands of  $\alpha'$  (dark) embedded in the ferritic matrix. (a) RD section. (b) TD section.



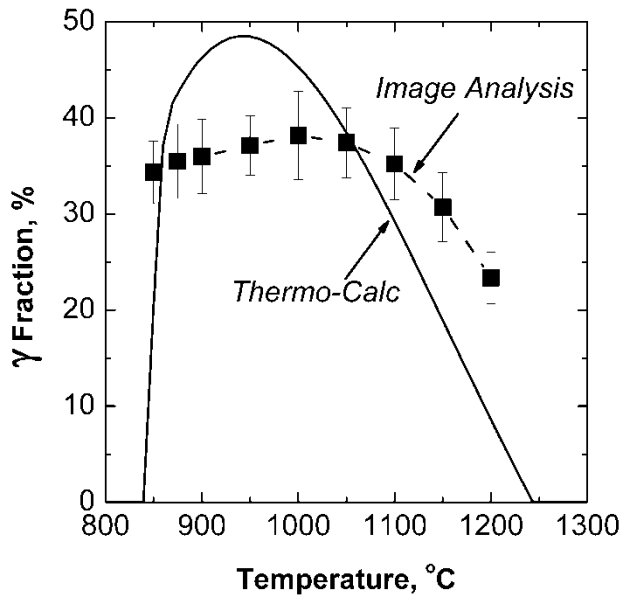


**Fig. 4.4.** Comparison of the  $\alpha'$  fractions according to the image analysis of specimens annealed for 2 min with the equilibrium  $\gamma$  fractions calculated by Thermo-Calc.

Representative optical micrographs of the specimens annealed at different temperatures are shown in Fig. 4.5. Decarburized near-surface regions of the specimen annealed at 1200 °C (Fig. 4.5(c)) were excluded from the image analysis procedure. In contrast to the calculated  $\gamma$  fractions which show a clear maximum of 48%, the  $\gamma$  fraction based on the image analysis increases from 34% at 850 °C to 38% at 1000 °C before decreasing at temperatures above 1000 °C. However, further optical microscopy examination of samples revealed that the  $\alpha$ - $\alpha'$  interfaces in the case of low annealing temperatures, especially at 850 °C (Fig. 4.5(d)), were very unclear and lacked the sharp contrast observed for high temperature samples (Fig. 4.5(e,f)). EBSD image quality maps of the samples annealed at 850 °C and 1000 °C are compared in Fig. 4.6 which suggest that the original martensite in the case of 850 °C actually consists of low image quality fresh martensite and regions with relatively high image quality corresponding to tempered martensite. In contrast, the image quality distribution is more or less uniform across the original martensite with fewer entrapped high image quality regions indicative of the dominance of the fresh martensite in the sample annealed at 1000 °C. As this type of contrast cannot be

obtained by image analysis of the optical micrographs, the difficulty of phase fraction analysis of 16%Cr stainless steel via light optical microscopy, remains.

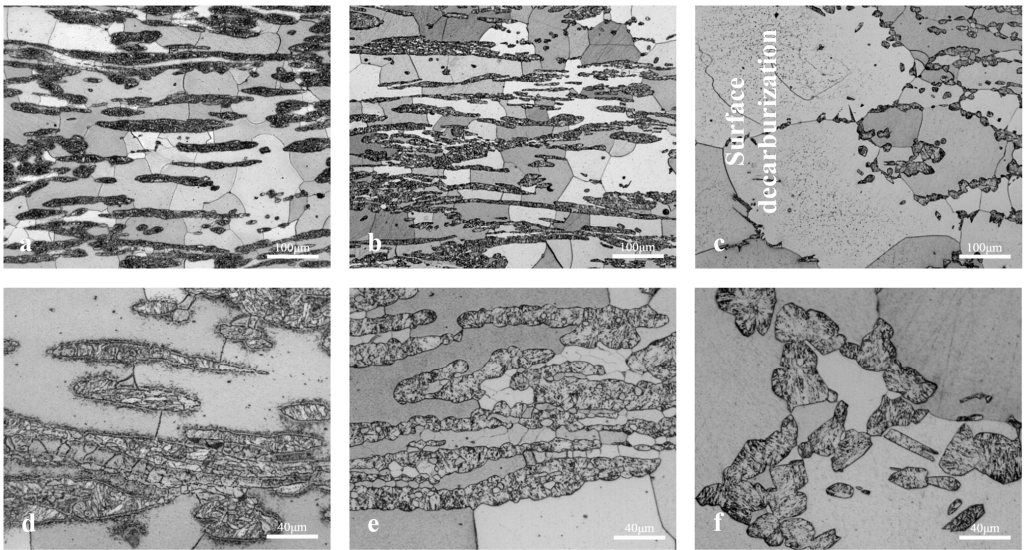


**Fig. 4.5.** Optical micrographs of the dilatometry specimens after annealing for 2 min at (a,d) 850 °C, (b,e) 1000 °C, and (c,f) 1200 °C.

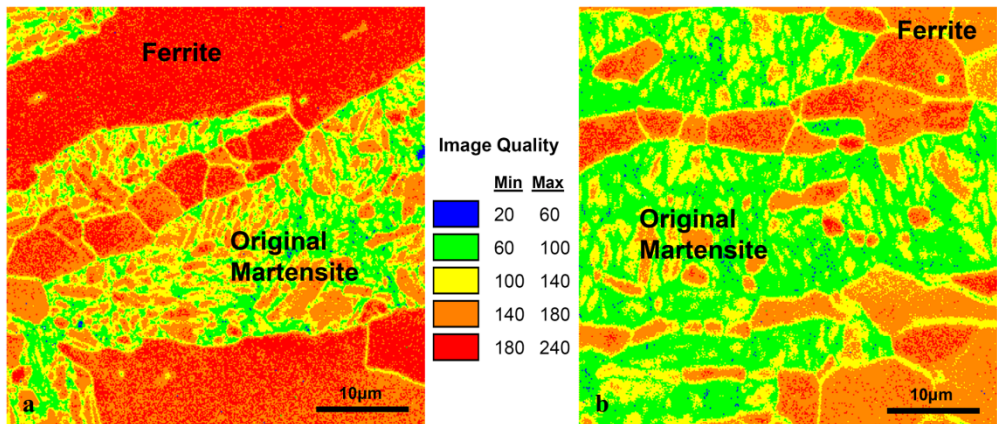


**Fig. 4.6.** EBSD image quality maps of the specimens annealed for 2 min at (a) 850 °C, and (b) 1000 °C.

#### 4.3.2. Dilatometric phase fraction analysis

As an alternative to image analysis, dilatometry can be used to determine the  $\gamma$  phase fraction as a function of temperature. In the dilatometric study of Co- and Mn-bearing

steels for instance [14], the lever rule was successfully used to calculate the fraction of austenite and ferrite in the intercritical range where the  $Ac_1$  and  $Ac_3$  temperatures can be used as the reference states with no  $\gamma$  and 100% $\gamma$ , respectively. Formation of the higher atomic density  $\gamma$  during continuous heating of  $\alpha$ , which has a lower atomic density, is associated with a decrease in the macroscopic volume of the sample which acts to decrease the slope of the general dilatometry curve. The higher CTE of austenite on the other hand tends to increase this slope. These two factors along with the width of the temperature range over which the  $\alpha \rightarrow \gamma$  transformation occurs, define the shape of the general dilatometry curve and allow to quantify the  $\gamma$  fraction as a function of temperature in the intercritical range.

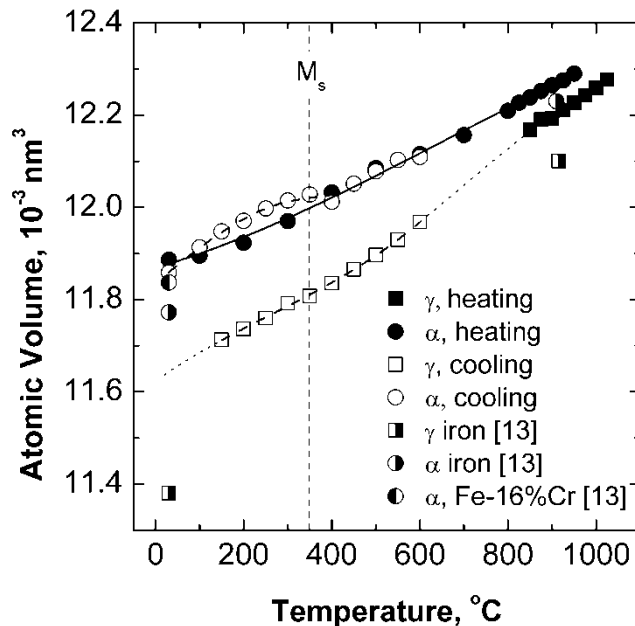


**Fig. 4.7.** Atomic volumes of  $\alpha$  and  $\gamma$  as measured by in-situ XRD. The results are for heating to 1025 °C and cooling back to RT at a rate of 1 °C/s. A holding time of 1 min at temperature was used prior to each measurement. No measurement was made in the temperature range of 600-1025 °C during cooling to achieve a maximum cooling rate of 1 °C/s and minimize austenite decomposition. For comparison, atomic volumes of pure iron and Fe-16%Cr after Ref. [13] are also reported. Note that the measured difference in atomic volume of  $\alpha$  and  $\gamma$  is appreciably higher at low temperature.

The approach explained in the preceding paragraph cannot be used in the present case as less than 50 volume-% of  $\gamma$  is formed. In-situ XRD measurements of the  $\gamma$  and  $\alpha$  atomic volumes during heating and cooling of the 16%Cr stainless steel are shown in Fig. 4.7. For comparison, specific volumes of  $\gamma$  and  $\alpha$  in the case of pure Fe and  $\alpha$  for Fe-16%Cr stainless steel based on [15] are also indicated on the graph. The small specific volume difference between the  $\gamma$  and  $\alpha$  (or  $\alpha'$ ) at the relatively elevated austenitization range of this alloy, compared to low carbon steels, leads to reduced contractions upon austenite formation which is usually considered to further deteriorate the sensitivity of the phase fraction analysis during continuous heating.

Anisotropic dimensional change of this steel after hot rolling operations is another source of complication which calls for the preparation of equi-orientation specimens in order to make meaningful comparisons. Fig. 4.8 depicts the general dilatometric curves of the three differently oriented specimens during heating to 1000 °C, holding for 2 min, followed by quenching to room temperature. The ND orientation is clearly associated with a more pronounced contraction and expansion during the austenitization and martensitic reactions, respectively. The relative volume change during austenitization of the RD, TD, and ND dilatometric specimens at a heating rate of 50 °C/min is shown in Fig. 4.9. The enhanced contraction in the ND results in reduced contractions in the RD and TD. Alternatively, the relative atomic volume change according to in-situ XRD is also shown as a reference representing the isotropic case. The phase fractions obtained from dilatometry based on the method explained in the section 3.5 were used in the calculation of atomic volumes from XRD data. The cooling signals in a temperature range in the vicinity of the  $M_s$  temperatures of the ND, RD, and TD specimens quenched from 1000 °C, are also magnified in Fig. 4.10 which again highlight the anisotropy. Dilatometric specimens taken mid-way between the RD and TD (not reported) behaved similarly implying an isotropic dilatational behavior in the RD-TD rolling plane which is significantly different from that in the ND. This anisotropy is very likely due to the geometrical arrangement of the phases in a banded microstructure. In other words, the low CTE ferrite matrix acts as a constraint against the free dimensional change of the transforming phase and

results in an orientation-dependent dimensional change due to the anisotropic morphology of the transformation products.

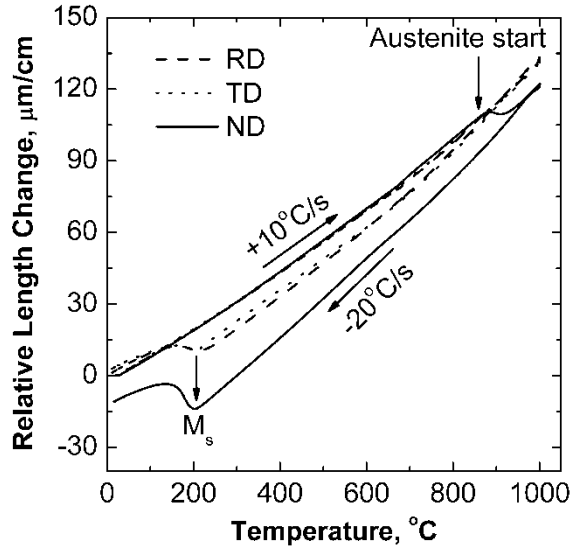


**Fig. 4.8.** Dilatometry traces of the RD, TD, and ND oriented specimens for heating to 1000 °C, and quenching to RT.

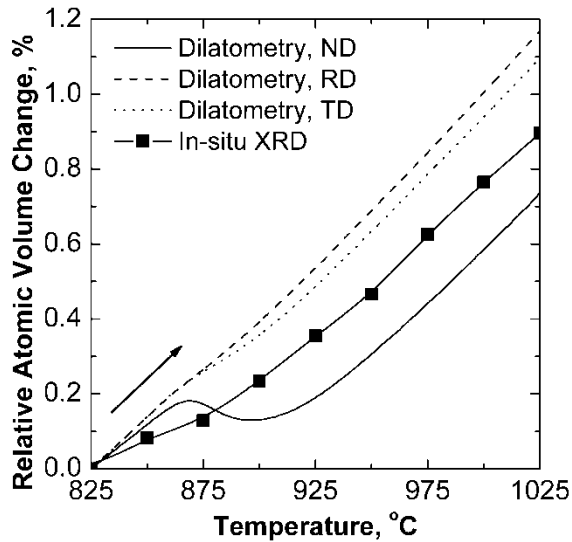


**Fig. 4.9.** Orientation and temperature dependence of the relative atomic volume change for the dilatometric specimens heated at a rate of 50 °C/min. The reference atomic volume is for a temperature of 825 °C. The value of the same parameter based on the high temperature XRD is also included in the figure.

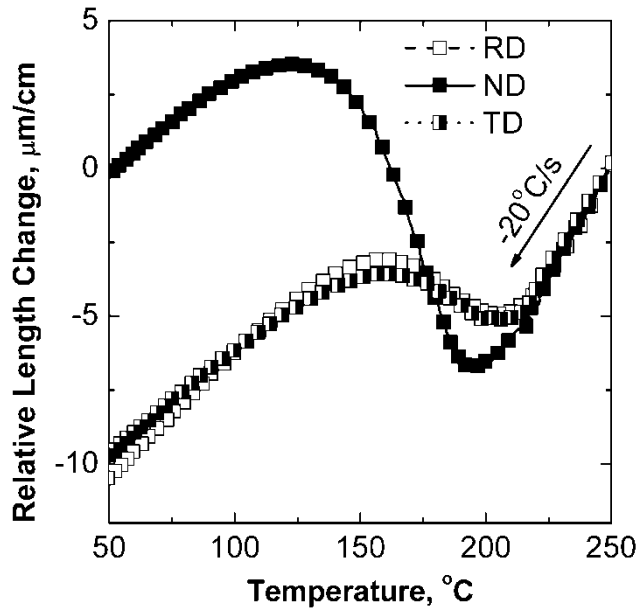


**Fig. 4.10.** Dilatometry traces of the RD, ND, and TD oriented specimens during martensitic transformation.

Due to the complexities involved, the straightforward application of the lever rule to the phase fraction analysis of the hot rolled 16%Cr stainless steel leads to erroneous results and two alternative dilatation-based methods are therefore proposed in the following paragraphs. While the first method is based on the measurement of the CTE during quenching of the annealed specimens containing various amounts of  $\gamma$ , the second relies on the measurement of dilatation due to the  $\gamma \rightarrow \alpha'$  transformation in the specimens quenched from different temperatures.

#### 4.3.3. CTE phase fraction analysis

The difference between the CTE of  $\gamma$  and that of  $\alpha$  is used in the phase fraction analysis with the CTE method. The average CTEs in the range of 0-538 °C for AISI 304 and AISI 430 as representative austenitic and ferritic stainless steels is  $18.4 \times 10^{-6} \text{ }^\circ\text{C}^{-1}$  and  $11.4 \times 10^{-6} \text{ }^\circ\text{C}^{-1}$ , respectively [16]. Hence the higher the overall CTE measured from the cooling section of the dilatometry curves in the no-transformation range, the higher the fraction of  $\gamma$ . To obtain the CTEs from the dilatometry, slopes of

the linear fits to the relative displacement-temperature curves in a temperature range between the  $M_s$  and the Curie temperature,  $T_c$ , ( $\sim 670$  °C) were measured. The fitting range was chosen far enough from the  $M_s$  and  $T_c$  temperatures to avoid the non-linearity close to these temperatures; the optimal fitting temperature range was found to be 350-550 °C. Linear fits for the ND and RD specimens quenched from 1000 °C are shown in Fig. 4.11.

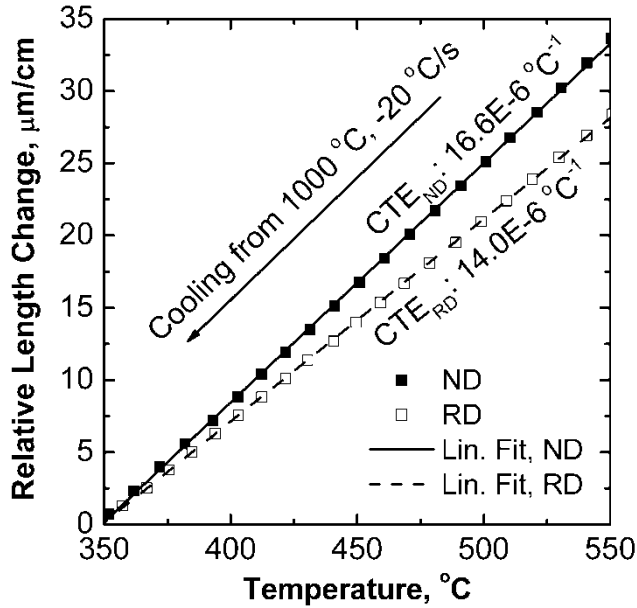


**Fig. 4.11.** Illustration of the fitting procedure used in order to determine the CTEs.

The plot of CTE versus annealing temperature for the ND and RD specimens is shown in Fig. 4.12. Although the two trends are roughly similar, large differences are observed in their absolute values. The CTE for crystals of cubic symmetry is isotropic [17], so texture differences cannot be the cause of the CTE differences along the RD and ND. The observed anisotropy is thought to be a manifestation of the geometrical constraint against the free isotropic dimensional change of the dilatometric specimens with a banded structure. In other words, during quenching,  $\gamma$ , which has a higher CTE compared to  $\alpha$ , tends to contract to a larger extent, but this is strongly opposed by the surrounding  $\alpha$  across the rolling plane.

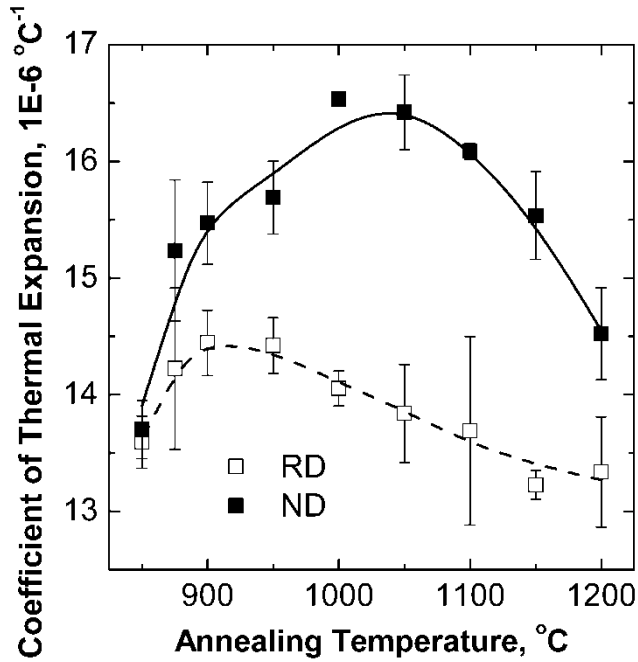


**Fig. 4.12.** Variations of CTE with annealing temperature for the ND and RD specimens. The error bars indicate the standard deviation.

In the case of a forged duplex stainless steel rod with a uniaxially anisotropic microstructure, the thermal stresses developed along the constrained direction, i.e. the rod axis, due to the dissimilar CTEs, have been expressed using the following equations [10]:

$$\sigma_{\alpha}^{\text{th}} = \frac{f_{\gamma} E_{\alpha} E_{\gamma} (\text{CTE}_{\gamma} - \text{CTE}_{\alpha}) \Delta T}{E_s} \quad (\text{Equation 4.1})$$

$$\sigma_{\gamma}^{\text{th}} = \frac{f_{\alpha} E_{\alpha} E_{\gamma} (\text{CTE}_{\alpha} - \text{CTE}_{\gamma}) \Delta T}{E_s} \quad (\text{Equation 4.2})$$

where  $E_{\gamma}$  and  $E_{\alpha}$  are the Young's moduli of the  $\gamma$  and  $\alpha$  respectively.  $E_s$  refers to the sample Young's modulus calculated by the rule of mixtures, and  $\Delta T$  is the temperature range over which the stresses have been accumulated. Due to the specific geometrical arrangement of the phases in the present study, the rolling direction of the bar can be regarded as equivalent to the axis of the forged rod since these two are the directions of the highest inter-phase coupling. As  $\alpha$  has invariably a higher volume fraction and



given the fact that it is also the stronger phase over the fitting temperature range [18], plastic deformation of  $\gamma$  which accumulates in-rolling-plane tensile stresses will be initiated when the thermal stresses exceed its yield strength. Therefore, in the constrained direction, i.e. RD,  $\alpha$  as the dominant phase will have a larger contribution to the measured CTE. Since the pancaked  $\gamma$  cannot contract freely in the rolling plane, it contracts more than the isotropic case in the ND. The high and low CTEs along the ND and RD respectively must then be a reflection of the plastic deformation of  $\gamma$  during cooling in the fitting range.

Variations of the instantaneous CTE during quenching of the RD and ND specimens from 1000°C can be seen in Fig. 4.13 where  $T_c$ , the Curie temperature, is characterized by a local minimum in the CTE as a result of small change in the atomic spacing of  $\alpha$  due to the spontaneous magnetostriction [15]. Whereas the RD specimen shows a slightly higher instantaneous CTE than the ND specimen at temperatures above  $T_c$ , the instantaneous CTE in the ND is significantly higher than that in the RD at temperatures below  $T_c$ . Hence at temperatures above  $T_c$ , it is mainly  $\alpha$  which yields in compression across the rolling plane to accommodate the larger contraction of the high CTE  $\gamma$ , even though it has a higher volume fraction. Although it was not practical to systematically apply linear fits to the dilatometry cooling curves over a wide enough range above  $T_c$  in the case of low annealing temperatures, the RD specimens exhibited a slightly higher CTE above  $T_c$  compared to the ND oriented specimens during cooling from the annealing temperatures associated with the highest  $\gamma$  contents. The observation of a sharp transition in the instantaneous CTE at  $T_c$  suggests that in addition to the contributions included in the Eqs. 1 and 2, which are only due to thermal stresses, the magnetostriction effect of the ferromagnetic transition of  $\alpha$  might also have an influence. On the other hand, the sharp transition might be related to a large drop in the yield strength of  $\alpha$  at temperatures above  $T_c$  as for instance reported in [18]. According to [18], whereas the yield strength of  $\gamma$  in a duplex stainless steel decreases by only 6 MPa from 145 MPa to 139 MPa, the yield strength of  $\alpha$  in the same alloy decreases from 250 MPa to 110 MPa, as the temperature is raised from

550 °C to 600 °C. Although the Curie temperature of  $\alpha$  in that alloy was not reported, it must lie in the range 550-600 °C based on the insight from [19].

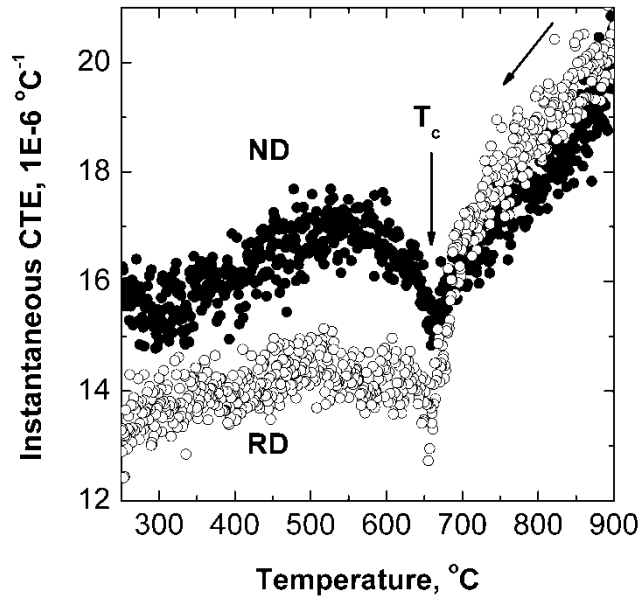


**Fig. 4.13.** Variations of the instantaneous CTE in the vicinity of  $T_c$  during quenching of RD and ND specimens from 1000 °C.

As mentioned previously, annealing at 1200 °C was associated with a narrow decarburized surface layer ( $\sim 400 \mu\text{m}$ ) consisting entirely of ferrite. Therefore, CTEs measured along any given direction of the specimen annealed at 1200 °C are expected to be slightly underestimated. As Fig. 4.5(c) shows, the geometrical arrangement of the martensite after annealing at 1200 °C is also different than at the other temperatures mostly due to its reduced continuity and the dissolution of a large fraction of the intra-granular  $\alpha'$  which means that the martensitic grains have more or less concentrated along the grain boundaries and are not necessarily extended parallel to the rolling plane. These two factors are the most likely reasons for the higher isotropy observed in the case of annealing at 1200 °C.

#### 4.3.4. Martensite dilatation phase fraction analysis

In the martensite dilatation method, the fresh  $\alpha'$  fraction in the quenched specimens is estimated directly. The atomic volume difference between the parent  $\gamma$  and the product

$\alpha'$  is large enough around the  $M_s$  temperature (see Fig. 4.7) to allow for the monitoring of even small changes in the  $\alpha$ - $\gamma$  balance in a precision dilatometer. In the dilatation method, the expansion due to the transformation of the dense  $\gamma$  to the less closely packed  $\alpha'$  is used to monitor the amount of transformed  $\gamma$ . To do so, as illustrated in Fig. 4.14, a linear fit is first applied to the cooling section of the dilatometry curves in the temperature range of 350 °C to 550 °C, as in the CTE method, and extrapolated down to 20 °C. The vertical spacing, at 20 °C, between the extrapolated line and the actual dilatometry curve is used to quantify the martensitic dilatation after making the following correction. In contrast to the fcc iron whose CTE is nearly independent of the temperature [15], the CTEs of  $\alpha$  and  $\alpha'$  increase with the temperature. Therefore, even in the absence of  $\gamma$ , some dilatation is measured when using the above procedure. To correct for this temperature dependence, the average dilatation of three specimens annealed for 2 min at 800 °C, a temperature safely below the austenitization range of the studied composition, is subtracted from all dilatation data. The correction factors amount to 2.3  $\mu\text{m}/\text{cm}$  and 3.6  $\mu\text{m}/\text{cm}$  for the RD and ND specimens, respectively.

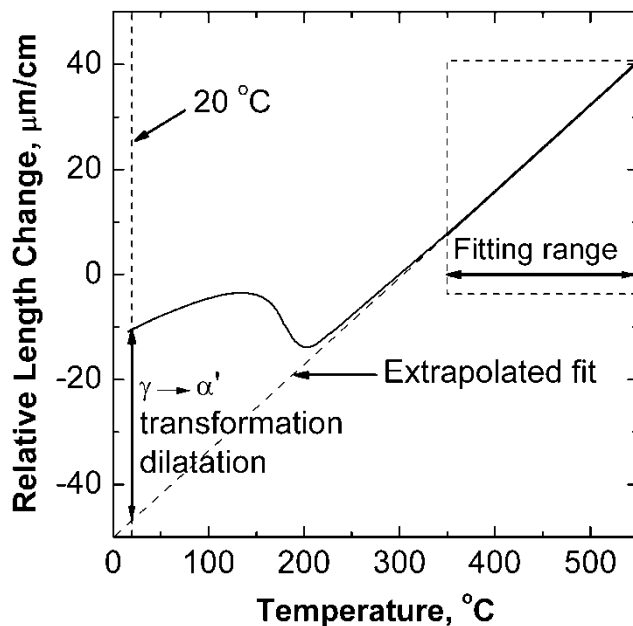


**Fig. 4.14.** Illustration of the martensite dilatation method for a ND oriented specimen quenched from 1000 °C.

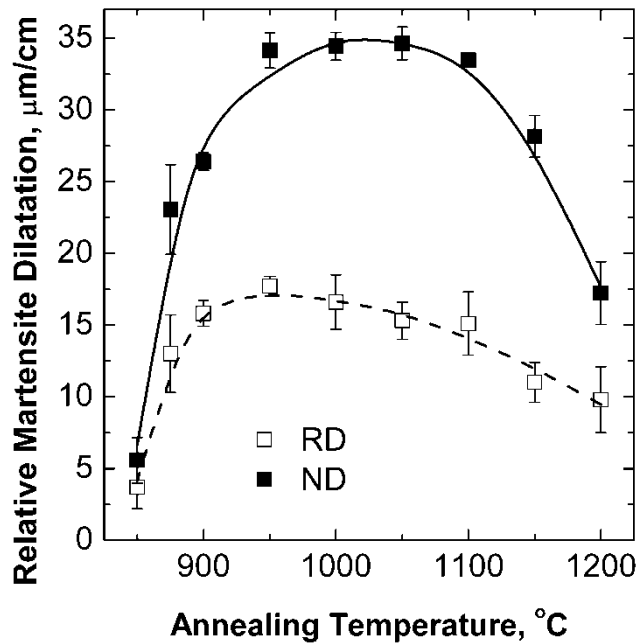


**Fig. 4.15.** Variations of martensitic dilatations with annealing temperature for ND and RD specimens. The error bars indicate the standard deviation.

The corrected dilatations for the ND and RD specimens in the studied temperature range are shown in Fig. 4.15. The  $M_s$ - $M_f$  interval in stainless steels has been reported to be typically less than 150 °C [20]. The  $M_s$  temperatures calculated by applying the Koistinen and Marburger's approach [21] to the six experiments for each annealing temperature (three with RD and three with ND orientation) are shown in Fig. 4.16. The lowest  $M_s$  temperature, 178 °C, belongs to the specimen annealed at 1200 °C signifying that for all annealing temperatures, the  $\gamma$  fully transforms to  $\alpha'$  or its fraction is negligible by the time the sample is cooled to 20 °C, the temperature at which the dilatation is measured. Therefore, in the absence of a pronounced crystallographic texture and effects due to alloying element partitioning on the expansions during the martensitic transformation, there is a direct correspondence between the CTE and the extent of the martensitic dilatation. Such a correspondence can be seen in the plots of CTE vs. dilatation for both orientations (Fig. 4.17). In the case of annealing at 850 °C, in particular in the case of RD specimens, some deviation from linearity is observed. Such a deviation might arise from either or a combination of (a) a small dilatation and

(b) a large CTE. The extent of dilatation during the martensitic reaction is well known to be a function of the interstitial solute atoms [22-23]. The small dilatation measured at 850 °C, may thus be linked to the reduced C and/or N content of  $\gamma$  as evidenced by the high  $M_s$  temperature in the case of 850 °C (Fig. 4.16). On the other hand, the large deviation at 850 °C may also be related to the presence of carbides and/or tempered martensite, both of which likely at 850 °C. This issue will be discussed later.

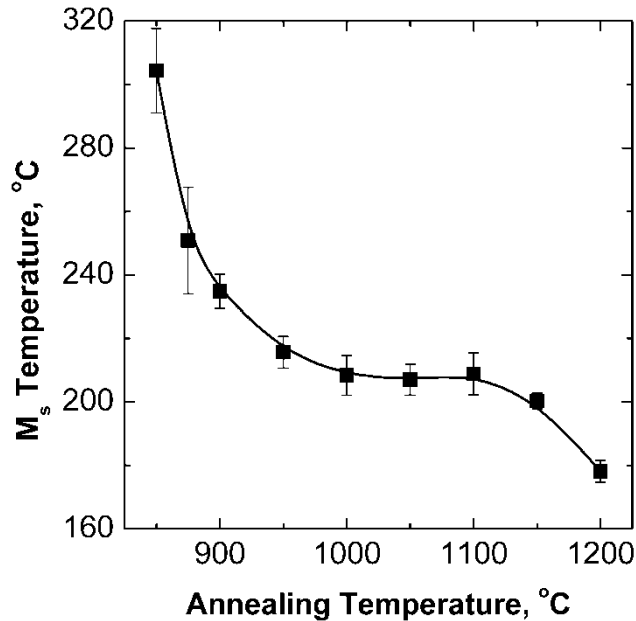


**Fig. 4.16.**  $M_s$  temperatures based on the fitting of the transformation kinetics to the Koistinen-Marburger equation. The error bars denote the standard deviation.

Initial texture of the parent  $\gamma$  and the occurrence of favored crystallographic variants of lath martensite as a result of applied stress, either external or internal, is known to lead to anisotropic transformation plasticity [24], in the simplest case visualized by the Bain strain [25]. Nevertheless, the reasonable correspondence between the CTE and the dilatation rules out the possibility of major textural influences on the observed anisotropic dilatations. This was also confirmed by the EBSD orientation map of the sample quenched from 1000 °C.

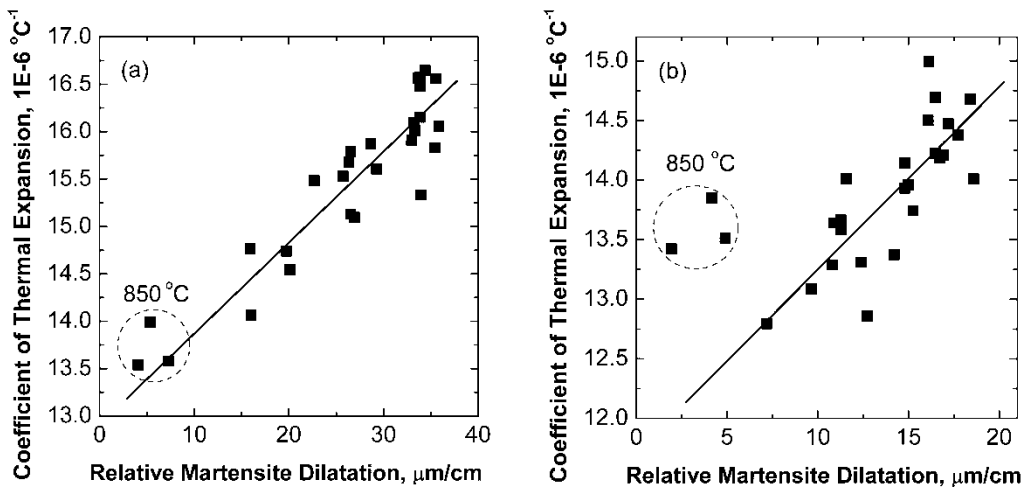


**Fig. 4.17.** Correspondence between the martensitic dilatation and the CTE for the different dilatometry experiments with (a) ND specimens and (b) RD specimens.

In order to quantify the expansion anisotropy, the ratio of the dilatation in ND and RD,  $DIL_{ND}/DIL_{RD}$ , for the different annealing temperatures is shown in Fig. 4.18. This ratio gradually rises from about 1.5 at 850 °C to more than 2.5 at 1150 °C, and drops abruptly at 1200 °C. The observed trend is expected to be a result of the change in the severity of the geometrical configuration of the phases causing the anisotropy as schematically shown in Fig. 4.19. At annealing temperatures below the one corresponding to the peak  $\gamma$  content, the fraction of the tempered  $\alpha'$  inside the original  $\alpha'$  is expected to be considerable so that the  $\gamma$  grains are relatively discontinuous. This reduces the anisotropy. As the annealing temperature increases, the tempered  $\alpha'$  fraction decreases and hence the anisotropy ratio increases. On the other hand, as the annealing temperature exceeds the peak  $\gamma$  content, the  $\gamma$  phase grains become increasingly connected and gradually start to transform to ( $\delta$ ) ferrite in such a way that the constraint leading to the anisotropy becomes increasingly serious. This could happen for instance through thinning of the  $\gamma$  bands and transformation of the entrapped  $\alpha$  or  $\alpha'$  into  $\gamma$ . At 1200 °C however, two factors, the surface decarburization and an imperfect banded structure due to the dominance of the intergranular  $\gamma$  grains, also contribute to a low anisotropy ratio at 1200 °C.

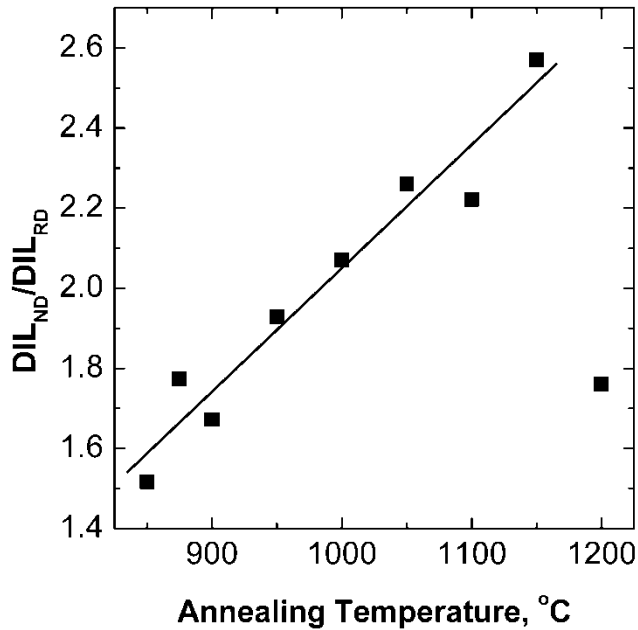


**Fig. 4.18.** Anisotropy ratio defined by the ratio of the martensitic dilatation along the ND to that along the RD plotted as a function of annealing temperature.

#### 4.3.5. Conversion of the dilatometry-based results into phase fractions

To overcome the complication caused by the anisotropy, and based on the observation of a more or less similar dilatometric behavior along the TD and RD which differs considerably from that of the ND, the CTE for different orientations is used to estimate an isotropic CTE value, using the following equation:

$$\text{CTE}_{\text{iso}} = \frac{1}{3}(\text{CTE}_{\text{ND}} + 2\text{CTE}_{\text{RD}}) \quad (\text{Equation 4.3})$$

where  $\text{CTE}_{\text{iso}}$  denotes the isotropic CTE. Assuming coexistence of  $\gamma$  and  $\alpha$  only during cooling from all intercritical annealing temperatures, the calculated isotropic CTEs are converted to  $\gamma$  volume fractions using the rule of mixtures:

$$f_{\gamma} = \frac{\text{CTE}_{\text{iso}} - \text{CTE}_{\alpha}}{\text{CTE}_{\gamma} - \text{CTE}_{\alpha}} \quad (\text{Equation 4.4})$$

In order to determine the  $\gamma$  fraction at each temperature, the CTEs of  $\gamma$  and  $\alpha$  must be known as Eq. 4.4 implies. If  $CTE_\gamma$  and  $CTE_\alpha$  are taken to be fixed values regardless of the annealing temperature, it suffices to determine them at a specific temperature and then generalize them to all annealing temperatures.

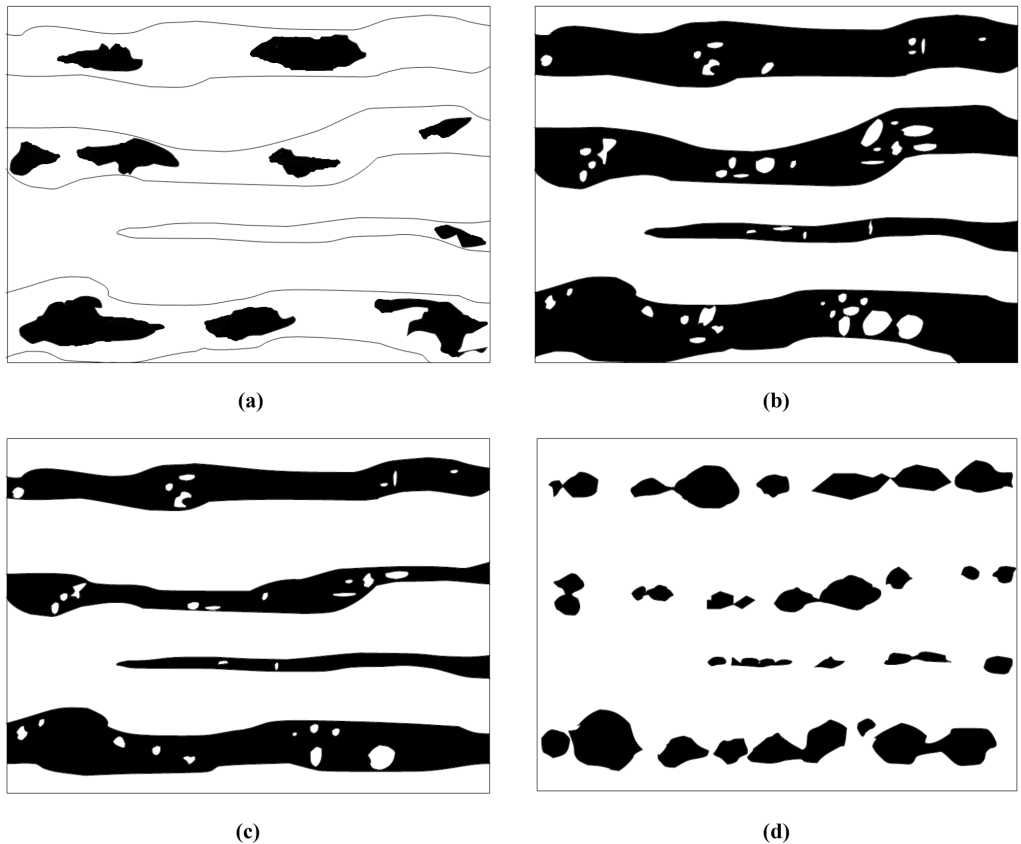


**Fig. 4.19.** Schematic showing evolution of microstructure with annealing temperature in a section containing the ND. Dark denotes the  $\gamma$  phase and white is representative of either the  $\alpha$  phase or initial martensite in the microstructure. At annealing temperatures below 900 °C,  $\gamma$  appears as isolated islands in the initially banded martensite (a) and reaches a maximum in volume fraction at about 1000 °C (b). Further increase of the temperature results in the thinning of the  $\gamma$  and a reduced fraction of entrapped  $\alpha$  (c). Eventually at 1200 °C, the continuity of  $\gamma$  is reduced. This is associated with a drastic decrease of the anisotropy ratio.



In order to find the  $CTE_{\alpha}$  without any interference from carbides and/or tempered martensite, the CTE was measured in the range of 350-550 °C after a prolonged annealing at 820°C. This CTE is for a  $\alpha$ +carbides mixture. The CTE of another 16%Cr steel with a composition containing a lower carbon content (0.023 mass%) was measured after a similar prolonged annealing treatment in the range of 350-550 °C in order to exclude the effect of carbides. The two CTEs were then extrapolated to 0 percent carbon and the result was chosen as  $CTE_{\alpha}$  ( $12.0 \times 10^{-6} \text{ }^{\circ}\text{C}^{-1}$ ). By taking the image analysis result at 1000 °C as the reference, the  $CTE_{\gamma}$  satisfying the rule of mixtures was found to be  $19.6 \times 10^{-6} \text{ }^{\circ}\text{C}^{-1}$ . Further investigations showed that the specimens held for 2 min at 800 °C, i.e. below the intercritical range, exhibited an average CTE of  $13.1 \times 10^{-6} \text{ }^{\circ}\text{C}^{-1}$ , i.e. higher than the extrapolated  $CTE_{\alpha}$ . This could be due to the presence of carbides and/or tempered martensite. Prior dilatometric investigations into the carbides dissolution had indicated that the carbides dissolve by the time the temperature reaches  $\sim 1000 \text{ }^{\circ}\text{C}$ . This temperature also coincides with the complete dissolution of the tempered martensite. Given these facts, the value of  $CTE_{\alpha}$  is assumed to linearly decrease from  $13.1 \times 10^{-6} \text{ }^{\circ}\text{C}^{-1}$  at 820 °C to  $12.0 \times 10^{-6} \text{ }^{\circ}\text{C}^{-1}$  at 1000 °C and these values are inserted into Eq. 4.4 to calculate the  $\gamma$  fraction.

By analogy with the procedure employed to convert the CTE results into the phase fractions, the isotropic dilatations are found by assuming an isotropic behavior within the RD-TD plane and using the following formula to calculate the isotropic dilatation:

$$DIL_{iso} = \frac{1}{3}(DIL_{ND} + 2DIL_{RD}) \quad (\text{Equation 4.5})$$

where  $DIL_{iso}$  denotes the isotropic dilatation, while  $DIL_{ND}$  and  $DIL_{RD}$  refer to the dilatations measured along the ND and RD. The dilatation data is subsequently converted into the  $\alpha'$  fractions by finding the proportionality constant which successfully converts the dilatation in the specimen quenched from 1000 °C to the corresponding  $\alpha'$  fraction based on the image analysis.

The  $\gamma/\alpha'$  fractions obtained from the dilatometry by means of the above procedure along with the  $\alpha'$  fractions from the image analysis are superimposed in Fig. 4.20. Since the  $\alpha'$  fraction at 1000 °C, as determined by image analysis, was used as

reference in the conversion of the dilatometric results to the phase fractions, the dilatometry-based results coincide with the image analysis results at this temperature. The difference between the image analysis and the dilatation-based methods, observed at low temperatures, is due to the presence of tempered martensite. Except for the annealing temperature of 850 °C, the CTE and dilatation methods give similar estimations of the  $\gamma/\alpha'$  fraction. The large difference between the two dilatometry-based fractions at 850 °C is a reflection of the low carbon content of  $\gamma$  as evidenced by its high  $M_s$  temperature of 304 °C. The good agreement of the dilatometry-based results at high temperatures with those obtained from image analysis strongly supports the assumption of an isotropic dilatational state within the rolling plane on grounds of the banded structure.

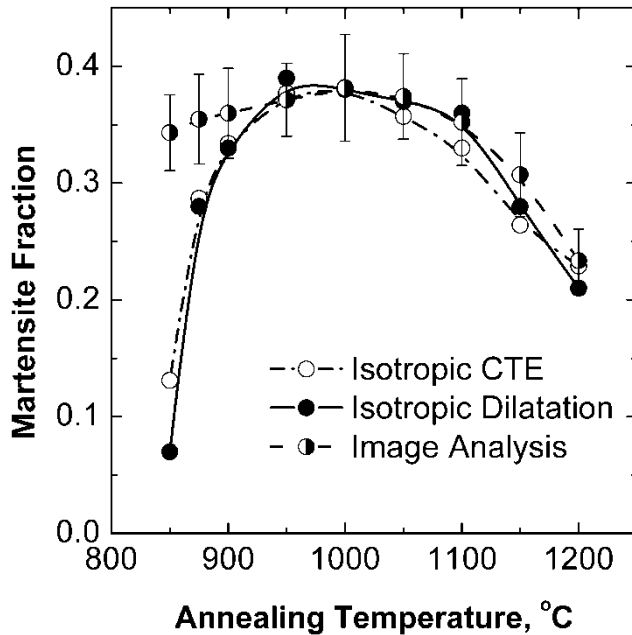


**Fig. 4.20.** Comparison of the  $\gamma$  ( $\alpha'$ ) fractions determined by dilatometry with the image analysis results. Note that the image analysis of optical micrographs overestimates the volume fraction of  $\gamma$  ( $\alpha'$ ) at low annealing temperatures. The error bars denote the standard deviation.

#### 4.4. Conclusions

The anisotropic dimensional change in a 16%Cr stainless steel with a banded microstructure consisting of  $\alpha+\alpha'$  was studied by dilatometry. The following conclusions were drawn:

- 1- A considerable transformation anisotropy was observed during both the austenitization and the martensitic reactions. In the case of the martensitic transformation, dilatations along the ND were considerably larger than along the RD after annealing in the intercritical temperature range. The ratio of dilatation along the ND to that along the RD increased when the annealing temperature increased. This was attributed to the enhancement of the banded structure and an increased constraint by the surrounding  $\alpha$ . In the case of the highest annealing temperature however, occurrence of appreciable surface decarburization and the presence of less perfectly aligned bands of  $\alpha'$  led to an abrupt drop in the anisotropy ratio.
- 2- CTEs also showed a significant direction dependence, with CTEs measured along the RD smaller than those along the ND in the temperature range between  $M_s$  and  $T_c$ . The accumulation of thermal stresses due to the difference between  $CTE_\alpha$  and  $CTE_\gamma$  leads to the plastic yielding of  $\gamma$  which is the minor phase in terms of volume fraction and also the softer phase below  $T_c$ .
- 3- The direct correspondence between the CTEs and the dilatations for each individual experiment rules out the possibility of prominent variant selection contributing to the anisotropic martensite dilatation. The correspondence however is weaker at low annealing temperatures where reduced carbon content may lead to low dilatations and other factors, such as the presence of tempered martensite and carbides, may lead to high CTEs.
- 4- Instead of using the data collected from only one set of similarly oriented specimens, a more realistic picture of the  $\alpha'$  fractions can be obtained from dilatometry by combining the results of ND and RD specimens, assuming the existence of in-rolling-plane isotropy and generalizing the dilatometric behavior of RD specimen to the whole rolling plane. Such results are especially useful when annealing specimens at low temperatures, where fresh martensite formed from  $\gamma$  and the original

martensite in the structure, which has undergone tempering during the annealing, coexist. This approach is especially useful when the lack of sufficient contrast in the optical micrographs interferes with the correct estimation by image analysis of the fresh martensite fraction at these temperatures.

#### 4.5. References

- [1] M. Gómez, *et al.*, "Modelling of Phase Transformation Kinetics by Correction of Dilatometry Results for a Ferritic Nb-microalloyed Steel," *ISIJ International*, vol. 43, pp. 1228-1237, 2003.
- [2] T. Waterschoot, *et al.*, "Tempering kinetics of the martensitic phase in DP steel," *ISIJ International*, vol. 46, pp. 138-146, 2006.
- [3] J. Z. Zhao, *et al.*, "Kinetics of phase transformations in steels: A new method for analysing dilatometric results," *ISIJ International*, vol. 41, pp. 492-497, 2001.
- [4] C. García De Andrés, *et al.*, "Application of dilatometric analysis to the study of solid-solid phase transformations in steels," *Materials Characterization*, vol. 48, pp. 101-111, 2002.
- [5] D. W. Suh, *et al.*, "Dilatometric analysis of austenite decomposition considering the effect of non-isotropic volume change," *Acta Materialia*, vol. 55, pp. 2659-2669, 2007.
- [6] D. W. Suh, *et al.*, "Dilatometric analysis of phase fraction during austenite decomposition into banded microstructure in low-carbon steel," *Metallurgical and Materials Transactions A: Physical Metallurgy and Materials Science*, vol. 38 A, pp. 2963-2973, 2007.
- [7] R. A. Jaramillo, *et al.*, "Dimensional anisotropy during phase transformations in a chemically banded 5140 steel. Part I: Experimental investigation," *Acta Materialia*, vol. 52, pp. 851-858, 2004.
- [8] R. A. Jaramillo and M. T. Lusk, "Dimensional anisotropy during phase transformations in a chemically banded 5140 steel. Part II: Modeling," *Acta Materialia*, vol. 52, pp. 859-867, 2004.

- [9] M. Farooque, *et al.*, "Dimensional anisotropy in 18 pct Ni maraging steel," *Metallurgical and Materials Transactions A: Physical Metallurgy and Materials Science*, vol. 32, pp. 1057-1061, 2001.
- [10] T. Siegmund, *et al.*, "The irreversible deformation of a duplex stainless steel under thermal cycling," *Materials Science and Engineering A*, vol. 169, pp. 125-134, 1993.
- [11] F. D. Fischer, *et al.*, "Fatigue and fracture of high-alloyed steel specimens subjected to purely thermal cycling," *Metallurgical Transactions A*, vol. 21, pp. 935-948, 1990.
- [12] N. Mary, *et al.*, "Finite-element and XRD methods for the determination of the residual surface stress field and the elastic-plastic behaviour of duplex steels," *Philosophical Magazine*, vol. 85, pp. 1227-1242, 2005.
- [13] J. Mola, *et al.*, "Influence of texture on ridging and formability of 16%Cr ferritic stainless steel," *Diffusion and Defect Data Pt.B: Solid State Phenomena*, vol. 160, pp. 153-158, 2010.
- [14] Y. C. Liu, *et al.*, "Abnormal austenite-ferrite transformation behaviour in substitutional Fe-based alloys," *Acta Materialia*, vol. 51, pp. 507-519, 2003.
- [15] W. Pepperhoff and M. Acet, *Constitution and Magnetism of Iron and Its Alloys*, 2001.
- [16] S. D. Washko and G. Aggen, *ASM Handbook*, vol. 1, p. 871, 1993.
- [17] T. H. K. Barron, *Thermal Expansion of Solids, Vol. I-4 of CINDAS Data Series on Materials Properties*, p. 6, 1998.
- [18] T. Siegmund, *et al.*, "On the thermomechanical deformation behavior of duplex-type materials," *Journal of the Mechanics and Physics of Solids*, vol. 43, pp. 495-501,503-532, 1995.
- [19] S. S. M. Tavares, *et al.*, "Magnetic properties of the UNS S39205 duplex stainless steel," *Journal of Alloys and Compounds*, vol. 351, pp. 283-288, 2003.
- [20] D. Peckner and I. M. Bernstein, *Handbook of Stainless Steels*, pp. 15.1-15.6, 1977.

- [21] D. P. Koistinen and R. E. Marburger, "A general equation prescribing the extent of the austenite-martensite transformation in pure iron-carbon alloys and plain carbon steels," *Acta Metallurgica*, vol. 7, pp. 59-60, 1959.
- [22] L. Cheng, *et al.*, "Lattice parameters of iron-carbon and iron-nitrogen martensites and austenites," *Scripta Metallurgica et Materiala*, vol. 24, pp. 509-514, 1990.
- [23] J. M. Moyer and G. S. Ansell, "The volume expansion accompanying the martensite transformation in iron-carbon alloys," *Metallurgical Transactions A*, vol. 6, pp. 1785-1791, 1975.
- [24] H. K. D. H. Bhadeshia, "Material factors," *Handbook of Residual Stress and Deformation of Steel*, pp. 3-10, 2002.
- [25] H. Miyaji and E. I. Furubayashi, *Text. Microstr.*, vol. 22, pp. 43-51, 1993.



# Chapter V

## Cold Rolling of Unannealed Hot Strips

### **5.1. Introduction**

There have been numerous modeling attempts, some of which discussed in chapter I, to correlate the texture and the ridging severity of ferritic stainless steel sheets. Although these models have contributed to a better understanding of the ridging mechanism, they remain qualitative and do not provide practical guidelines to alleviate ridging. The experimental assessment of the effect of composition on the microstructural evolution, and eventually the ridging resistance, needs to be further explored while monitoring other parameters of importance to formability such as the normal anisotropy. Based on the results, an alloy design concept associated with superior ridging characteristics in the AISI 430 ferritic stainless steel is introduced. In addition to the effect of chemical composition, effect of elimination of the homogenization annealing step of hot strips on the ridging resistance and formability of sheets will be discussed.

### **5.2. Experimental Procedure**

Three variants of the AISI 430 ferritic stainless steel namely low C (steel A), standard (steel B), and Al-added (steel C) with compositions given in Table 3.1 were used in the present study.



Hot rolled strips with a thickness of 3 mm were used as the feedstock for the cold rolling operations. They were obtained by rough rolling and finish rolling of slabs. Sheets with an identical final thickness of approximately 0.6 mm were obtained after processing of hot rolled strips according to the two processing routes denoted HCA (Hot rolled, Cold rolled, and Annealed) and HACA (Hot rolled, Annealed, Cold rolled, and Annealed), shown schematically in Fig. 5.1. In the HACA route, hot rolled strips were homogenization annealed prior to cold rolling, and recrystallization annealed at 1093 K (820 °C) after cold rolling. In the HCA route, the hot rolled strips were directly cold rolled and homogenization annealing at 1093 K (820 °C) for five hours followed.

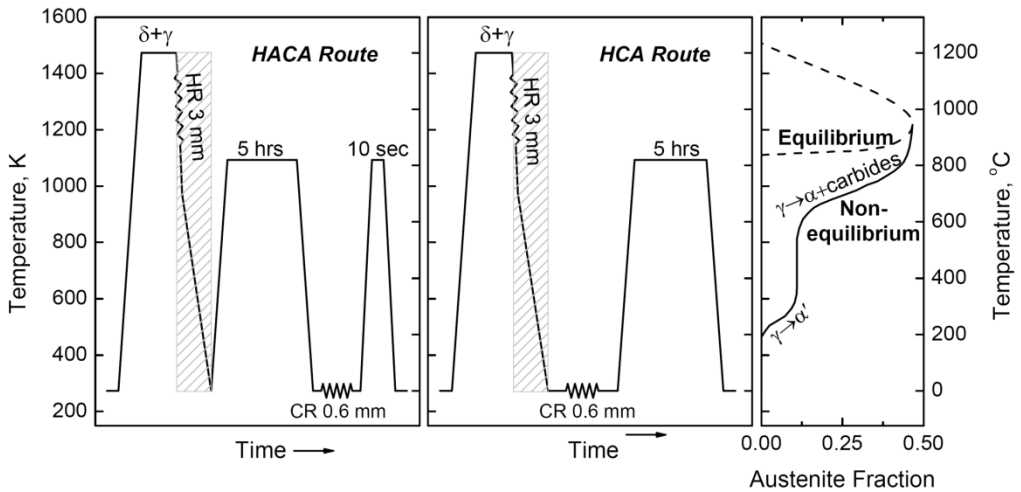


**Fig. 5.1.** Schematic of the simulated thermo-mechanical processing routes. HR and CR denote Hot Rolling and Cold Rolling, respectively. The equilibrium  $\gamma$ -phase fraction change during hot rolling (hatched region) of a typical AISI 430 is also shown and compared schematically with the non-equilibrium fractions encountered in practice.

Fig. 5.1 also shows schematically the evolution, during hot rolling, of the  $\gamma$ -phase fraction under equilibrium and non-equilibrium conditions. For a typical AISI 430 composition, equilibrium predicts absence of the  $\gamma$ -phase at temperatures below approximately 1123 K (850 °C). In practice, non-equilibrium conditions prevail and

the  $\gamma$ -phase present during hot rolling partially decomposes to  $\alpha$ -phase and carbides in the temperature range of 873-1073 K (600-800 °C), where the decomposition rate is high, and the remaining  $\gamma$ -phase undergoes a martensitic transformation below the  $M_s$  temperature. Therefore, the  $\gamma$ -phase transformation products consist of transformed  $\alpha$ -phase,  $\alpha'$  martensite, and carbides.

The microstructure of the hot rolled strip was investigated in a JEOL JEM-2100F FEG-Scanning Transmission Electron Microscope (STEM) operated at 200 kV. Dilatometry was used to estimate the high temperature  $\gamma$ -phase fraction based on the amount of martensitic dilatation.

The sheets were compared in terms of their ridging resistance by measuring the roughness profile in the transverse direction (TD) of tensile specimens prestrained 15% along the RD. The roughness parameter  $R_t$  was measured over spans of 10 mm in 5 different locations within the gauge length of specimens prepared according to the ASTM E8 standard. ASTM E8 standard tensile specimens were also used for automatic r-value measurement according to the procedure explained in 2.5.

SEM with a field emission type gun was used to examine the microstructure of etched specimens. It was also used for the EBSD measurements. Texture inhomogeneities are usually present through the thickness of rolled products. EBSD measurements were performed on the full RD section of sheets, to evaluate the effect of processing on the overall texture and for correlation with the r-values. In contrast, ridging is considered to be related to the texture in the midthickness plane of sheets. The midthickness ND planes of sheets were therefore also examined in order to identify the texture bands usually linked to ridging. To do so, rectangular areas extending 3.3 mm in the TD and 1.1 mm in the RD were scanned.

EPMA was used to determine the elemental distribution of Al and study the AlN dissolution behavior in steel C. 3 mm-thick specimens taken from finish rolled hot strips were used in the EPMA studies after annealing for 1 minute in the temperature range of 1173-1473 K (900-1200 °C).

A Bruker X-ray diffractometer equipped with a Cu tube was utilized to measure the lattice parameter of the  $\gamma$ -phase in the 1198-1323 K (925-1050 °C) temperature range,

using a step size of  $0.02^\circ$  and a dwell time per step of 0.1 sec. Using an evacuated heating stage equipped with a radiation heater, specimens with a thermo-mechanical history identical to the dilatometry specimens were heated at an average heating rate of 0.5 K/s. Measurements were performed on planes normal to the TD in the  $2\theta$  range of  $42.4\text{--}45.1^\circ$ . The lattice parameter was calculated on the basis of the  $(111)_\gamma$  peak position.

### 5.3. Results

The temperature dependence of the equilibrium  $\gamma$ -phase fraction, calculated by means of Thermo-Calc using the TCFE6 database, is shown in Fig. 5.2. The calculations predict that the maximum  $\gamma$ -phase fraction in steel B is slightly higher than steel A. The maximum  $\gamma$ -phase fraction for steel C is between that of steel A and steel B. The  $\gamma$ -phase fraction of steel C is higher than that of the other two compositions at high temperatures. As shown in Fig. 5.3, this is related to the gradual dissolution of AlN in the steel C that proceeds at temperatures up to 1588 K (1315  $^\circ\text{C}$ ).

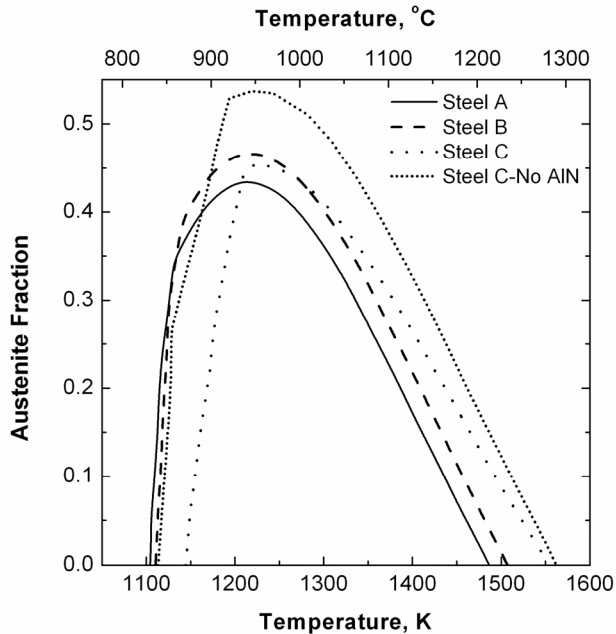


**Fig. 5.2.** Thermo-Calc calculations of the equilibrium  $\gamma$ -phase fraction. For steel C,  $\gamma$ -phase fraction in the absence of AlN is also shown.

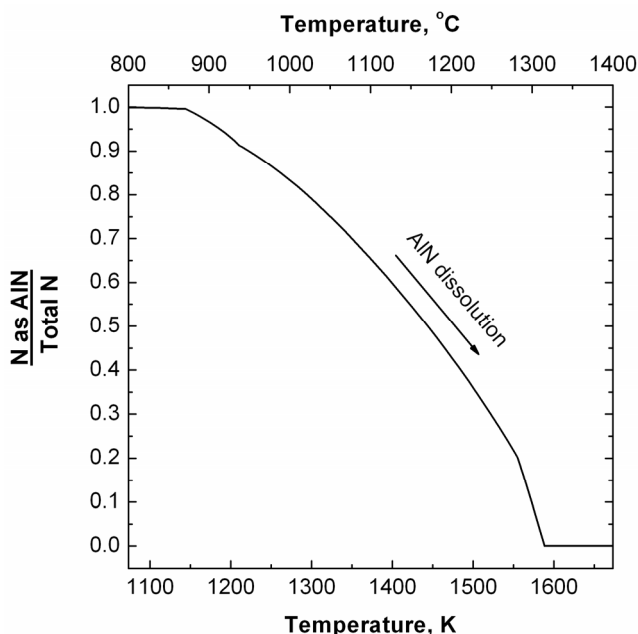


**Fig. 5.3.** Thermo-Calc calculations of the equilibrium AlN formation in steel C.

Also shown in Fig. 5.2, is the  $\gamma$ -phase fraction of steel C when the AlN phase is excluded from the thermodynamic calculations. The higher solute N content of steel C in this case increases the  $\gamma$ -phase fraction compared to the equilibrium phase fraction in the presence of AlN. Due to the low Al content of steels A and B, the amount of N that can be combined with Al is very limited ( $<0.002$  mass-%). Therefore, the solute N content of steels A and B can be assumed to be identical to the nominal N content.

The temperature dependence of the  $\gamma$ -phase fraction for the different steels, estimated by means of the martensitic dilatation measurement in dilatometry, is shown in Fig. 5.4. The  $M_s$ - $M_f$  temperature interval for stainless steels is typically less than 150 K [1]. Given that 443 K (170 °C) was the lowest  $M_s$  temperature measured for all intercritical annealing temperatures, the retained  $\gamma$ -phase fraction is expected to be zero or negligible at 293 K (20 °C), indicating that martensitic dilatations are proportional to the high temperature  $\gamma$ -phase fractions. Results in Fig. 5.4 indicate a large deviation from the equilibrium profiles of Fig. 5.2 especially in the case of steel C. Whereas the equilibrium calculations predict a sharp  $\gamma$ -phase fraction profile due to the rapid drop of the  $\gamma$ -phase fraction after the maximum, the dilatometry results

indicate a broader  $\gamma$ -phase profile, *i.e.* a less steep  $\gamma$ -phase fraction profile after the maximum. Comparing the dilatometry results of steels A and B, not only do the interstitials increase the peak  $\gamma$ -phase fraction, but they also tend to broaden the profile.

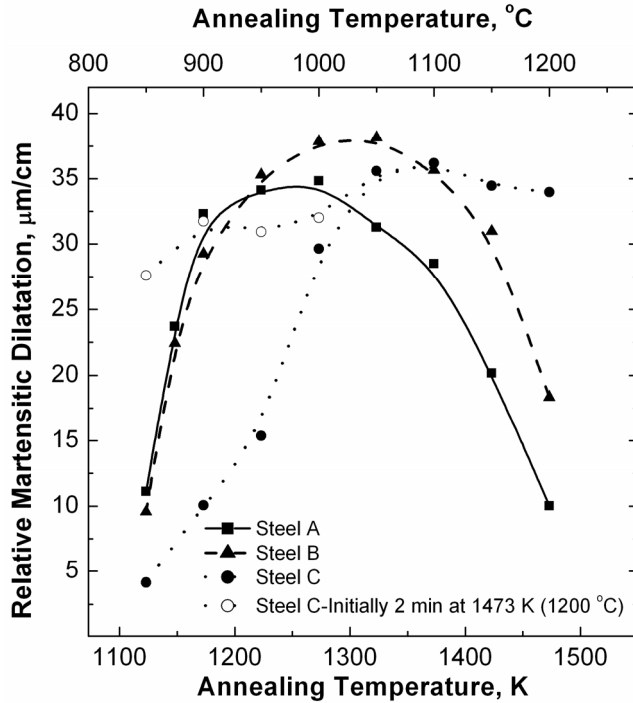


**Fig. 5.4.** Experimental martensitic dilatations in samples parallel to the ND of hot rolled slabs. They can be used as a measure of relative  $\gamma$ -phase fraction evolution.

Samples were quenched to 293 K (20 °C) after 2 minutes of annealing at each temperature. Initial annealing of steel C at 1473 K (1200 °C) leads to a significant increase in the dilatation below 1273 K (1000 °C).

Profilometry results taken along the TD of prestrained tensile specimens are shown in Fig. 5.5. Regardless of the processing route, steels B and C are associated with the best and the worst ridging resistance, respectively. As for the effect of processing, the HCA processed sheets exhibit a superior ridging resistance compared to their HACA counterparts. The microstructure before cold rolling of the HACA processed sheets consisted of a homogenous  $\alpha$ -phase matrix with embedded  $M_{23}C_6$  precipitates. In the HCA route, on the other hand, a banded microstructure consisting of untransformed  $\alpha$ -

phase and  $\gamma$ -phase transformation products was cold rolled. For both HACA and HCA routes, AlN precipitates were also present in the microstructure of the steel C. The profilometry results suggest the beneficial effect of the presence of  $\gamma$ -phase transformation products during cold rolling on the texture development during cold rolling and recrystallization annealing that follows.

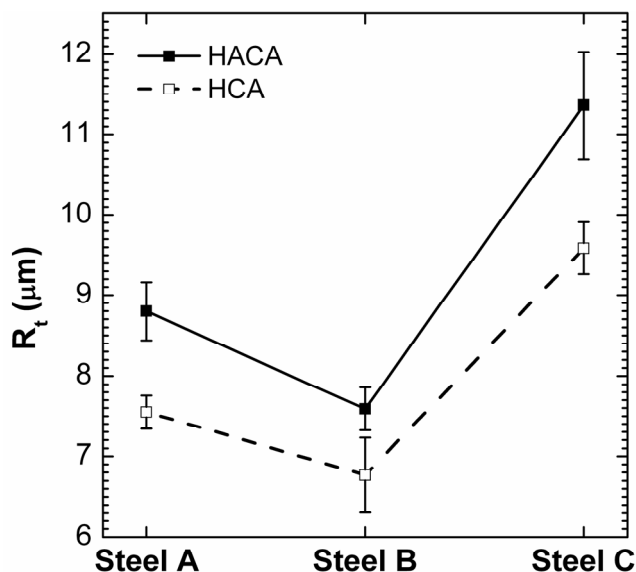


**Fig. 5.5.** Ridging heights,  $R_t$ , as measured by profilometry, in the transverse direction, of tensile specimens prestrained 15% along the RD. Error bars denote the standard deviation.

The  $\gamma$ -phase transformation products in the starting hot rolled strips were found to consist of  $\alpha$ -phase,  $M_{23}C_6$  carbides and, occasionally,  $\alpha'$  martensite, as shown in the cross sectional TEM micrographs of steel A shown in Fig. 5.6. Steel B was also found to have a microstructure comparable to that of steel A. Due to the low cooling rate after hot rolling, the  $\gamma$ -phase present after the last hot rolling pass partially decomposes to  $\alpha$ -phase and  $M_{23}C_6$  carbides at high temperatures. The remaining  $\gamma$ -phase eventually transforms to  $\alpha'$  martensite when the  $M_s$  temperature is reached.

TEM micrographs of hot rolled strip of steel C are shown in Fig. 5.7. In contrast to the microstructure of steels A and B which contains carbides less than  $0.1 \mu\text{m}$  in size,

carbides in the steel C were found to have a broader size distribution (Fig. 5.7(a,b)) with a large volume fraction of carbides exceeding 0.1  $\mu\text{m}$  and sometimes up to 0.5  $\mu\text{m}$  in size. These carbides were formed during the slow cooling to room temperature of the hot rolled strip. EDS spectra of the matrix (P1 in Fig. 5.7(b)), a Cr-rich precipitate (P2 in Fig. 5.7(b)), and an Al-rich precipitate (P3 in Fig. 5.7(c)) are shown in Fig. 5.7(d).

Using Selected Area Diffraction (SAD) analysis, the Cr-rich precipitates were found to have an FCC crystal structure with a lattice parameter of approximately 1.05 nm, *i.e.* within the reported values of 1.05~1.074 nm for the  $\text{M}_{23}\text{C}_6$  (M representing Cr and Fe) type carbides [1-6], commonly found in stainless steels.  $\text{M}_6\text{C}$  (M representing Cr, Fe, and Mo) is another common carbide in the stainless steels with an FCC crystal structure and a lattice parameter of 1.085~1.128 nm [2-6], slightly larger than that of the  $\text{M}_{23}\text{C}_6$  type carbides. There is evidence that  $\text{M}_6\text{C}$  forms from  $\text{M}_{23}\text{C}_6$  when the Mo content of the precipitates increases [1]. Although  $\text{M}_{23}\text{C}_6$  and  $\text{M}_6\text{C}$  have fairly similar lattice parameters, they belong to different space groups (Fm3m for  $\text{M}_{23}\text{C}_6$  and Fd3m for  $\text{M}_6\text{C}$ ). This difference can be used for a more reliable discrimination of these carbides. Due to the crystal symmetry in the Fd3m space group, structure factor for the  $hk0$  reflections with  $h+k \neq 4n$  is zero. Therefore, such reflections will be absent in the SAD pattern taken parallel to the  $[001]$  zone axis [2-4]. It must be noted that in SAD patterns taken from zone axes other than the  $[001]$ , the forbidden reflections in the  $\text{M}_6\text{C}$  may appear due to the multiple diffraction. The SAD pattern, parallel to the  $[001]$  crystal direction of the precipitate shown in Fig. 5.7(e) shows the presence of the  $\{200\}$  reflections. The carbides in the hot rolled strip microstructure are therefore  $\text{M}_{23}\text{C}_6$  type carbides.

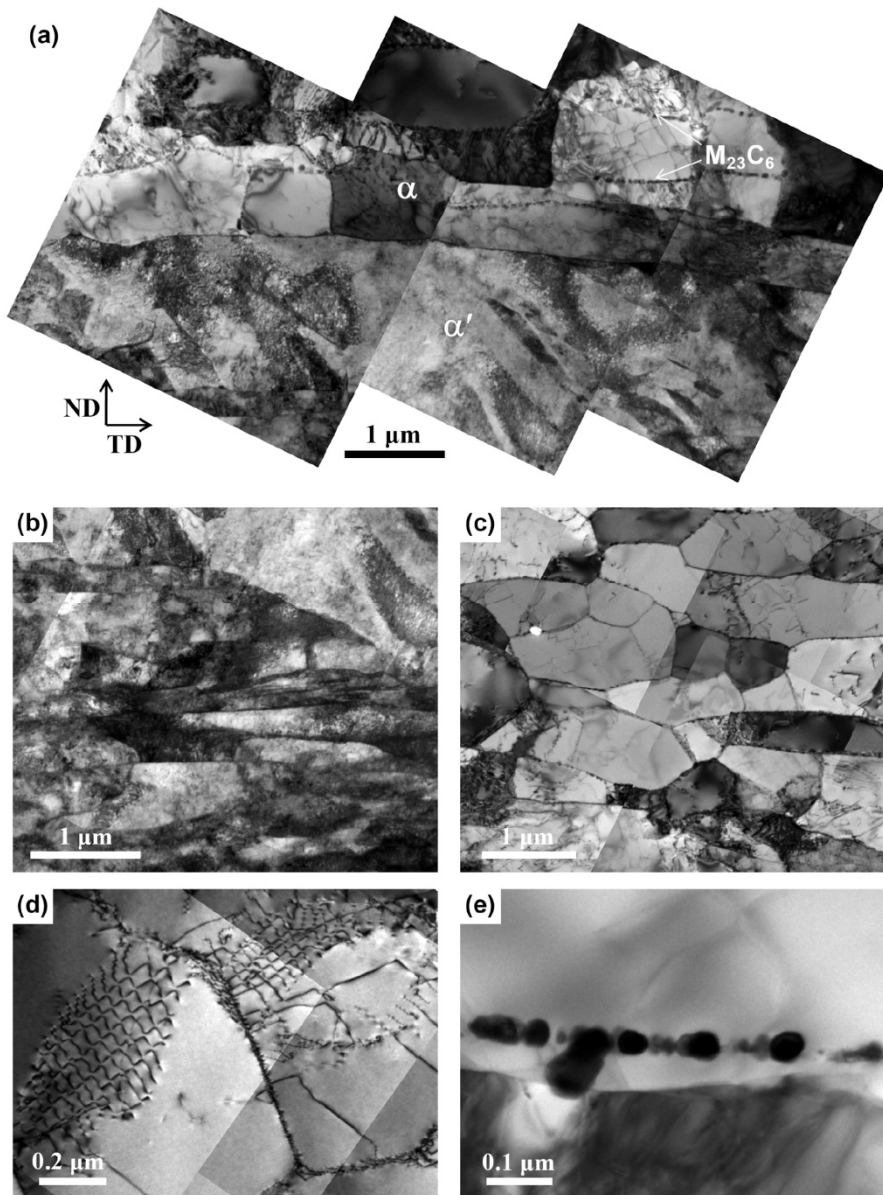


**Fig. 5.6.** (a) Composite TEM micrograph showing the microstructure of the transformed  $\gamma$ -phase regions in the hot rolled strip of steel A. Due to the low cooling rate after hot rolling, the  $\gamma$ -phase decomposes mainly into ferrite (c) and  $M_{23}C_6$  carbides (e) at high temperatures. The remaining  $\gamma$ -phase eventually transforms to  $\alpha'$  martensite (b) at lower temperatures. The untransformed  $\alpha$ -phase with a recovered microstructure is shown in (d).



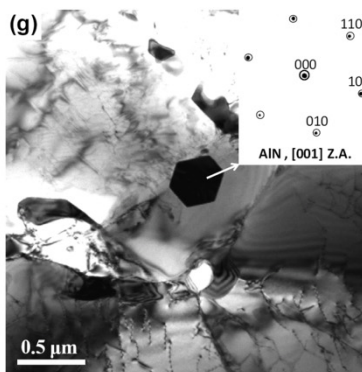
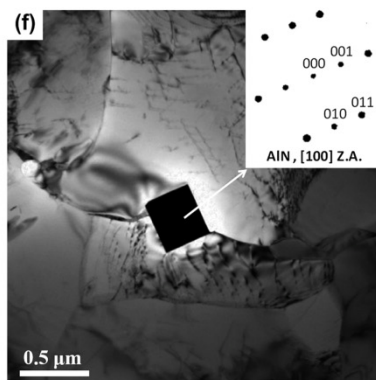
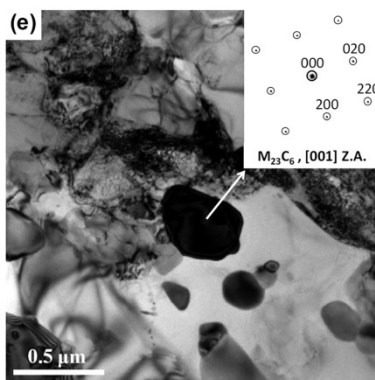
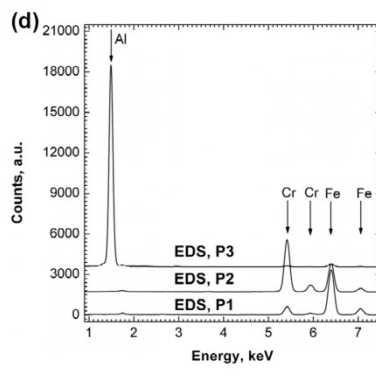
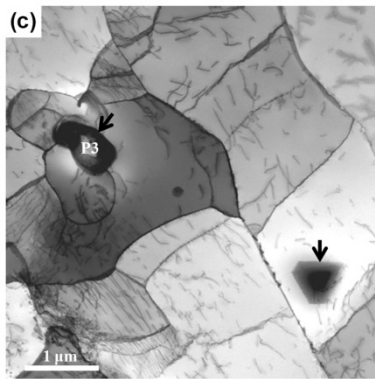
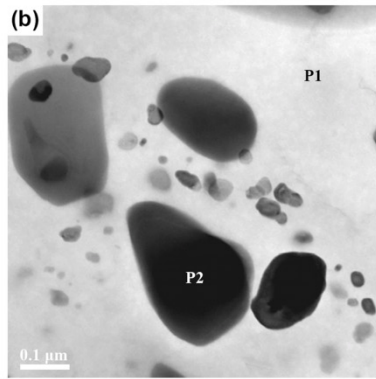
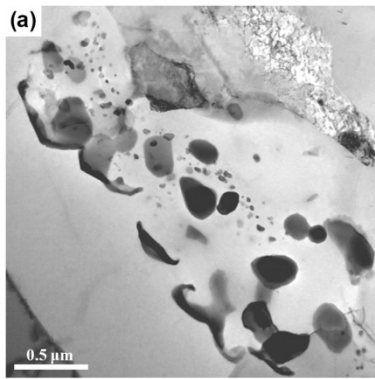


**Fig. 5.7.** STEM (a-c) and TEM (e-g) micrographs of the hot rolled strip of steel C.  $M_{23}C_6$  carbides are shown in (a,b). (c) shows two AlN precipitates, marked by arrows, in the untransformed  $\alpha$ -phase. EDS spectra of the spots P1, P2, and P3 marked in (b) and (c), corresponding to matrix,  $M_{23}C_6$ , and AlN respectively, are shown in (d). SAD patterns of the [001] zone axis of an  $M_{23}C_6$  precipitate is shown in (e). (f) and (g) show the [100] and [001] zone axes of two differently oriented AlN precipitates, respectively.

The Al-rich precipitates in the steel C were also analyzed by means of electron diffraction. SAD pattern analysis of the precipitates shown in Fig. 5.7(f,g) confirms that it has an HCP crystal structure, with a and c axes measuring about 0.31 nm and 0.50 nm, respectively. These values closely match the reported a and c values of the hexagonal wurtzite type AlN ( $a=0.311$  nm,  $c=0.498$ ) [7-9]. It must be noted that the presence of the forbidden {001} reflections in the [100] zone axis SAD pattern of Fig. 5.7(f) is due to the multiple diffraction.

EBSD orientation distribution functions (ODFs) obtained from the RD plane of sheets are shown in Fig. 5.8. They indicate a strengthening of  $\alpha$ -fiber orientations, *i.e.*  $\langle 110 \rangle // RD$ , at the expense of the  $\gamma$ -fiber orientations, *i.e.*  $\langle 111 \rangle // ND$ , and thus a more random texture, when changing from a standard HACA processing to the HCA processing route.

Fig. 5.9 shows the angular dependence of r-value for steel A, B, and C processed according to the HACA and HCA routes. The HACA processing is associated with an r-value trend characterized by  $r_{90} > r_0 > r_{45}$  except for the steel C in which  $r_{45} > r_0$ . In contrast to the HACA processing in which r-value is lowest at 45 ° to RD, the HCA processing is associated with the highest r-value at 45 ° to RD.

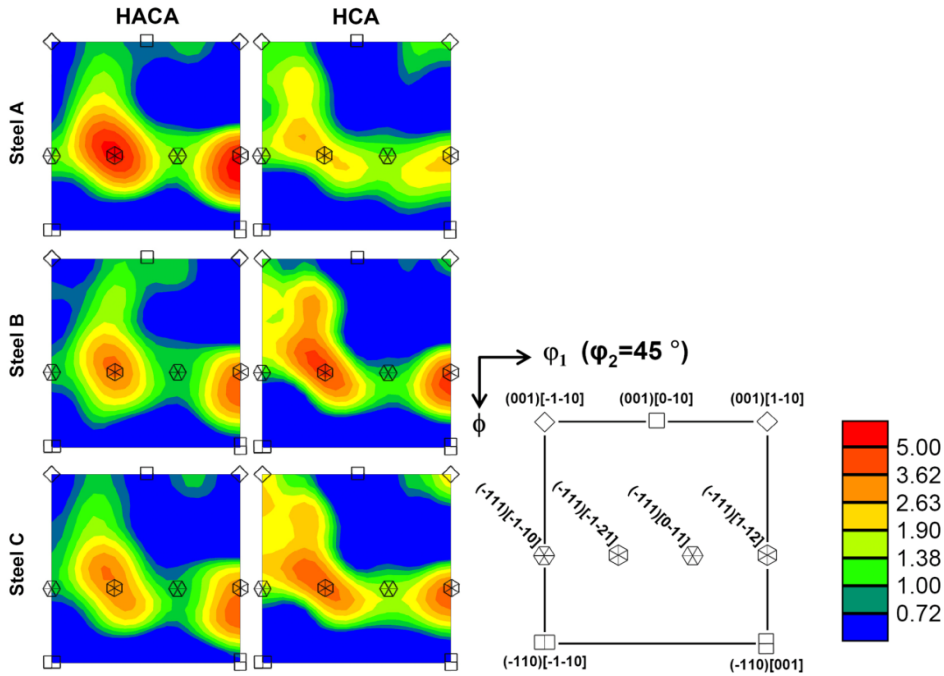


**Fig. 5.8.** EBSD ODFs taken from the full RD section of sheets.

Fig. 5.10 shows ND and RD orientation maps and their corresponding ODFs, obtained from the midthickness ND plane of sheets. Texture banding parallel to the RD can be observed in all samples. However, the texture bands vary in type, width, and spacing from one sample to the other.

## 5.4. Discussion

### 5.4.1. The $\gamma$ -Phase Fraction Evolution

The  $\gamma$ -phase fraction in the transformable ferritic stainless steels is mainly controlled by the interstitial alloying element content. For example, the equilibrium calculations of Fig. 5.2 demonstrate that in the absence of AlN, steel C which has the highest interstitials content shows the highest  $\gamma$ -phase fraction, followed by steels B and A. In practice, however, AlN formation takes place readily in the transformable ferritic stainless steels. Microstructural examinations indicated presence of the AlN in the microstructure of the as-cast slab and the hot rolled strip of steel C. In the aluminum-killed carbon steels which are hot rolled in the  $\gamma$ -phase stability range, the

AlN formation in the hot rolled strip can be suppressed with relative ease by the combination of a high finish rolling temperature and a low coiling temperature [10]. Therefore, it is the coexistence of  $\alpha$ -phase and  $\gamma$ -phase which accelerates the AlN formation in the transformable ferritic stainless steels.

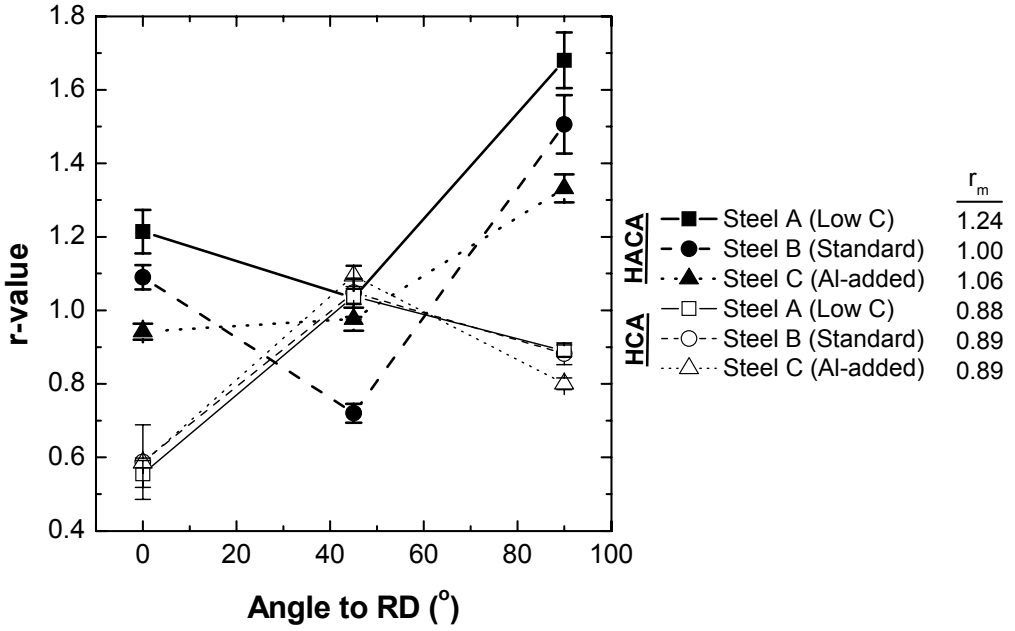


**Fig. 5.9.** Angular dependence of r-value and mean r-values for steels A, B, and C processed according to HCA and HACA routes.

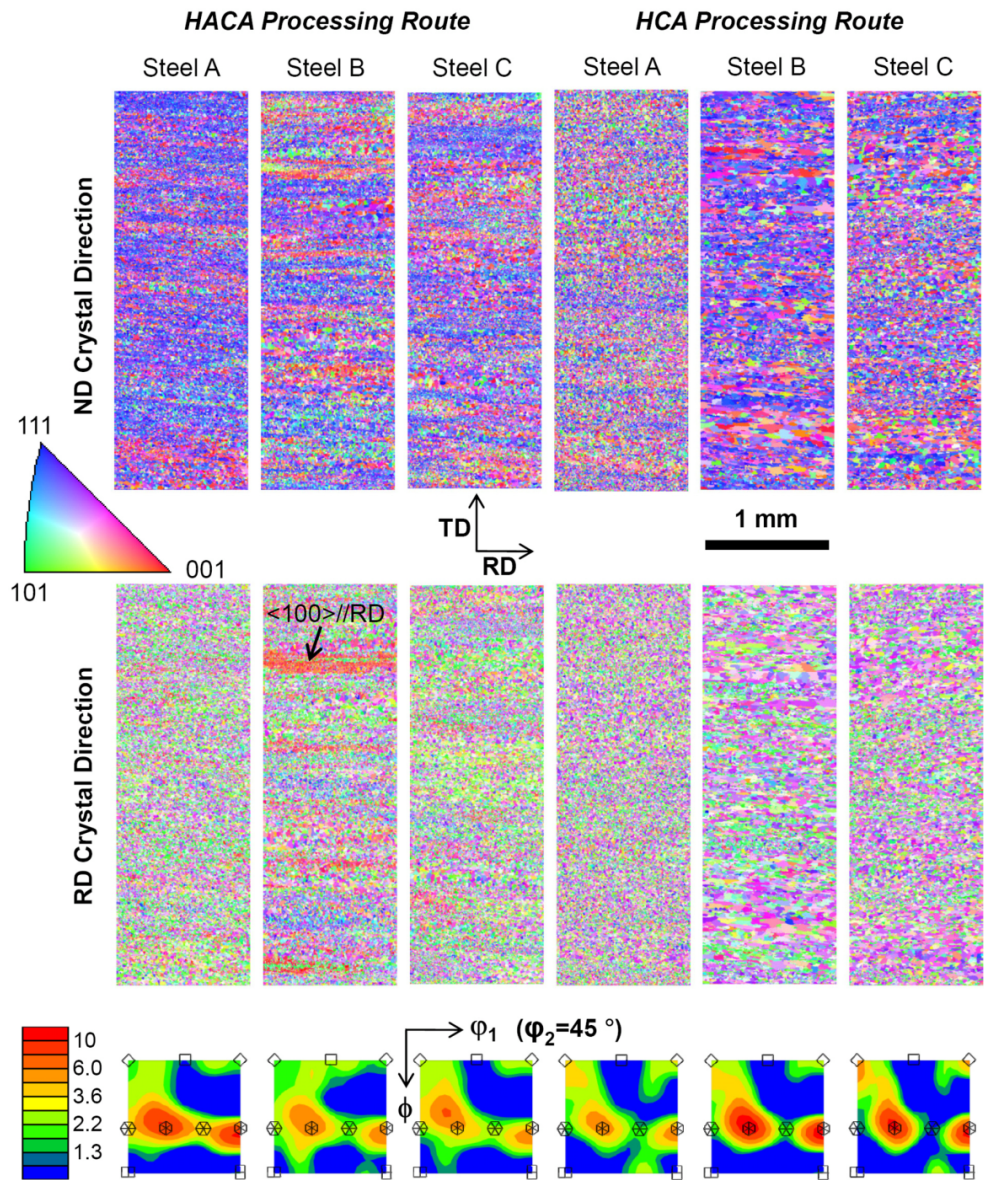


**Fig. 5.10.** EBSD crystal orientation maps of the midthickness ND plane of sheets. An area extending 3.3 mm in the TD and 1.1 mm in the RD was scanned.

Crystallographic directions parallel to the ND and RD as well as the corresponding ODFs are shown. For a description of symbols used in the ODF plots, refer to **Fig. 5.8**.

AlN formation leads to a low solute N content. As N is a strong  $\gamma$ -phase stabilizer, this will therefore raise the equilibrium  $\gamma$ -phase start temperature,  $A_{e1}$ , and facilitate the carbide formation as evidenced by extensive carbide formation in the hot rolled strip of steel C. The effect of N on the stability range of the  $\gamma$ -phase is clearly underestimated in the Thermo-Calc equilibrium calculations. To check whether or not  $\gamma$ -phase was present in equilibrium conditions at 1223 K (950 °C), the hot strips of the three steels were initially annealed at 1093 K (820 °C) for 5 hrs to obtain a homogenous ferritic matrix with embedded  $M_{23}C_6$  precipitates. AlN was also formed in the case of steel C. Dilatometry specimens of annealed hot strips were then held at 1223 K (950 °C) for 10 minutes and quenched to 293 K (20 °C). Whereas steels A and B were associated with a significant martensitic dilatation, no dilatation was observed in the steel C. The optical micrographs after the preceding procedure are shown in Fig. 5.11, which in accordance with the dilatation results, confirm the absence of  $\alpha'$  formation in the steel C but a significant  $\alpha'$  formation in the steels A and B. Therefore, the  $A_{e1}$  temperature of steel C must be above 1223 K (950 °C), *i.e.* much higher than the  $A_{e1}$  temperature of 1143 K (870 °C) predicted by Thermo-Calc (Fig. 5.2).

It is well established that the dissolution of interstitials in  $\gamma$ -phase is associated with a lattice dilatation, which can be observed by means of the lattice parameter measurements [11-12]. Variation with temperature of the  $\gamma$ -phase lattice parameter is shown in Fig. 5.12 for specimens heated at a rate of 0.5 K/s. Clearly, the lattice parameter of the  $\gamma$ -phase in the steel C increases at a higher rate in comparison with the other steels. Therefore, in addition to the thermal dilatation of the lattice, there is another significant contribution to the measured lattice parameter of the steel C. The additional expansion is due to the diffusion of more C and N atoms into the  $\gamma$ -phase as a result of the gradual dissolution of carbides and nitrides. Accordingly, in contrast to the steel A and steel B which show small variations in the  $M_s$  temperature after annealing for 2 minutes at temperatures above 1173 K (900 °C), the  $M_s$  temperature of steel C constantly decreases in the range of 1173-1323 K (900-1050 °C) as the C and N contents of the  $\gamma$ -phase increases (Fig. 5.13). The  $M_s$  temperatures in Fig. 5.13 have been calculated using the method proposed by Koistinen and Marburger [13].



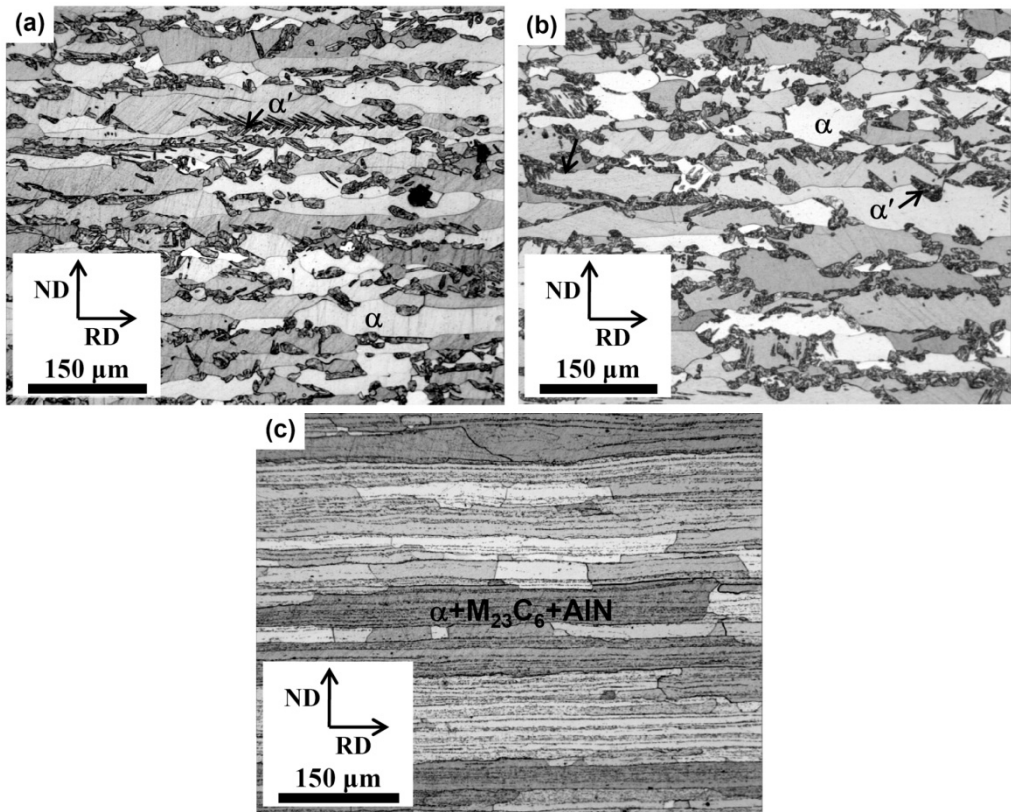


**Fig. 5.11.** Optical micrographs of the hot rolled strips after 5 hrs of annealing at 1093 K (820 °C) ( $<A_{e1}$ ) to obtain a homogenous ferritic microstructure containing precipitates, followed by holding at 1223 K (950 °C) for 10 minutes and quenching to room temperature. The dark martensite is seen in the steels A and B only. (Chemical etching)

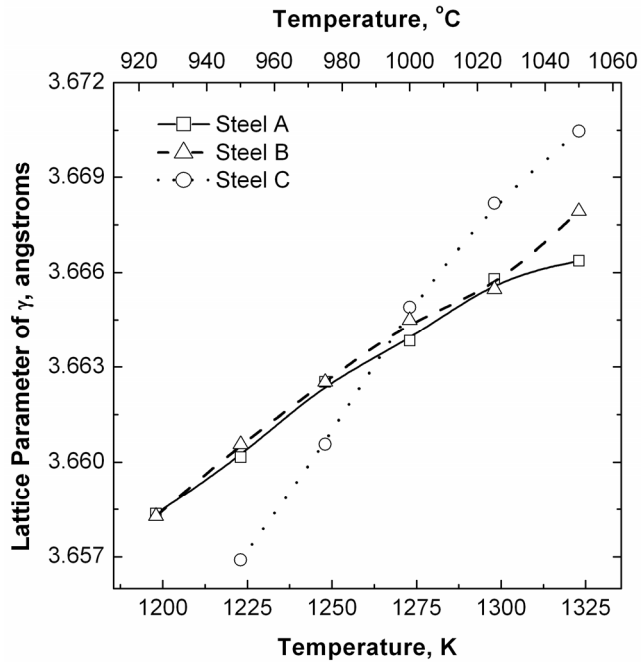


**Fig. 5.12.** Lattice parameter of the  $\gamma$ -phase based on the  $(111)_{\gamma}$  reflection, measured by high temperature XRD.

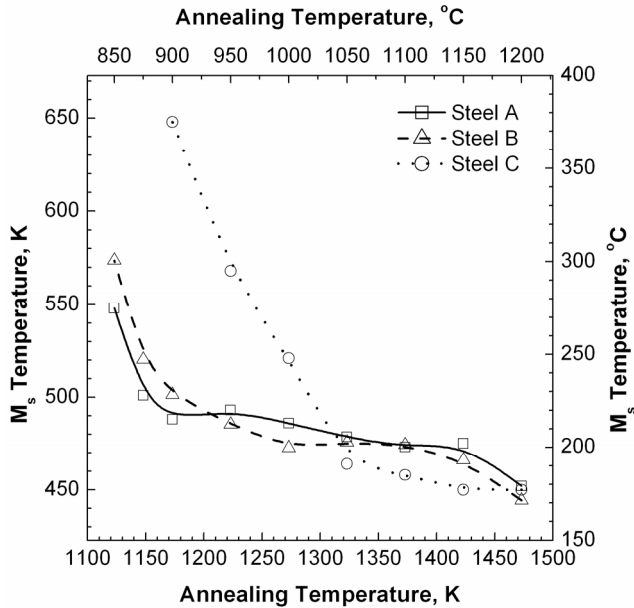


**Fig. 5.13.**  $M_s$  temperatures of the intercritical  $\gamma$ -phase based on the fitting of the martensite transformation kinetics data to the Koistinen-Marburger equation.



To study the  $\gamma$ -phase fraction evolution of steels in more detail, the instantaneous Coefficient of Thermal Expansion (CTE), *i.e.* derivative of the relative length change versus temperature, during continuous heating of dilatometry specimens at a rate of 10 K/s was plotted in Fig. 5.14(a). In the absence of any phase transformations, the instantaneous CTE simply reflects the weighted average CTE of the microstructural constituents. When a phase transformation is also involved, depending on the density difference between the parent and product phases and the fraction transformed, the instantaneous CTE will be influenced. The observed decrease in the instantaneous CTE of the investigated steels at about 1123 K (850 °C) (marked  $A_{c1}$ , the  $\gamma$ -phase start temperature on heating) is due to the replacement of the  $\gamma$ -phase transformation products, notably  $\alpha$ -phase, by the more closely packed  $\gamma$ -phase. In contrast to steels A and B which exhibit only a single abrupt decrease in the instantaneous CTE at about 1123 K (850 °C), steel C shows a less significant decrease at about 1123 K (850 °C) which is followed by a second small decrease in the temperature range of 1223-1273 K (950-1000 °C). The discontinuity, which is the consequence of a second gradual increase in the austenite fraction, is likely related to the dissolution of carbides beginning in the indicated temperature range. SEM micrographs, after holding for 2 minutes of dilatometry specimens of steel C at 1223 K (950 °C) and 1323 K (1050 °C), corresponding to below and above the austenitization discontinuity, are shown in Fig. 5.15(a,b). The volume fraction of carbides, predominantly along the boundaries, is significantly smaller at 1323 K (1050 °C) than at 1223 K (950 °C). This confirms that the dissolution of boundary carbides is the primary cause of the discontinuity during austenitization of steel C. Therefore, the discontinuous austenitization behavior must disappear if specimens are initially treated at a temperature above the carbides dissolution temperature and reappear by making the carbides form again. This was investigated by performing the heat treatment cycle shown in Fig. 5.14(b) on dilatometry specimens of steel C and plotting the instantaneous CTE during heating steps marked 1st, 2nd, and 3rd. As shown in Fig. 5.14(c), the discontinuity observed during the 1st heating step disappears in the 2nd heating step. This is because the boundary carbides responsible for the discontinuous austenitization behavior dissolve

during holding at 1473 K (1200 °C). The specimen taken to 1473 K (1200 °C) in the 2nd heating step was directly quenched to 1073 K (800 °C) and soaked for times of 10 and 30 minutes. This treatment causes carbides to form as the unstable  $\gamma$ -phase transforms to ferrite and carbides.

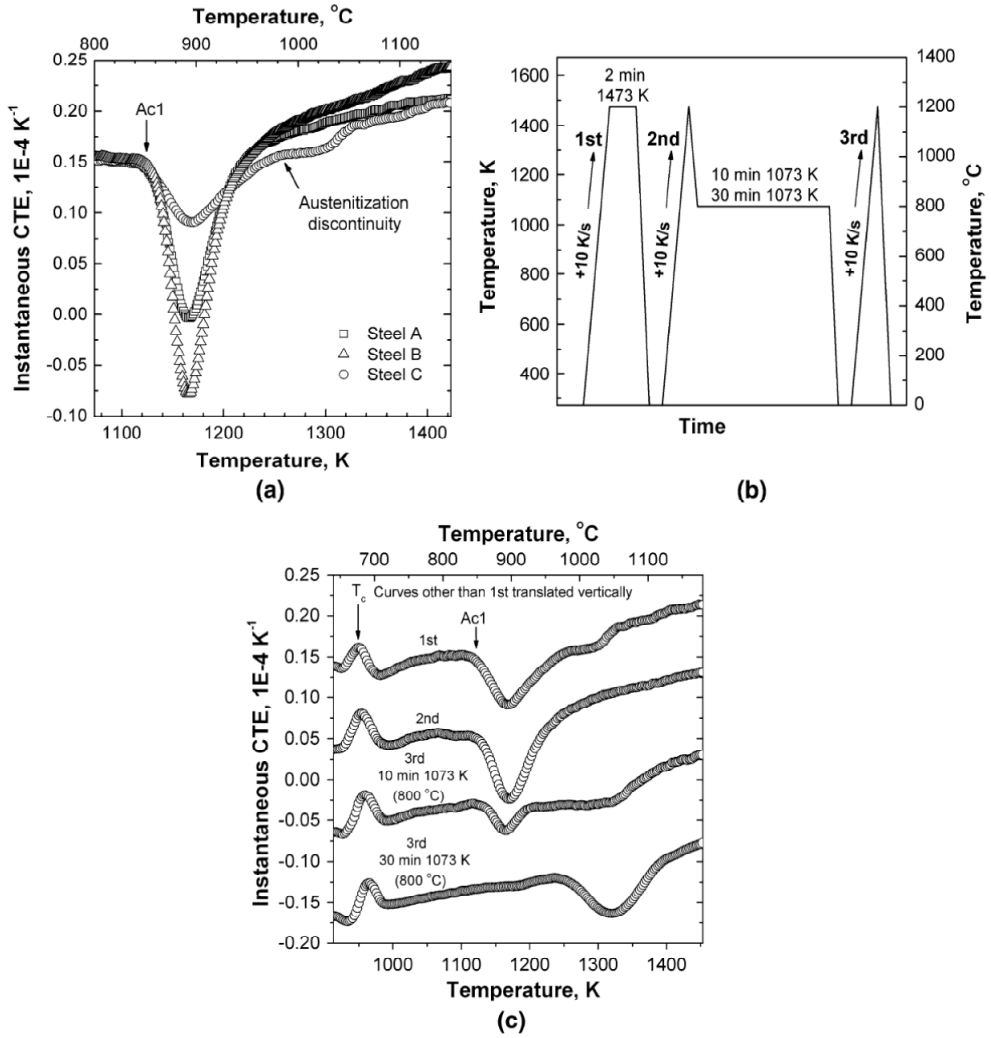


**Fig. 5.14.** (a) Instantaneous CTE during continuous heating of dilatometry specimens at a heating rate of 10 K/s. (b) Dilatometry-simulated heat treatment cycle used to study the dissolution/precipitation of carbides in steel C. Shown in (c) are the instantaneous CTE curves corresponding to heating steps 1<sup>st</sup>, 2<sup>nd</sup>, and 3<sup>rd</sup> in (b). For clarity, curves other than 1<sup>st</sup> have been translated downwards in increments of 0.1.

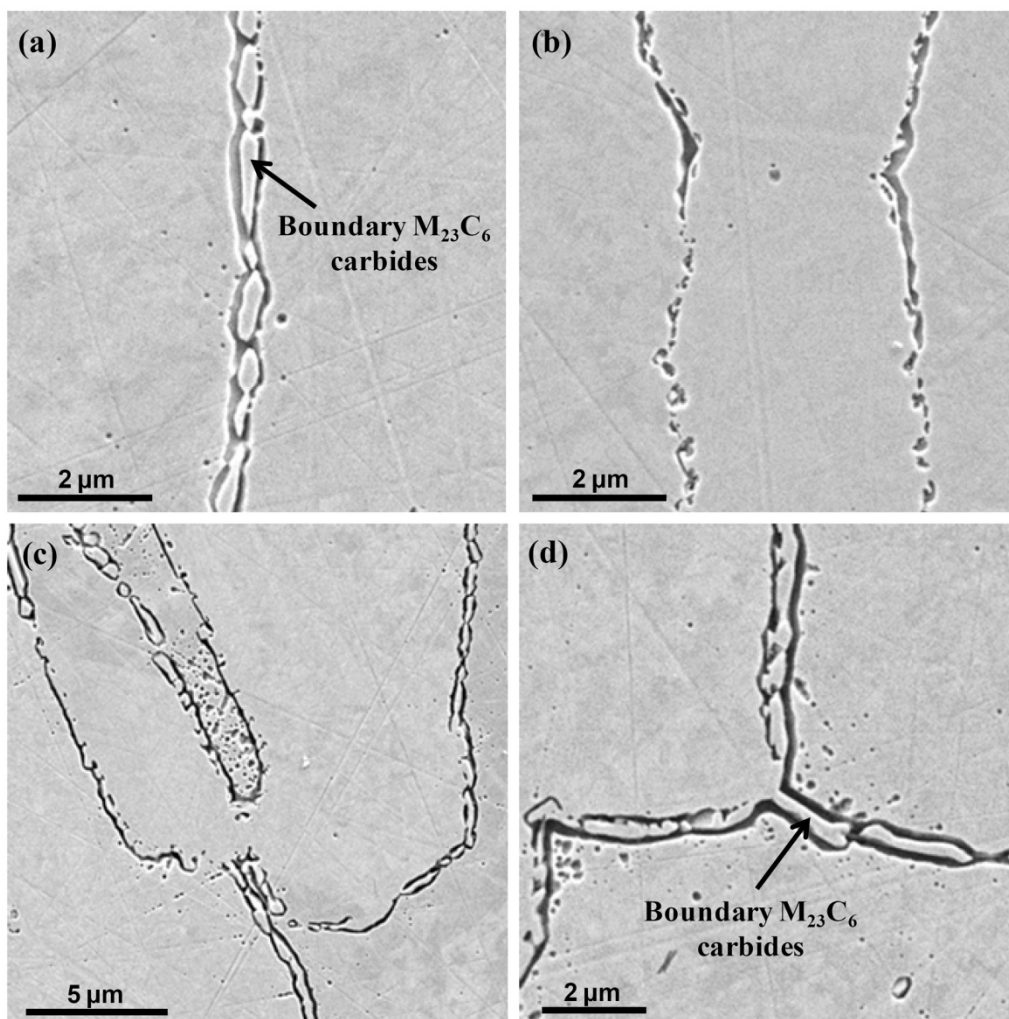


**Fig. 5.15.** SEM micrographs of steel C dilatometry specimens after 2 minutes of holding at 1223 K (950 °C) **(a)** and 1273 K (1000 °C) **(b)** followed by quenching to room temperature. **(c)** and **(d)** show the microstructure of dilatometry specimens of steel C after taking to 1473 K (1200 °C), quenching to 1073 K (800 °C) and holding for 10 minutes, followed by quenching to room temperature. (Electro-chemical etching)

Fig. 5.15(c) shows the microstructure of the specimen soaked for 10 minutes at 1073 K (800 °C) prior to the 3rd heating step. Stringers of carbides have again formed in the microstructure along certain boundaries. In the case of austenitic stainless steels

containing  $\delta$ -ferrite phase, precipitation of carbides has been reported to be fastest along the  $\delta/\gamma$  boundaries [14]. In fully austenitic stainless steels, the grain boundaries are the most favorable sites for the formation of carbides [5]. Therefore, the boundaries containing carbides in Fig. 5.15(c) are likely the  $\alpha/\gamma$  phase boundaries and the grain boundaries. Instantaneous CTE during the 3rd step heating of specimens treated at 1073 K (800 °C) for 10 and 30 minutes can be seen in Fig. 5.14(c). After an annealing time of 10 minutes, the austenitization during the 3rd heating step takes place discontinuously. When the holding time is increased to 30 minutes, however, the austenitization is observed to take place in a continuous manner but at a temperature much higher than 1123 K (850 °C). In the former case, the  $\gamma$ -phase taken to 1073 K (800 °C) does not fully decompose to ferrite and carbides at the end of the 10 minute cycle as evidenced by martensitic transformation related dilatation during cooling to room temperature. Therefore, the reversion to the  $\gamma$ -phase, of the C-enriched martensitic regions takes place at a temperature close to 1123 K (850 °C) during the 3rd heating step. This is in spite of the fact that the formation of very fine carbides within the  $\alpha'$  martensite substructure is a very fast process [15] and will likely precede the  $\gamma$ -phase reversion during the 3rd heating step. The justification for this would be the Gibbs-Thomson effect which tends to increase the Gibbs free energy and therefore the solubility limit of fine precipitates [16]. Therefore, the solubility limit of the very fine carbides nucleating in the martensite would be higher than the solubility limit of the coarse carbides present in the boundaries. When the soaking time at 1073 K (800 °C) is increased to 30 minutes, the  $\gamma$ -phase fully decomposes to ferrite and carbides and no martensitic transformation related dilatation is measured on cooling to room temperature. As a consequence of the absence of C-enriched martensitic regions in this case, the first austenitization step occurring at about 1123 K (850 °C) is eliminated and the  $\gamma$ -phase reversion takes place at a higher temperature of about 1243 K (970 °C), as the coarse boundary carbides start to dissolve. These findings are in agreement with the observation of no  $\gamma$ -phase formation after soaking at 1223 K (950 °C) of steel C with a microstructure composed of  $\alpha$ , AlN, and coarse carbides (Fig. 5.11(c)).

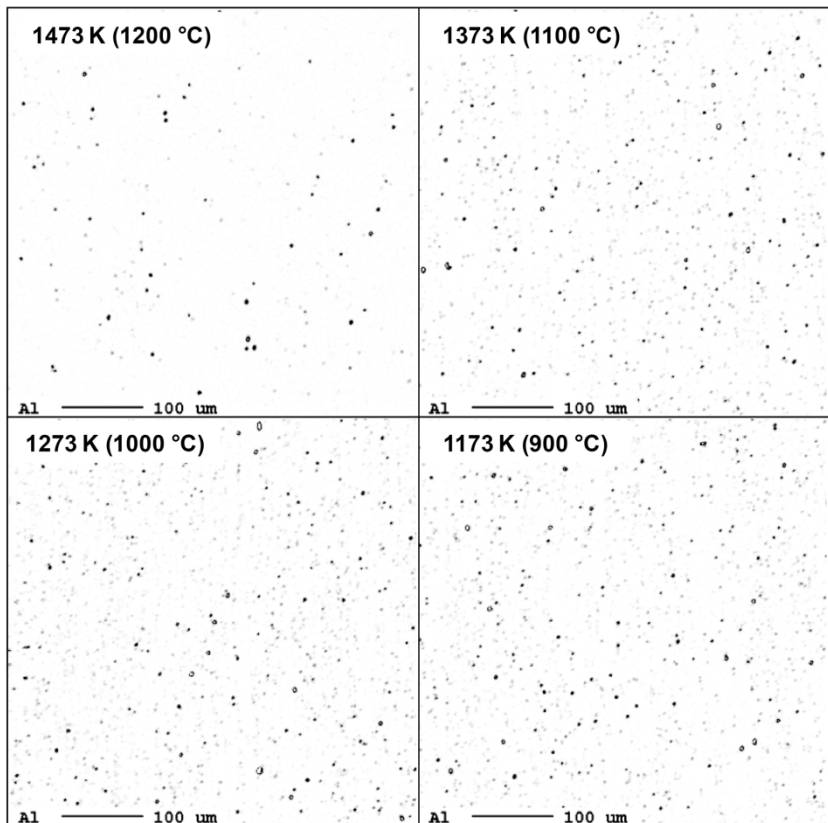


**Fig. 5.16.** EPMA elemental maps of Al showing the distribution of AlN precipitates after 1 minute of holding at the indicated temperatures.

Gradual dissolution of AlN is yet another contribution to the relatively flat  $\gamma$ -phase fraction profile of steel C which tends to become dominant at temperatures higher than the austenitization discontinuity due to the carbides dissolution. According to the EPMA elemental maps of Al shown in Fig. 5.16, there is a significant drop in the AlN fraction of steel C as the annealing temperature increases from 1373 K (1100 °C) to 1473 K (1200 °C). Below 1373 K (1100 °C), however, the change in the volume fraction of AlN precipitates is not very noticeable, indicating that carbides dissolution must be the main reason for the previous observations concerning the higher rate of  $\gamma$ -phase lattice expansion in steel C, based on the hot stage XRD results of Fig. 5.12. Similarly, the large drop in the  $M_s$  temperature of steel C dilatometry specimens in the intercritical annealing temperature range of 1173-1323 K (900-1050 °C) (Fig. 5.13) must be dominated by the dissolution of  $M_{23}C_6$  carbides rather than the AlN nitrides.

#### 5.4.2. Texture Bands Observation

The as-cast columnar grains, present in the outer sections of slabs, are known to be more susceptible to ridging than the central equiaxed grains [17-18]. Nevertheless, the texture bands responsible for ridging are more likely to be present in the midthickness plane of rolled sheets [18-22], where plane strain deformation is dominant during hot rolling. The reason might be the dominance of shear deformation in the subsurface sections during hot rolling, which generates a higher dislocation density and thus a higher driving force for the dynamic recrystallization [23].

In the present work, there was no clear correlation between the ridging height results of Fig. 5.5 and the midthickness plane micro-texture results of Fig. 5.10. Texture banding was observed for the three steels in all conditions. The type and the geometrical arrangement of the bands however was found to vary from one sample to another. Considering steels B and C processed according to the HACA route, which are associated with the best and the worst ridging resistance for this processing route, respectively, texture banding is more noticeable in the case of steel B. However, the bands in the HACA processed steel B have more crystallographic diversity compared to the bands in steel C. For instance, the clear bands of  $\langle 100 \rangle // \text{RD}$  oriented grains, shown in red in the RD crystal direction map of the midthickness plane of steel B, are entirely absent in steel C.

Midthickness plane EBSD scans can be of use for the qualitative assessment of the ridging resistance when the difference in the ridging resistance of different conditions is high. However, through-thickness texture inhomogeneities usually exist in the rolled products which tend to reduce the accuracy of the models making use of the midthickness plane grain orientation information only. Therefore, the most promising approach for the estimation of ridging resistance from the EBSD orientation maps would be to perform three dimensional scans, followed by the implementation of the grain orientation data into a crystal plasticity model.

### 5.4.3. Effect of the Processing Route on the Ridging Resistance

Profilometry results of Fig. 5.5 indicate the superior ridging resistance of steels associated with the HCA route compared to their HACA counterparts. This suggests the beneficial effect, during cold rolling, of the presence of  $\gamma$ -phase transformation products on the breakdown of undesirable grain colonies responsible for ridging. The grain colonies are more likely to be in the untransformed  $\alpha$ -phase where the dynamic recrystallization during hot rolling is very limited and recovery is the principal restoration mechanism [24]. The presence of bands of relatively hard  $\gamma$ -phase transformation products during cold rolling acts as a means of breaking up the unfavorably oriented grain colonies and results in an effective texture randomization after recrystallization. This is clearly evidenced by a higher fraction of  $\alpha$ -fiber oriented grains and a weaker  $\gamma$ -fiber texture in the strip obtained by the HCA route. Ridging in ferritic stainless steels is known to occur when low r-value texture bands with orientations other than the  $\gamma$ -fiber are embedded in a high r-value matrix with texture components belonging to the  $\gamma$ -fiber [25]. Therefore, a lower fraction of  $\gamma$ -fiber grains in the matrix decreases the r-value difference between the bands and the matrix. This can be an additional contribution to the higher ridging resistance of strips processed by the HCA route compared to the HACA route.

### 5.4.4. Effect of the Composition on the Ridging Resistance

When AISI 430 stainless steel is hot rolled in the  $\alpha+\gamma$  dual-phase stability range, the  $\gamma$ -phase, which has a higher strength than the  $\alpha$ -phase [26-27], accommodates less strain than the externally applied strain. The  $\alpha$ -phase, on the other hand, undergoes more strain than when a fully ferritic microstructure, *e.g.* a non-transformable ferritic stainless steel grade, is deformed. The higher strains and strain rates in the ferrite can promote the dynamic recrystallization and the breakdown of the grain colonies in the  $\alpha$ -phase. Furthermore, the transformed regions of the microstructure are less likely to contribute to ridging because the phase transformation acts as an effective means of texture randomization. These two are the main mechanisms leading to the superior

ridging resistance of the transformable grades of ferritic stainless steel compared to the non-transformable types [25, 28].

The steels used in the present study were all hot rolled in a  $\alpha+\gamma$  dual-phase region where the  $\gamma$ -phase fraction and its evolution play an important role. The relative ridging resistance of different compositions is maintained in both processing routes with the compositions B and C showing the smoothest and the roughest surfaces after straining, respectively. There is a direct relationship between the high temperature  $\gamma$ -phase fraction and the ridging resistance of the steels A and B. Steel B which has a higher  $\gamma$ -phase fraction than steel A, according to both equilibrium calculations and dilatometry, also shows a higher resistance to ridging. In contrast, steel C has roughness values considerably higher than the other two compositions in spite of its relatively high equilibrium  $\gamma$ -phase fractions. The temperature dependence of the  $\gamma$ -phase fraction of steel C, as determined by dilatometry (Fig. 5.4), indicates a large deviation from the thermodynamic equilibrium calculations shown in Fig. 5.2. The martensitic dilatation results show that the  $\gamma$ -phase fraction of steel C increases gradually up to a temperature of 1323 K (1050 °C), above which it remains constant. This specific temperature dependence of  $\gamma$ -phase fraction will result in the presence of a high fraction of hard  $\gamma$ -phase in the initial stage of hot rolling and a low  $\gamma$ -phase fraction during the final passes. As discussed above, a small  $\gamma$ -phase fraction during hot rolling is not desirable in view of the ridging resistance. Prior to hot rolling, however, slabs are usually reheated to temperatures of approximately 1473 K (1200 °C). The  $\gamma$ -phase fraction during hot rolling will therefore be estimated more realistically when the dilatometry samples are soaked at 1473 K (1200 °C) prior to being cooled to the annealing temperature. Initial soaking of the dilatometry samples at 1473 K (1200 °C) for 2 minutes resulted in a significant increase in the martensitic dilatation for steel C at temperatures below 1323 K (1050 °C), as shown by open circles in Fig. 5.4. This is mainly due to the dissolution, during the anneal at 1473 K (1200 °C), of carbides and nitrides present in the starting microstructure. The increased solute nitrogen and carbon content of the  $\gamma$ -phase as a result of initial soaking at 1473 K (1200 °C) adds to its stability and prevents its decomposition



during the hot rolling passes below 1323 K (1050 °C). The low ridging resistance of the steel C can therefore not be ascribed to the small  $\gamma$ -phase fraction during the final hot rolling passes.

As shown in the dilatometry results, one of the differences between steel C and the other steels is that it has a high fraction of  $\gamma$ -phase at the slab reheating temperature of 1473 K (1200 °C). This results in the limited formation of additional  $\gamma$ -phase during the hot rolling and restricts the chances of nucleation of  $\gamma$ -phase in the untransformed  $\alpha$ -phase bands. In the case of steels A and B, on the other hand, the  $\gamma$ -phase fraction at 1473 K (1200 °C) is low and approximately 20% of the  $\gamma$ -phase is formed during the rolling. As a result, new  $\gamma$ -phase islands form in deformed  $\alpha$ -phase during the hot rolling. Multiple nucleation sites are available for newly formed  $\gamma$ -phase in the deformed  $\alpha$ -phase because the slab reheating temperature of 1473 K (1200 °C) ensures a homogenous  $\alpha+\gamma$  dual-phase microstructure. This results in a rather uniform distribution of  $\gamma$ -phase islands in the ferritic matrix of steels A and B. The nucleation of  $\gamma$ -phase in the untransformed  $\alpha$ -matrix is desirable in view of the ridging resistance. The slightly superior ridging behavior of steel B compared to steel A can also be attributed to its higher  $\gamma$ -phase fraction during the hot rolling.

Fig. 5.17 shows light optical micrographs of the steels after hot rolling of 200 mm thick slabs to a thickness of 30 mm followed by fast cooling. The high temperature  $\gamma$ -phase, which transforms to the  $\alpha'$  martensite observed at room temperature, has a dark contrast. Based on the micrographs, it is not possible to distinguish clearly between the  $\gamma$ -phase regions present at the slab reheating temperature and those formed later during the hot rolling. However, the fine dispersed  $\alpha'$  martensite islands, noticeable in the ferritic matrix of steels A and B only, are believed to have formed from the high temperature  $\gamma$ -phase nucleated during the hot rolling.

The difference discussed in the preceding paragraph can be readily observed after homogenization annealing, for 5 hrs, of the 3 mm-thick hot strips at 1093 K (820 °C). This leads to a microstructure consisting of carbides (and AlN in the case of the steel C) and a homogenous ferritic matrix. Carbides preferably form in the carbon rich regions, *i.e.* in the  $\gamma$ -phase transformation products. This is clearly shown in Fig. 5.18

which compares the light optical micrographs of the homogenized hot rolled microstructure of steels A, B, and C. Precipitate-free bands are observed in the case of the steel C only. Steels A and B have a rather uniform distribution of precipitates. The precipitate-free regions in the steel C correspond to the  $\alpha'$ -free bands of ferrite in Fig. 5.17. In the case of steels A and B, the homogenous distribution of fine  $\alpha'$  islands in the ferrite reduces the distance between the alternate  $\alpha'$  bands and leads to a more uniform distribution of favorable sites for the nucleation of carbides.

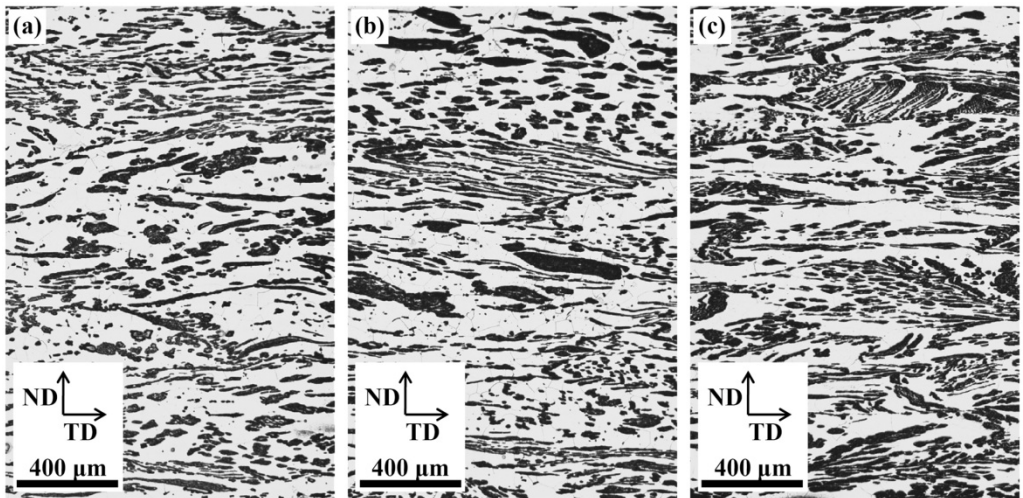


**Fig. 5.17.** Optical micrographs of steel A (a), steel B (b), and steel C (c) after hot rolling to a thickness of 30 mm. The  $\alpha'$  martensite has a dark contrast. (Electrochemical etching)

In 430-type steels, the  $\alpha \rightarrow \gamma$  transformation may compete with the recrystallization in the  $\alpha$ -phase during hot rolling. Hot rolling in the  $\alpha \rightarrow \gamma$  transformation range has therefore been connected with a more pronounced ridging [29]. The present work, however, suggests that the composition with the highest  $\gamma$ -phase fraction at the slab reheating temperature and the lowest  $\alpha \rightarrow \gamma$  transformation during hot rolling exhibits a more severe ridging. This implies that the beneficial effect of  $\gamma$ -phase formation in the untransformed  $\alpha$ -phase outweighs its detrimental effect due to retarding the dynamic recrystallization in the  $\alpha$ -phase.

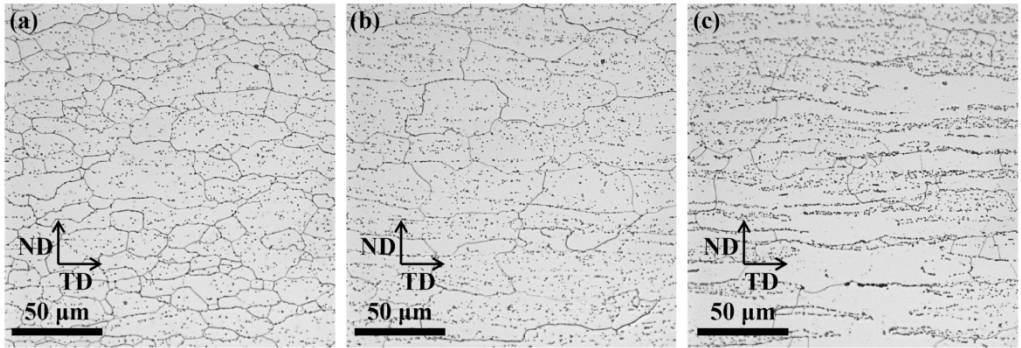


**Fig. 5.18.** Optical micrographs of steel A (a), steel B (b), and steel C (c) after hot rolling to a thickness of 3 mm and homogenization annealing for 5 hrs at 1093 K (820 °C). (Electro-chemical etching)

Hot deformation is known to accelerate the precipitation of carbides and nitrides in the microalloyed steels, by introducing dislocations which can act as favorable nucleation sites for their precipitation [10, 30]. If the precipitates are very fine, they can inhibit the dynamic recrystallization by the pinning action of the precipitates on the subgrain boundaries. Strain-induced formation of AlN could therefore be an additional detrimental mechanism leading to the low ridging resistance of steel C.

#### 5.4.5. Alloy Design for a Reduced Ridging

The microstructural evolution of two hypothetical steels denoted 1 and 2, with  $\gamma$ -phase fraction profiles shown in Fig. 5.19, is illustrated schematically in Fig. 5.20. Whereas steel 2 shows a clear sharp peak  $\gamma$ -phase fraction, steel 1 has a flat  $\gamma$ -phase fraction profile. The initial as-cast microstructure is assumed to be the same in both steels and consists of dark  $\alpha'$  martensite islands in a light ferritic matrix (Fig. 5.20(a)). The  $\gamma$ -phase fraction is however larger for the steel 1 at the slab reheating temperature (Fig. 5.20(b)) due to a higher solute interstitials that tend to broaden the  $\gamma$ -phase fraction profile and thereby maintain a high  $\gamma$ -phase fraction. Steel 2, however, does not develop a large  $\gamma$ -phase fraction (Fig. 5.20(e)) at the slab reheating temperature due to its lower interstitials content. In the early stage of hot rolling, the  $\gamma$ -phase fraction in the steel 2 increases significantly and new  $\gamma$ -phase islands nucleate in the untransformed ferritic matrix (Fig. 5.20(f)). In contrast, no new  $\gamma$ -phase islands

nucleate in the ferritic matrix of steel 1 (Fig. 5.20(c)), as the  $\gamma$ -phase fraction was already at its maximum value at the slab reheating temperature. As discussed in section 4.1, this is close to the situation where Al is present in the composition of high interstitial steels such as steel C in the present work. This fundamental difference between the two scenarios leads to a uniform distribution of  $\gamma$ -phase ( $\alpha'$  at room temperature) in the steel 2 at the end of hot rolling (Fig. 5.20(g)), while steel 1 contains relatively large regions of untransformed ferrite (Fig. 5.20(d)). After homogenization annealing of the microstructures shown in Fig. 5.20(d,g), steel 2 will exhibit a uniform distribution of precipitates whereas precipitate-free bands will be observed in the case of steel 1. This was demonstrated, with real microstructures, in Fig. 5.18.

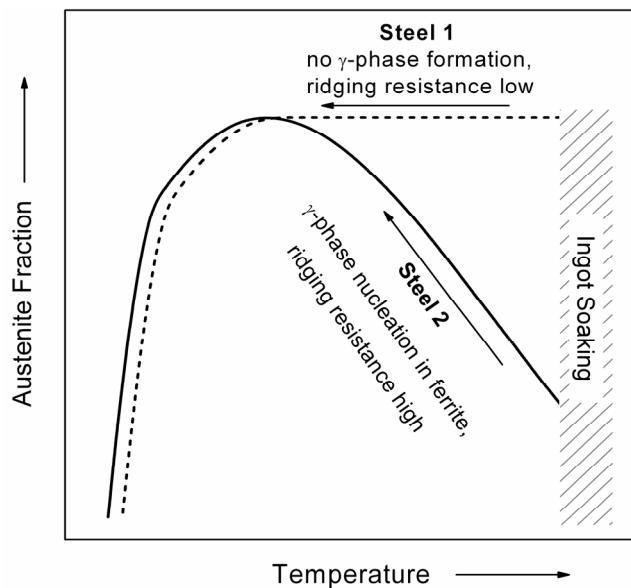


**Fig. 5.19.** Schematic representation of the alloy design concept introduced in the present work by means of two hypothetical AISI 430 ferritic stainless steels having different  $\gamma$ -phase fraction profiles.

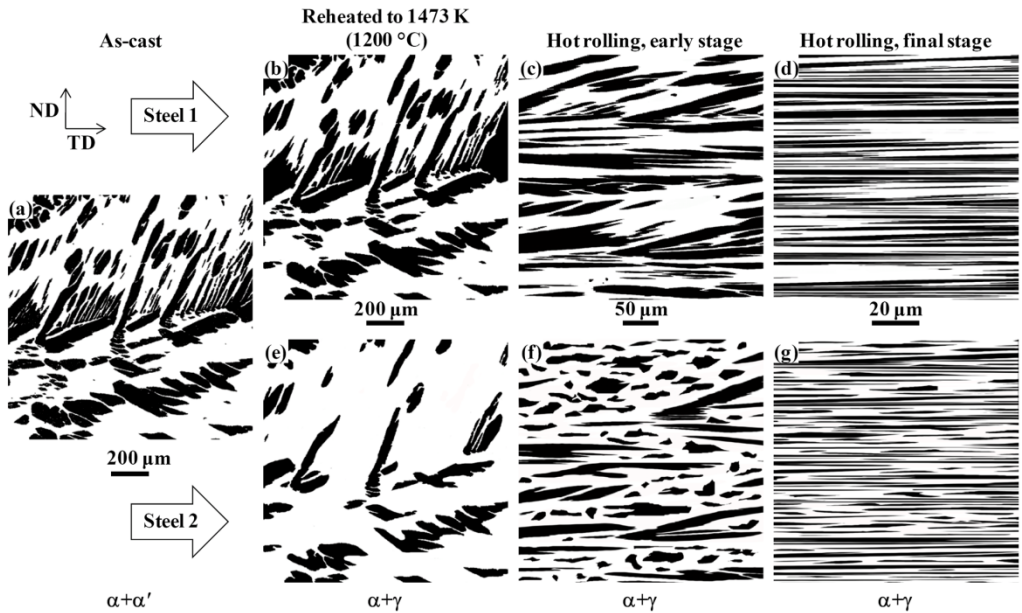


**Fig. 5.20.** Schematics showing microstructural evolution of the two hypothetical steels, denoted steel 1 and steel 2, with  $\gamma$ -phase fraction profiles shown in **Fig. 19**. The same initial as-cast microstructure **(a)** evolves differently for steels 1 and 2 after slab reheating at 1473 K (1200 °C) **(b,e)**, small hot rolling reductions **(c,f)**, and large hot rolling reductions **(d,g)**.

In order to obtain a good ridging resistance in the high interstitial steels containing Al, such as steel C in the present study, slab reheating temperatures must be high enough to ensure a low  $\gamma$ -phase fraction and full dissolution of AlN. This ensures nucleation of a large fraction of  $\gamma$ -phase in the untransformed  $\alpha$ -phase and a superior ridging resistance.

### 5.5. Correlation between the r-value and texture

As shown in Fig. 5.9, although associated with a small improvement in the ridging resistance, cold rolling of unannealed hot strips effectuated in the HCA processing route causes reversion of the angular dependence of r-value. This can be explained in view of the textural changes brought about by elimination of the homogenization annealing step, prior to the cold rolling, of hot rolled strip. As full RD section EBSD

ODFs of Fig. 5.8 show, the intensity of the  $\alpha$ -fiber texture components in the HCA processing route is higher than the HACA processing route. Fig. 5.21 shows the calculated r-value trends for several texture components of importance to ferritic steels. They are based on the relaxed constraint crystal plasticity model calculations [31-32]. Texture components belonging to the  $\alpha$ -fiber are generally associated with high r-values at 45 ° to RD. Exceptions to this are  $\{111\}\langle 110\rangle$  and orientations on the  $\alpha$ -fiber located below the  $\{111\}\langle 110\rangle$  component. Therefore, the reversed trend of r-value in the HCA route can be attributed to the high intensity of  $\alpha$ -fiber texture components between the  $\{111\}\langle 110\rangle$  and  $\{001\}\langle 110\rangle$  components. These components are likely a result of the persistence of  $\alpha$ -fiber texture components which dominate the as-cold rolled microstructure. The difference in the final texture of HCA and HACA route products could be related to the absence of martensite as well as low angle grain boundaries in the microstructure of homogenization annealed hot strips. These factors can affect the crystal rotations during cold rolling and the recrystallization behavior after cold rolling. Fine in-rolling-plane arrays of precipitates in the microstructure of unannealed hot strips can also influence the final texture by their boundary and dislocation pinning effect. This could be implied from the higher aspect ratio of grains in the HCA route sheets compared to the HACA route products. High angle grain boundary maps of Fig. 5.22 illustrate that the grains in HACA sheets are more equiaxed than the HCA sheets.

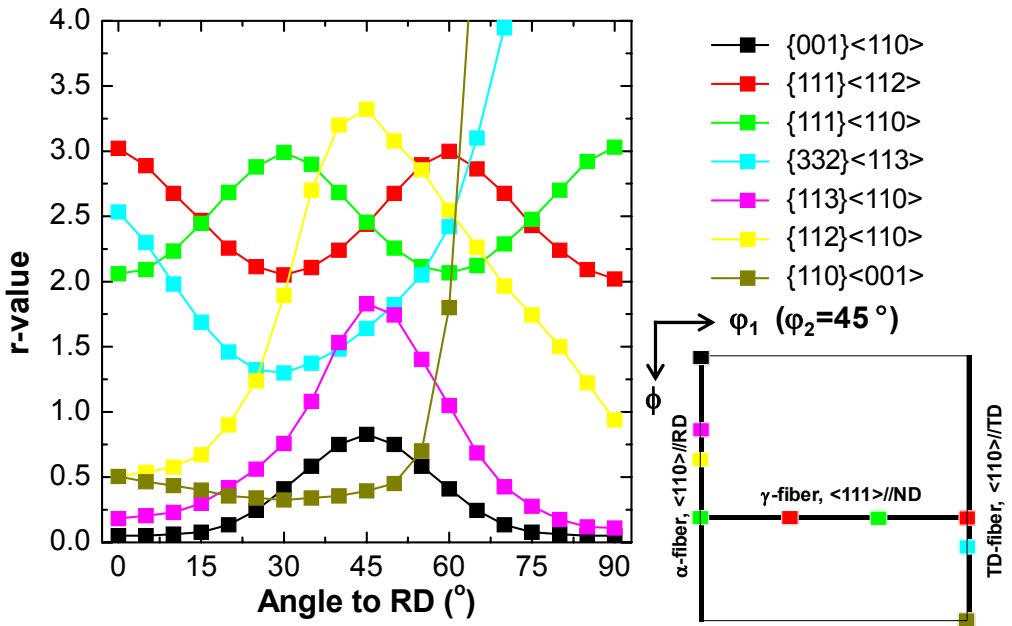


**Fig. 5.21.** Orientation dependence of the r-value for several texture components of importance to ferritic steels calculated based on the relaxed constraint model of crystal plasticity. Redrawn from [31-32].

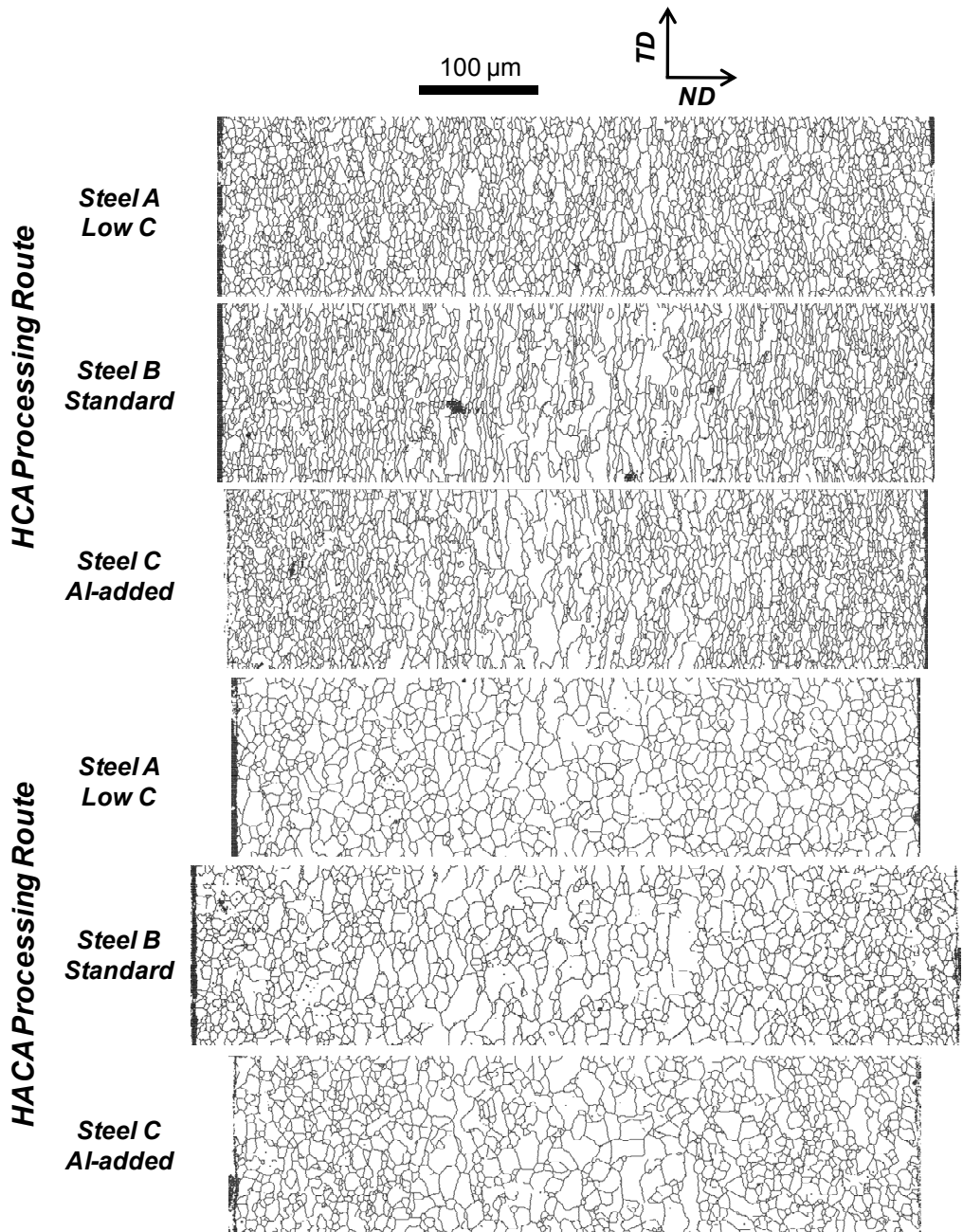


Fig. 5.22. EBSD maps of full RD plane of HCA and HACA processed sheets highlighting boundaries with misorientations larger than 15 °.



## 5.6. Conclusions

The effects of the thermo-mechanical processing and chemical composition on the ridging resistance of the AISI 430 transformable ferritic stainless steel were studied.

The main conclusions of the present work are as follows:

- 1- Cold rolling of as-hot rolled strip with a banded microstructure consisted of  $\alpha$ -phase and  $\gamma$ -phase transformation products ( $\alpha$ ,  $M_{23}C_6$ , and  $\alpha'$ ) results in an improved ridging resistance compared to when annealed hot rolled strip with a homogenous microstructure of  $\alpha+M_{23}C_6$  is cold rolled. The presence of hard  $\gamma$ -phase transformation products during cold rolling facilitates the breakdown of untransformed  $\alpha$ -phase grains elongated in the rolling direction and reduces the likelihood of formation of texture bands with similar orientations after recrystallization of untransformed  $\alpha$ -phase regions.
- 2- The presence, during hot rolling, of the  $\gamma$ -phase, which has a higher strength than the  $\alpha$ -phase at high temperatures, is beneficial to the ridging resistance. The higher strains and strain rates applied to the  $\alpha$ -phase, as a result of the presence of the  $\gamma$ -phase, will promote its dynamic recrystallization and improve the ridging resistance.
- 3- Not only the  $\gamma$ -phase fraction, but also its evolution during hot rolling, plays an essential role in the development of ridging. A small  $\gamma$ -phase fraction at the slab reheating temperature that increases considerably in the early stage of hot rolling is desirable. The  $\gamma$ -phase fraction profile for the steels with high interstitials is relatively broad. Therefore, the slab reheating temperature in such cases must be accordingly raised to ensure a small  $\gamma$ -phase fraction.
- 4- Al addition to the AISI 430 leads to the AlN formation and a higher stability of the  $M_{23}C_6$  carbides. This will significantly increase the  $A_{e1}$  temperature and decrease the  $\gamma$ -phase fraction. The flatter  $\gamma$ -phase fraction profile obtained in this case and the smaller  $\gamma$ -phase fraction will reduce the ridging resistance. In such cases, it is advisable to soak the slabs at temperatures corresponding to a low  $\gamma$ -phase fraction which is also high enough to achieve the full dissolution of  $M_{23}C_6$  and AlN.
- 5- Due to the through-thickness texture inhomogeneities, it is difficult to correlate the ridging resistance to the midthickness plane EBSD data only. The most promising

approach for the estimation of ridging resistance from the EBSD orientation maps would be to perform three dimensional scans, followed by the implementation of the grain orientation data into validated crystal plasticity models.

6- HACA processed sheets are associated with higher mean r-values than their HCA processed counterparts. The angular dependence of r-value also reverses by elimination of hot strip annealing step. These could be attributed to the higher intensity of  $\alpha$ -fiber texture components in the HCA route sheets.

### 5.7. References

- [1] D. Peckner and I. M. Bernstein, *Handbook of stainless steels*. New York: McGraw-Hill, 1977.
- [2] T. H. O. Lee, *et al.*, "Crystallographic details of precipitates in Fe-22Cr-21Ni-6Mo-(N) superaustenitic stainless steels aged at 900 °C," *Metallurgical and Materials Transactions A: Physical Metallurgy and Materials Science*, vol. 31, pp. 1713-1723, 2000.
- [3] T. F. Liu, *et al.*, "Orientation relationships among  $M_{23}C_6$ ,  $M_6C$ , and austenite in an Fe-Mn-Al-Mo-C alloy," *Metallurgical transactions. A, Physical metallurgy and materials science*, vol. 21 A, pp. 567-574, 1990.
- [4] K. H. Kuo and C. L. Jia, "Crystallography of  $M_{23}C_6$  and  $M_6C$  precipitated in a low alloy steel," *Acta Metallurgica*, vol. 33, pp. 991-996, 1985.
- [5] T. Sourmail, "Precipitation in creep resistant austenitic stainless steels," *Materials Science and Technology*, vol. 17, pp. 1-14, 2001.
- [6] A. F. Padilha and P. R. Rios, "Decomposition of austenite in austenitic stainless steels," *ISIJ International*, vol. 42, pp. 325-337, 2002.
- [7] M. H. Biglari, *et al.*, "Crystal structure and morphology of AlN precipitating on nitriding of an Fe-2at.% Al alloy," *Philosophical Magazine A*, vol. 72, pp. 1281 - 1299, 1995.

- [8] V. Massardier, *et al.*, "Kinetic and microstructural study of aluminium nitride precipitation in a low carbon aluminium-killed steel," *Materials Science and Engineering A*, vol. 355, pp. 299-310, 2003.
- [9] M. Sennour and C. Esnouf, "Contribution of advanced microscopy techniques to nano-precipitates characterization: Case of AlN precipitation in low-carbon steel," *Acta Materialia*, vol. 51, pp. 943-957, 2003.
- [10] F. G. Wilson and T. Gladman, "Aluminium nitride in steel," *International Materials Reviews*, vol. 33, pp. 221-286, 1988.
- [11] B. C. De Cooman, *et al.*, *Materials Design, The Key to Modern Steel Products*: GRIPS Media, Germany, 2007.
- [12] T. S. Hummelshøj, *et al.*, "Lattice expansion of carbon-stabilized expanded austenite," *Scripta Materialia*, vol. 63, pp. 761-763, 2010.
- [13] D. P. Koistinen and R. E. Marburger, "A general equation prescribing the extent of the austenite-martensite transformation in pure iron-carbon alloys and plain carbon steels," *Acta Metallurgica*, vol. 7, pp. 59-60, 1959.
- [14] S. H. Kim, *et al.*, "Dissolution kinetics of delta ferrite in AISI 304 stainless steel produced by strip casting process," *Materials Science and Engineering A*, vol. 356, pp. 390-398, 2003.
- [15] J. Mola, "Title," unpublished|.
- [16] D. A. Porter and K. E. Easterling, *Phase Transformations in Metals and Alloys*, 2nd ed. London: Chapman & Hall, 1992.
- [17] J. I. Hamada, *et al.*, "Effect of Initial Solidified Structure on Ridging Phenomenon and Texture in Type 430 Ferritic Stainless Steel Sheets," *ISIJ International*, vol. 43, pp. 1989-1998, 2003.
- [18] H. J. Shin, *et al.*, "The effect of texture on ridging of ferritic stainless steel," *Acta Materialia*, vol. 51, pp. 4693-4706, 2003.

- [19] O. Engler, *et al.*, "Crystal-plasticity analysis of ridging in ferritic stainless steel sheets," *Metallurgical and Materials Transactions A: Physical Metallurgy and Materials Science*, vol. 36, pp. 3127-3139, 2005.
- [20] H. G. Kang, *et al.*, "Effect of lubrication during hot rolling on the evolution of through-thickness textures in 18%Cr ferritic stainless steel sheet," *Steel Research International*, vol. 79, pp. 489-496, 2008.
- [21] M. Brochu, *et al.*, "Analysis of grain colonies in type 430 ferritic stainless steels by Electron Back Scattering Diffraction (EBSD)," *ISIJ International*, vol. 37, pp. 872-877, 1997.
- [22] S. H. Park, *et al.*, "Evolution of microstructure and texture associated with ridging in ferritic stainless steels," *ISIJ International*, vol. 42, pp. 100-105, 2002.
- [23] D. Raabe and K. Lücke, "Texture and microstructure of hot rolled steel," *Scripta Metallurgica et Materialia*, vol. 26, pp. 1221-1226, 1992.
- [24] J. S. Hinton and J. H. Beynon, "Restoration processes during hot deformation in the  $\delta$ -ferrite and austenite dual phase region of AISI430 ferritic stainless steel," *ISIJ International*, vol. 47, pp. 1465-1474, 2007.
- [25] I. Jung, *et al.*, "Influence of the Cold Rolling and Annealing Sequence on the Ridging Behaviour of Ti-Stabilized 18% Cr Ferritic Stainless Steel," *Steel Research International*, vol. 81, pp. 1089-1096, 2010.
- [26] T. Siegmund, *et al.*, "The irreversible deformation of a duplex stainless steel under thermal cycling," *Materials Science and Engineering A*, vol. 169, pp. 125-134, 1993.
- [27] H. J. McQueen, "Elevated-temperature deformation at forming rates of  $10^{-2}$  to  $10^2$  s<sup>-1</sup>," *Metallurgical and Materials Transactions A: Physical Metallurgy and Materials Science*, vol. 33, pp. 345-362, 2002.

- [28] J. Mola, *et al.*, "Influence of texture on ridging and formability of 16%Cr ferritic stainless steel," *Solid State Phenomena*, vol. 160, pp. 153-158, 2010.
- [29] K. Kimura, *et al.*, "Hot recrystallization behavior of SUS 430 stainless steel," *Nippon Steel Technical Report*, pp. 11-16, 1996.
- [30] T. Gladman, *The physical metallurgy of microalloyed steels*. London: Maney Publishing, 1997.
- [31] R. K. Ray, *et al.*, "Transformation textures in steels," *ISIJ International*, vol. 34, pp. 927-942, 1994.
- [32] R. K. Ray, *et al.*, "Cold rolling and annealing textures in low carbon and extra low carbon steels," *International Materials Reviews*, vol. 39, pp. 129-172, 1994.



## Chapter VI

# Cold Rolling of $\alpha+\alpha'$ Dual-Phase Microstructure

### 6.1. Introduction

In chapter 5, the direct cold rolling of unannealed hot strips was found to be associated with a superior ridging resistance compared to the case where hot strips were batch annealed prior to the cold rolling. The improved ridging resistance of sheets cold rolled in the presence of a small fraction of  $\alpha'$  implies that introducing larger fractions of fresh martensite can further improve the ridging resistance. Therefore, two different volume fractions of martensite were deliberately introduced in the microstructure of hot rolled strips through annealing at two different intercritical temperatures followed by quenching and the properties of interest namely ridging resistance and r-value were measured.

### 6.2. Experimental Procedure

A 3 mm-thick hot rolled strip of standard AISI 430 composition was used for the processing routes explained in this chapter. As shown in Fig. 6.1, it had a microstructure basically consisting of  $\alpha$  ferrite and  $\alpha'$  martensite with a small volume fraction of fine precipitates present in the  $\alpha/\alpha'$  boundaries. The hot strips were intercritically annealed at 865 °C and 1000 °C in order to obtain hot strips containing

known volume fractions of martensite for the subsequent cold rolling operations. Another hot strip intercritically annealed at 950 °C led to ridging and r-value results similar to the hot strip annealed at 1000 °C. This implies a similar  $\alpha'$  fraction and microstructural evolution upon annealing at 950 °C and 1000 °C. Fig. 6.2 shows the MultiPAS annealing simulator used for the intercritical annealing of hot strips. The annealing times at 1000 °C and 865 °C were 60 s and 150 s, respectively, leading to approximate  $\alpha'$  volume fractions of 35% and 15%. The heat treated hot strips were subsequently cold rolled to a thickness of 0.6 and batch annealing simulation at 820 °C followed. The processing steps in the routes denoted HA1000QCA and HA865QCA (H: hot rolling, A: annealing, Q: quenching, C: cold rolling) are schematically shown in Fig. 6.3.

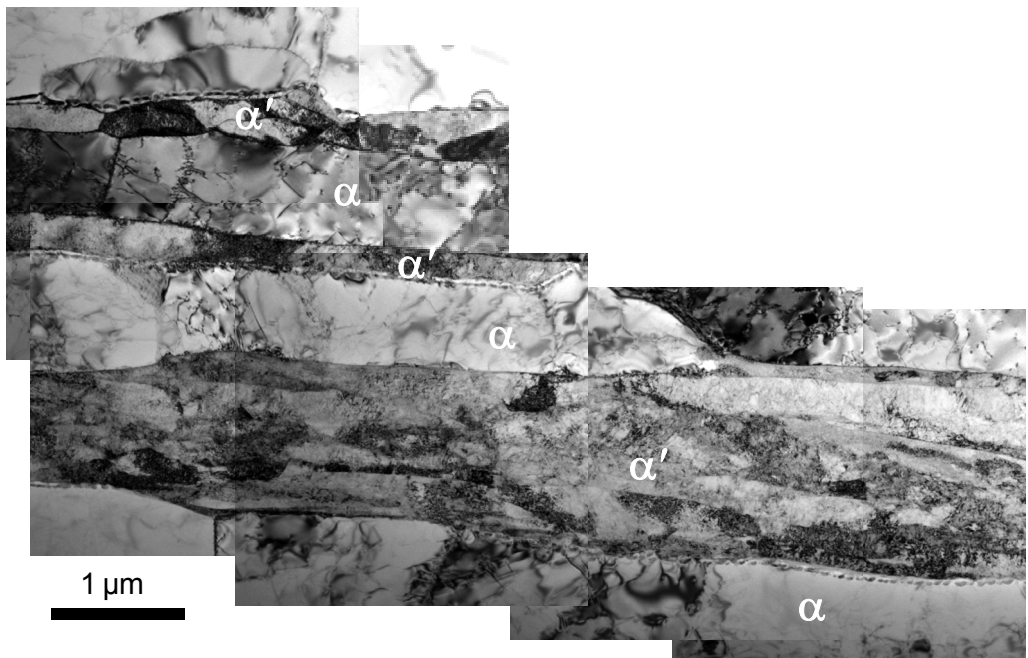


**Fig. 6.1.** TEM micrograph showing the microstructure of hot rolled strip used for the HAQCA route processing.

The final sheets were evaluated in terms of ridging resistance by measuring roughness along the TD of ASTM E8 standard specimens tensile strained 15% in the RD. The r-value was measured automatically by in-situ measurement of the width change in the



strain range of 10-15%. EBSD characterization of cold rolled sheets before and after cold rolling was also carried out.

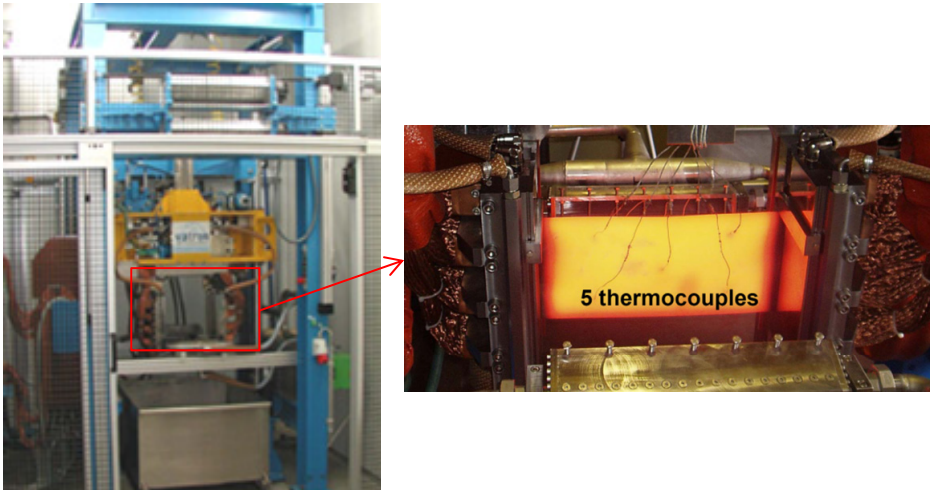


**Fig. 6.2.** The MultiPAS annealing simulator used for intercritical annealing of 3 mm-thick hot rolled strips.

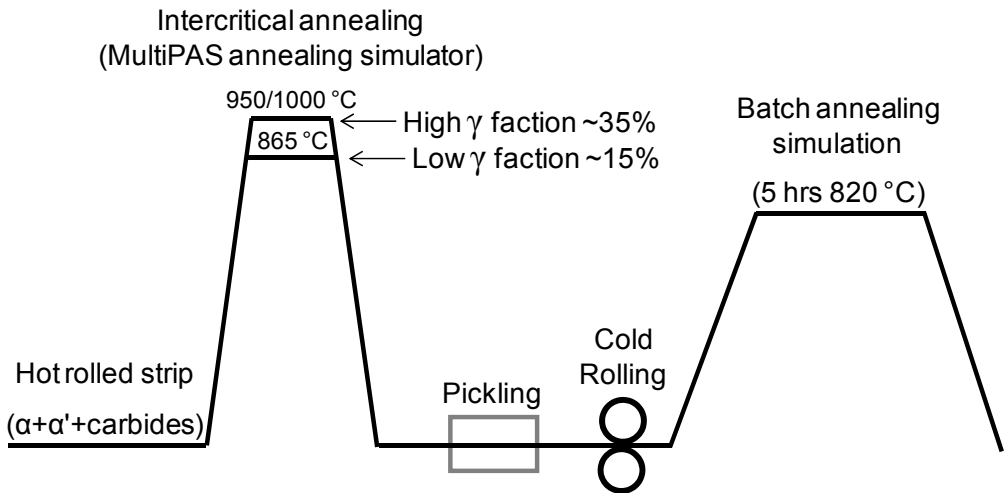


**Fig. 6.3.** The MultiPAS annealing simulator used for intercritical annealing of 3 mm-thick hot rolled strips.

### 6.3. Results and Discussion

The EBSD orientation maps of Fig. 6.4 show the microstructure after cold rolling of intercritically annealed hot strips. In the case of both intercritical annealing

temperatures, the density of  $\alpha$ -fiber oriented grains after cold rolling is high. In the case of annealing at 1000 °C, the martensite lath boundaries not parallel to the TD are clearly visible. In other words, during cold rolling, the large difference in the strength of ferrite and martensite has caused partitioning of more strain in the softer phase i.e. ferrite, leaving the martensitic morphology more or less unchanged. Whereas the hot strip annealed at 865 °C shows a cold rolled microstructure composed of discrete grains of elongated ferrite, the ferritic regions in the HA1000QC sheet are subdivided into narrow bands of small rotations with boundaries which cannot be delineated easily. Additionally, the ferritic grains in the HA1000QC sheet are not as elongated in the TD as the ferrite in the HA865QC sheet.

The differences in the microstructure of as-cold rolled sheets can be attributed to the microstructure of annealed hot strips. The well-delineated ferrite boundaries are likely due to the presence of low angle grain boundaries prior to cold rolling because the annealing time of 150 s at 865 °C is not sufficient to cause the full annihilation of the low angle grain boundaries present in the hot strip microstructure. Annealing at 1000 °C, however, ensures that large ferritic grains free of low angle grain boundaries are obtained. To illustrate this, the effect of annealing on the microstructure of the hot strip used in the HCA and HACA processing routes discussed in chapter 5 is shown in Fig. 6.5. Whereas the low angle grain boundaries persist in the hot strip microstructure after annealing at 850 °C and 875 °C, they anneal out after annealing at 1000 °C. One of the reasons for the persistence of low angle grain boundaries could be the stability of  $M_{23}C_6$  precipitates after the annealing treatment at 875 °C and their dissolution at 1000 °C.

### **6.3.1. Ridging Resistance**

The profilometry results for the standard hot strips intercritically annealed at 865 °C, 950 °C, and 1000 °C prior to cold rolling is shown in Fig. 6.6. The results are compared with the results of HCA and HACA processing routes (chapter 5) for the standard composition. Ridging height decreases with increasing the  $\alpha'$  fraction during cold rolling. As mentioned before, the intercritical annealing temperatures of 950 °C

and 1000 °C were associated with comparable ridging (and r-value) results. Some of the tensile specimens used for the ridging measurements were polished prior to 15% tensile straining. Polishing was found to cause a marginal improvement of the ridging resistance.

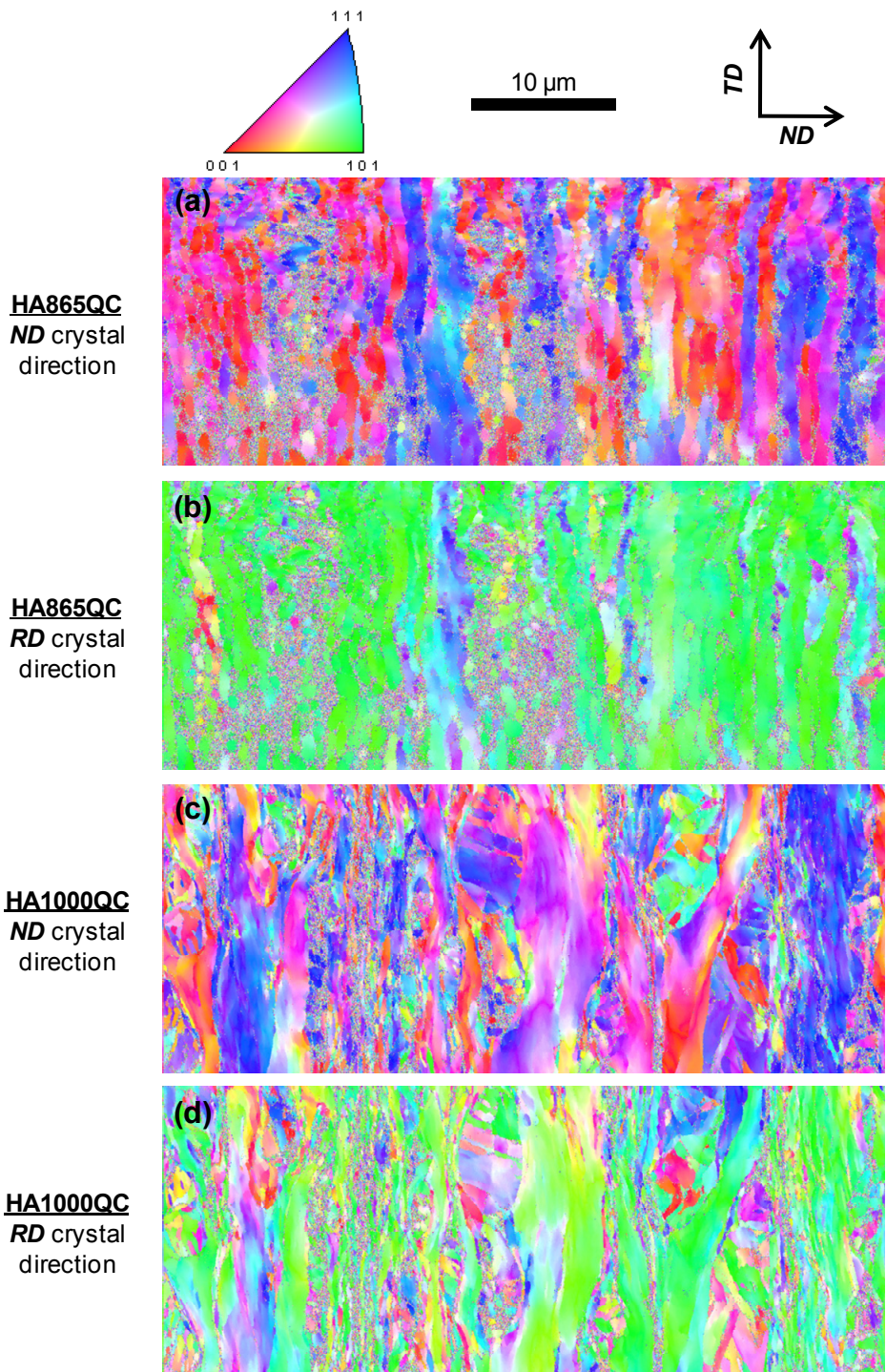


**Fig. 6.4.** EBSD orientation maps indicating crystal directions parallel to RD and ND of the cold rolled HA865QC and HA1000QC sheets.

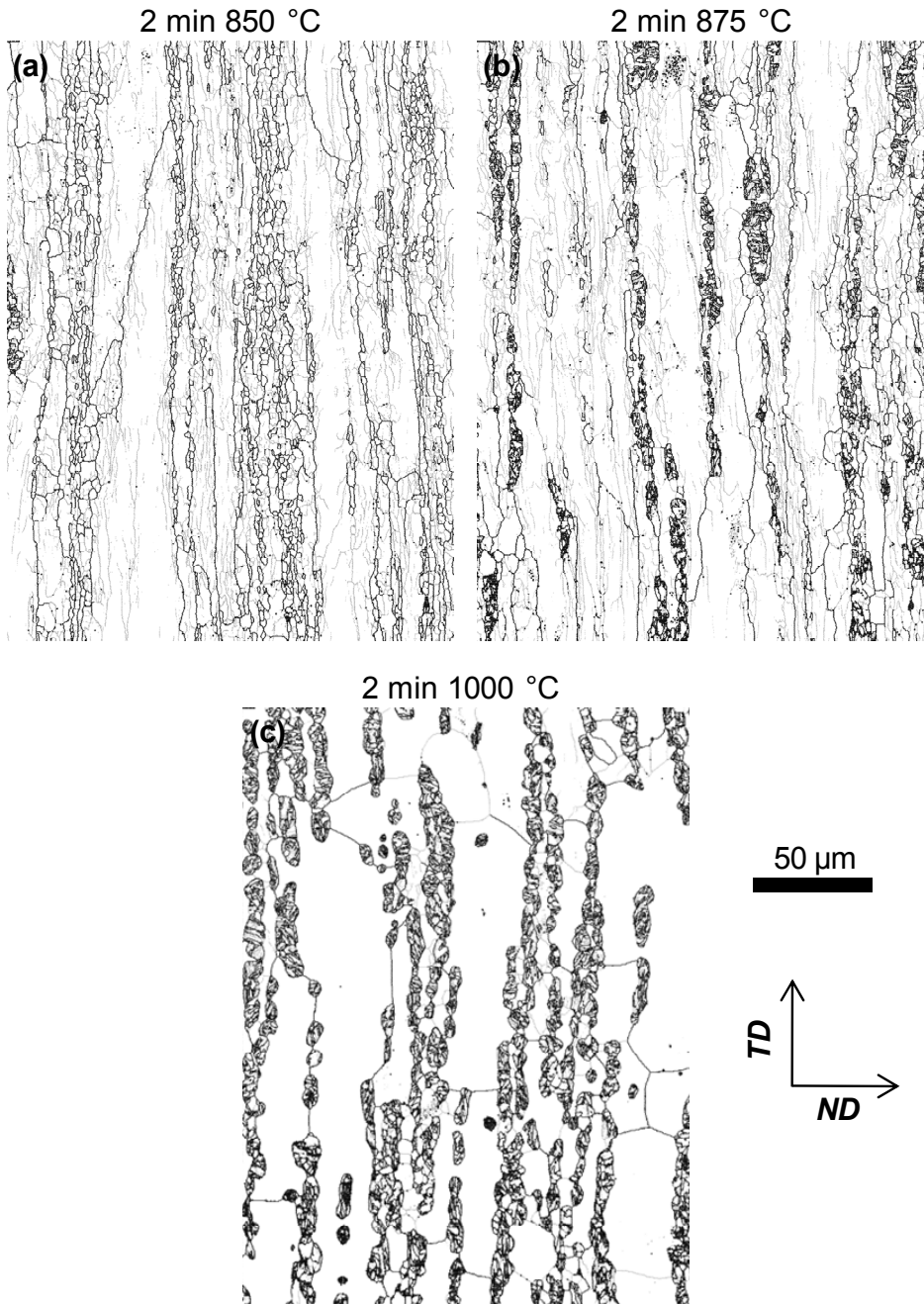


**Fig. 6.5.** EBSD maps of the hot strip used in the HCA and HACA processing routes after annealing for 2 minutes at 850 °C (a), 875 °C (b), and 1000 °C (c). The maps highlight boundaries with misorientation angles between 2 ° and 15 ° (gray) and boundaries with misorientation angles larger than 15 ° (black).

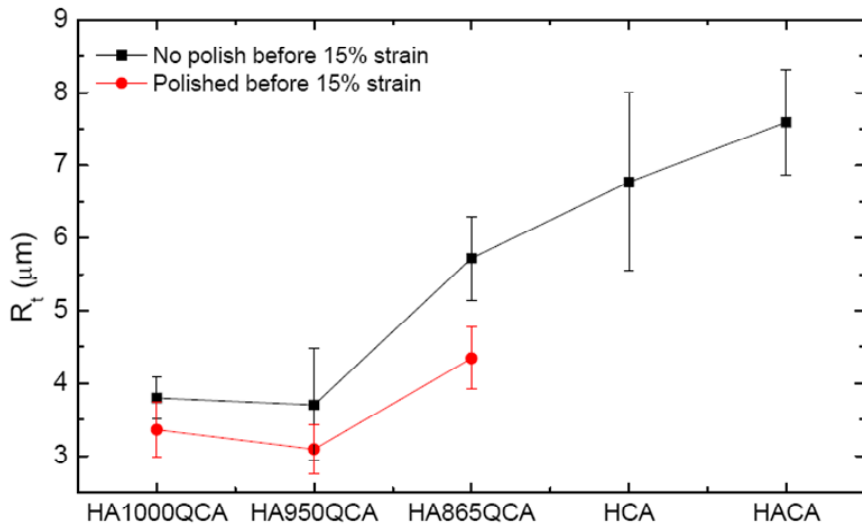


**Fig. 6.6.** Roughness parameter  $R_t$  for the AISI 430 sheets of standard composition processed according to HAQCA, HCA, and HACA processing routes. The red symbols are for tensile specimens polished prior to 15% straining.

The midthickness EBSD orientation maps of Fig. 6.7 confirm the absence of noticeable texture bands parallel to the RD of HAQCA route final sheets in agreement with their superior ridging resistance. This is particularly true for the HA1000QCA route sheet which is also associated with a very weak texture. Another characteristic of the HAQCA route sheets is their finer grain size than the HCA and HACA route sheets (compare with Fig. 5.10).

One of the mechanisms responsible for the high ridging resistance of HAQCA route products is the breakdown of the elongated ferrite grains as a result of presence of hard  $\alpha'$  phase during cold rolling. This effect will be more pronounced in the presence of higher  $\alpha'$  fractions. EBSD orientation maps of Fig. 6.8 taken from the TD section of as-cold rolled hot strips demonstrate a high density of shear bands in the microstructure of as-cold rolled hot strip containing about 35%  $\alpha'$ . These hot strips effectively cut through the elongated ferrite grains and fragment them. Besides, the shear bands can themselves act as favorable sites for the nucleation of recrystallized ferrite grains in the subsequent annealing step and bring about texture randomness and



a fine grain size. The microstructural evolution upon cold rolling and recrystallization of a dual phase  $\alpha+\alpha'$  microstructure will be further dealt with in chapters 7-8.

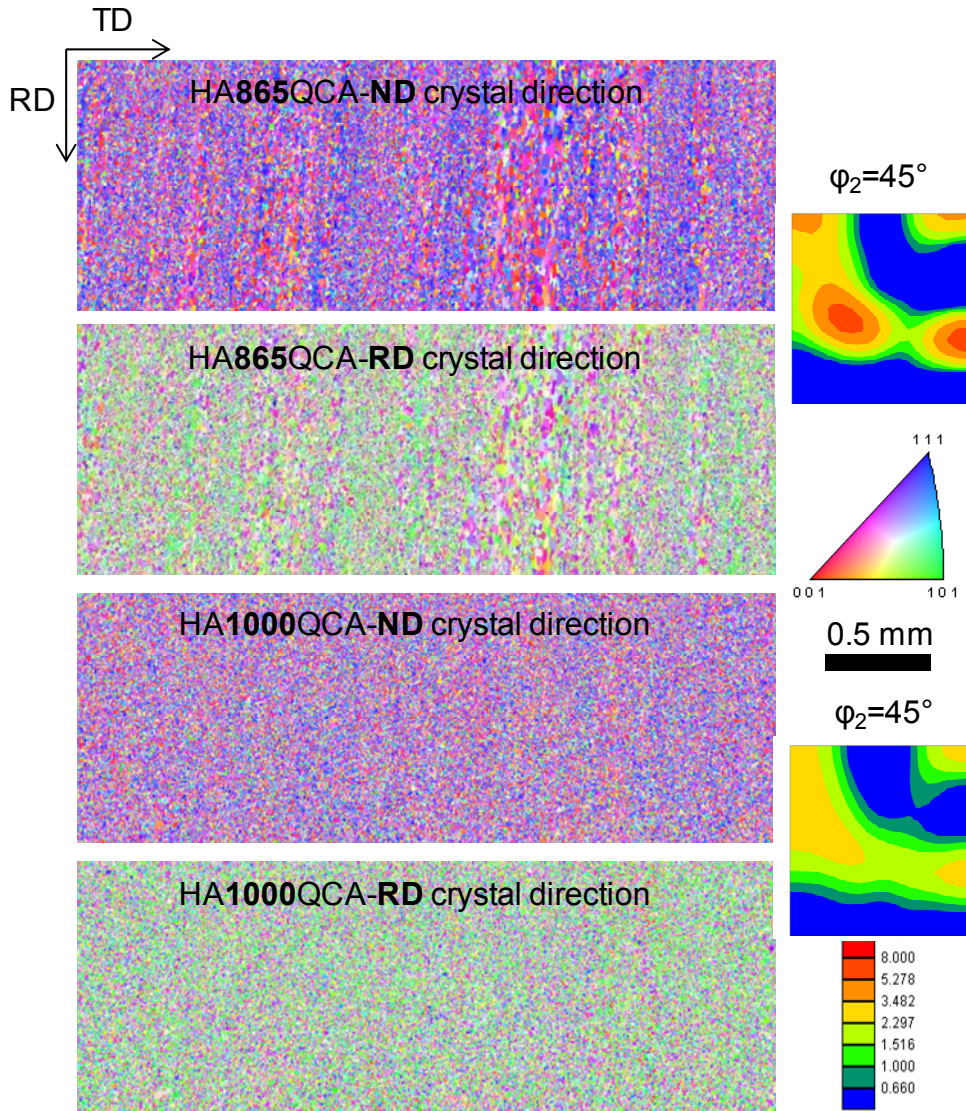


**Fig. 6.7.** EBSD crystal orientation maps of the midthickness ND plane of sheets. An area extending 3.3 mm in the TD and 1.1 mm in the RD was scanned. Crystallographic directions parallel to the ND and RD as well as the corresponding ODFs are shown.

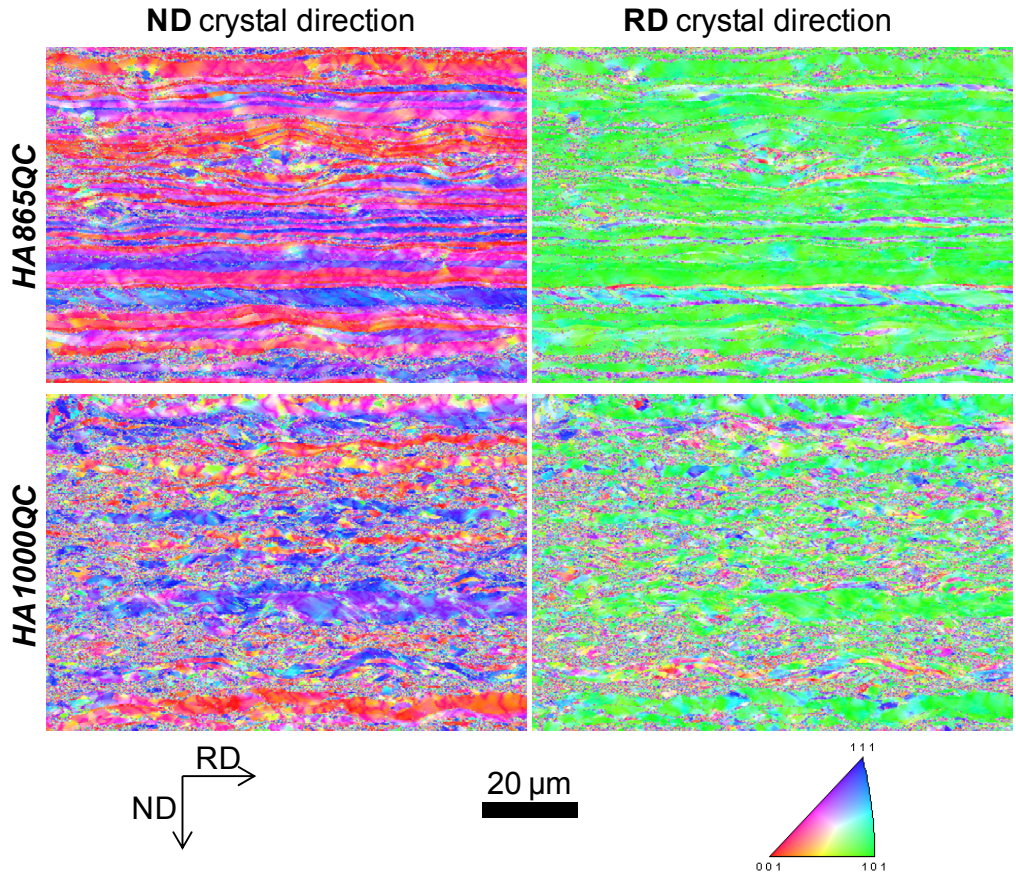


**Fig. 6.8.** Orientation maps based on the TD plane EBSD scan of HA865QC and HA1000QC cold rolled sheets denoting the crystal directions parallel to the ND and RD.

### 6.3.2. r-value

The angular dependence of r-value for the HA865QCA and HA1000QCA route sheets is shown in Fig. 6.9. The trend is very similar to the one observed in the case of HCA route sheets as  $r_{45} > r_{90} > r_0$ . This r-value trend is usually characteristic of ferritic steels with a high density of  $\alpha$ -fiber oriented grains. This was confirmed by the ODFs based on the EBSD scan of the full RD section of sheets (Fig. 6.10) which indicate a high intensity of the  $\alpha$ -fiber texture in both cases. In spite of the higher intensity of the  $\gamma$ -fiber in the HA865QCA route sheet, it has a lower mean r-value than the HA1000QCA route sheet which is mainly due to its lower r-value at 45 ° to RD.



Averaging r-values measured at a larger number of angles is expected to lead to more justified mean r-values. Considering the trend of r-value in Fig. 6.9, the HA865QCA route sheet has a smaller planar anisotropy indicative of less susceptibility to earing during deep drawing than the HA1000QCA route sheet.

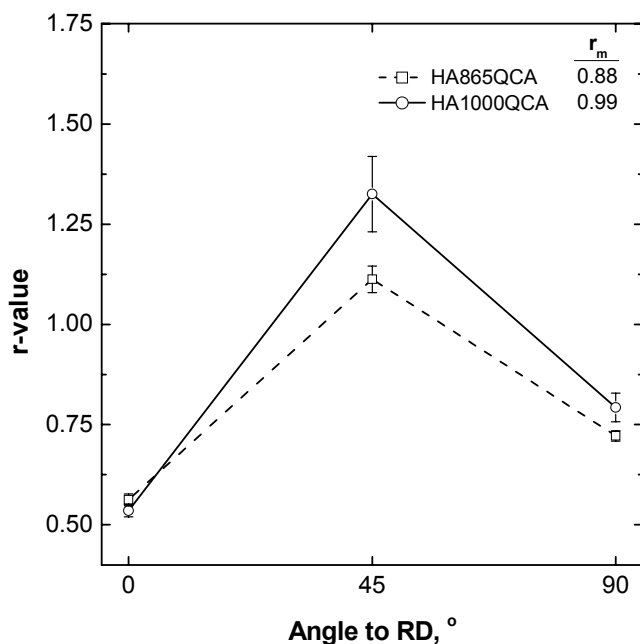


**Fig. 6.9.** Angular dependence of r-value and mean r-value for the HA865QCA and HA1000QCA processed sheets.

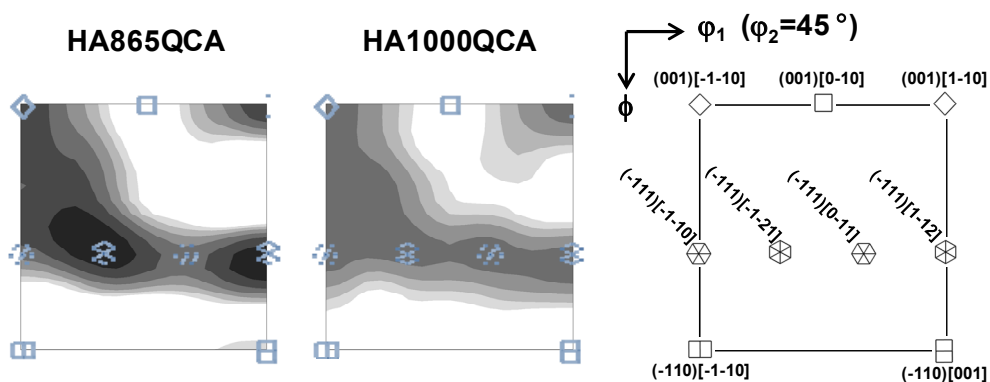


**Fig. 6.10.** ODF of final HA865QCA and HA1000QCA route sheets obtained from the EBSD scan of full RD section.

#### 6.4. Conclusions

Intercritically annealed hot strips containing about 15% and 35%  $\alpha'$  martensite in a ferritic matrix were cold rolled and annealed in order to assess the effect of  $\alpha'$  on the ridging resistance and formability. The following conclusions were drawn:

1- Presence of hard  $\alpha'$  during cold rolling enhances the ridging resistance of cold rolled and annealed sheets. No apparent evidence of grain colonies of any type was found when a hot strip containing about 35%  $\alpha'$  was cold rolled. Presence of hard  $\alpha'$  during cold rolling leads to shear band formation and thus fragmentation of elongated ferrite grains. Later on, recrystallization of this microstructure causes formation of fine grains with a weak texture which is favorable in view of the ridging resistance.

2- High density of  $\alpha$ -fiber oriented grains in the HAQCA routes leads to high r-values at 45 ° to RD and low r-values at 0 ° and 90 ° to RD. This causes a high planar anisotropy of r-value. In spite of a high ridging resistance in the HAQCA route, the mean r-values are still lower than unity.



## Chapter VII

# Thermal Restoration Mechanisms in Fully Ferritic and Dual-Phase ( $\alpha+\alpha'$ ) Microstructures

### 7.1. Introduction

Good visual appearance is a major requirement in applications where ferritic stainless steels are used. Ridging, the formation of corrugations parallel to the Rolling Direction (RD), is a common surface defect associated with the cold formed ferritic stainless steel sheets, which deteriorates their visual appearance. Ridging is however known to be less noticeable in the transformable types of ferritic stainless steels which have a ( $\alpha+\gamma$ ) microstructure at hot rolling temperatures [1]. The presence of high temperature austenite in the transformable ferritic stainless steels allows for the presence of  $\alpha'$  martensite during cold rolling and this improves the ridging resistance by reducing the formation of similarly oriented ferrite grain colonies parallel to the RD [2]. Cold rolling is usually followed by a recrystallization annealing step below the austenite start temperature,  $A_{e1}$ , which renders the sheets soft and makes them ready for the final shaping operation. Therefore, the differences in the recrystallization behavior of cold rolled ferrite and cold rolled dual phase ( $\alpha+\alpha'$ ) microstructures are particularly relevant to the ridging phenomenon. Although martensite has a very high dislocation density, comparable to that of heavily cold rolled ferrite, it is very stable against

recrystallization and does not recrystallize even after prolonged holding times at temperatures just below the  $A_{c1}$  temperature [3-4]. One possible explanation could be the homogenous distribution of dislocations in the martensite, which is very different from the deformed ferrite in which the cell boundaries serve as heterogeneous nucleation sites for recrystallization [5]. Tsuchiyama [6] holds that the block boundaries, which are misoriented by only about  $10.5^\circ$ , are very stable and do not migrate easily. The high angle boundaries with misorientations in the range of  $15-45^\circ$ , on the other hand, show high mobilities and their outward bulging causes grain growth in the course of the recrystallization. An alternative mechanism to account for the high stability against the recrystallization of martensite is the instantaneous formation of fine precipitates in the supersaturated martensite upon reheating [7]. These precipitates can pin the dislocations and lath boundaries and retard the recrystallization. The 9%Cr steels used in power plant applications owe their excellent creep resistance to their martensitic matrix stabilized by the pinning effect of closely spaced fine precipitates [8]. In low carbon steels, reduction of the carbon content to levels below 100 ppm has been found to speed up the disappearance of the lath martensite morphology. Even in this case, the boundaries of equiaxed ferrite grains were found to contain dislocation structures indicative of their formation by recovery rather than recrystallization [5]. Cold rolling of martensite in a 0.2%C steel was found to damage the lath martensite and improve the recovery and recrystallization kinetics [4]. The focus of this chapter is to identify the differences in the recrystallization behavior of a fully ferritic cold rolled microstructure and that of a dual phase ( $\alpha+\alpha'$ ) cold rolled microstructure.

## **7.2. Experimental Procedure**

3 mm-thick hot rolled strips of standard AISI 430 composition were used in the recrystallization studies after the following two heat treatments. The first heat treatment was batch annealing simulation at  $820^\circ\text{C}$  for 5 hrs, slightly below the  $A_{c1}$  temperature of  $850^\circ\text{C}$ , in order to achieve a microstructure composed of a fully ferritic matrix and embedded  $M_{23}C_6$  precipitates, typically in the size range of  $0.1-0.5\ \mu\text{m}$ . The second heat treatment procedure was similar to the first heat treatment with

an additional one-minute soaking at the intercritical temperature of 950 °C as the final step. This treatment led to the partial dissolution of carbides and the formation of approximately 25 vol. % austenite, which transformed to  $\alpha'$  martensite upon cooling to room temperature. Optical light micrographs of annealed hot strips just prior to cold rolling are shown in Fig. 7.1. The 3 mm-thick hot strips with and without  $\alpha'$  martensite, denoted dual phase and ferritic onwards, were subsequently cold rolled to true strains of either 0.84 or 1.79 to final thicknesses of either 1.3 mm or 0.5 mm, respectively. Unless otherwise stated, the results for the 1.3 mm-thick sheets are reported. The cold rolled specimens were heat treated for different times below the  $A_{e1}$  temperature to study the effect, on the recrystallization behavior, of the initial microstructure, by means of hardness measurement, optical light microscopy, Transmission Electron Microscopy (TEM), and Electron Backscattering Diffraction (EBSD).

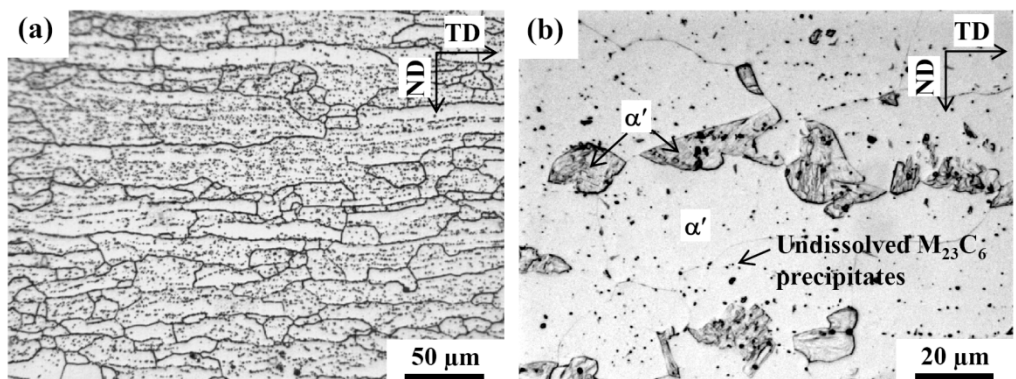


**Fig. 7.1.** Optical micrographs showing the microstructure of (a) ferritic and (b) dual phase ( $\alpha+\alpha'$ ) hot rolled strips with a thickness of 3 mm, used in the cold rolling experiments.

### 7.3. Results and Discussion

Fig. 7.2 compares the hardness evolution of the ferritic and dual phase cold rolled sheets after heating to 830 °C at a heating rate of 50 °C/s and holding for different times. The higher hardness of the dual phase microstructure in the cold rolled state is due to the presence of the hard martensite phase in the microstructure. In the case of

the ferritic microstructure, softening due to the recrystallization took place almost instantly as the annealing temperature was reached and the hardness reached a base level in the range of 140-145 HV after only 2 sec. In the case of the dual phase microstructure, however, the base hardness level corresponding to the equivalent dislocation-free microstructure was not reached even after a holding time of 10 min.

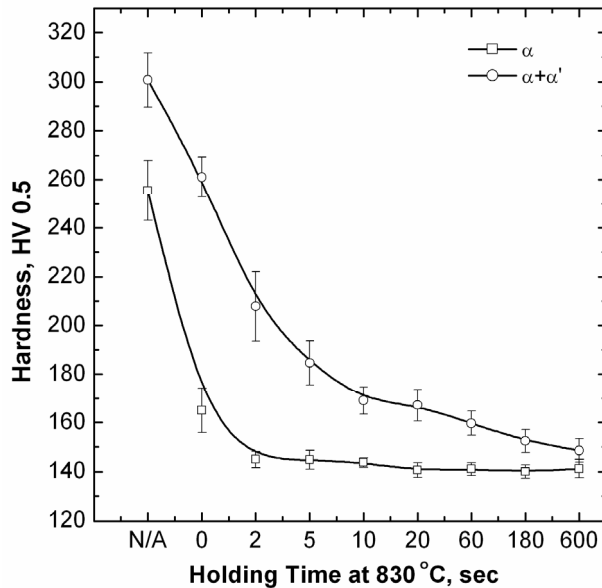


**Fig. 7.2.** Hardness changes as a function of annealing time, for fully ferritic ( $\alpha$ ) and dual phase ( $\alpha+\alpha'$ ) cold rolled sheet. The as cold rolled state is denoted by N/A.

Fig. 7.3 shows the cross sectional optical micrographs of as cold rolled and annealed sheets of dual phase and ferritic microstructures. In the case of the ferritic sheet, the as cold rolled microstructure was dominated by elongated grains of ferrite in which weakly etched sets of parallel lines, corresponding to cell walls, were also visible (Fig. 7.3(a)). The dual phase sheet, on the other hand, had a cold rolled microstructure composed of deformed ferrite grains embedding martensitic regions. The bulk martensite regions did not exhibit much elongation in the rolling direction because of their much higher strength compared to the ferritic matrix (Fig. 7.3(b)). One of the features of the cold rolled dual phase steel not observed in the ferritic steel was the presence of shear bands making an angle of about 25-45 ° with the RD, as seen in the

RD-ND plane sections. This indicates that the instability of homogenous deformation through a pure glide mechanism activated the local deformation through the shear band formation as well. When the cold rolled ferritic sheet was heated to 830 °C and immediately quenched (Fig. 7.3(c)), majority of the elongated cold rolled grains were recrystallized which is in agreement with the observed abrupt drop in the hardness. The same treatment for the dual phase sheet caused recrystallization of only a small fraction of the ferrite grains (Fig. 7.3(d)). Shear bands and regions in the vicinity of the martensite appeared to be the favorable sites for the recrystallization of strained ferrite. After an annealing time of 5 sec, all the ferrite grains in the ferritic sheet recrystallized (Fig. 7.3(e)). The fraction of recrystallized ferrite in the dual phase sheet also increased dramatically after annealing for 5 sec (Fig. 7.3(f)). Martensite in the dual phase microstructure, however, showed a high resistance to recrystallization which is responsible for the high hardness readings in the case of the dual phase microstructure.

Partitioning of stress and strain during deformation of multi-phase microstructures is a well-known concept [9]. Hence, the strain accommodated by the soft ferritic matrix of the dual phase microstructure is higher than for the hard martensite. This means that at an identical cold reduction ratio, the strain accommodated by the ferrite in the dual-phase steel, which is the driving force for the recrystallization, is larger than in the ferrite in the fully ferritic microstructure. The contradictory observation of delayed recrystallization of ferrite in the dual phase microstructure can therefore be related to one or a combination of the following factors:

- The stored energy in deformed metals is usually small compared to the energy changes associated with phase transformations [10]. As a result, phase transformations such as precipitation reactions have a pronounced effect on the recrystallization behavior. The delayed recrystallization of ferrite in the dual phase steel may therefore be related to the competition between the recrystallization of ferrite and the formation of precipitates from the supersaturated martensite.



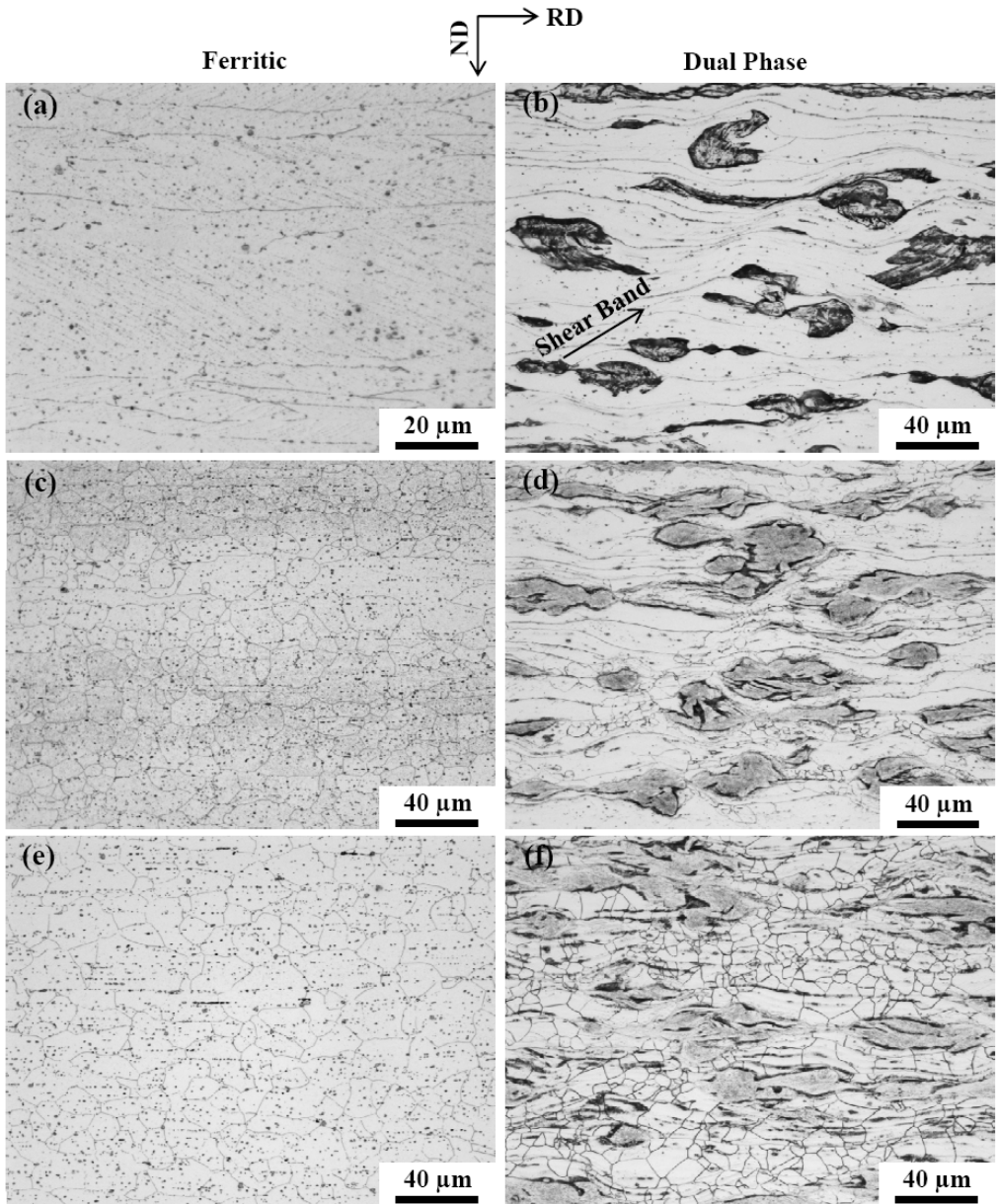


**Fig. 7.3.** Microstructural evolution during annealing of 1.3 mm-thick cold rolled sheet of ferritic (left) and dual phase (right) steel. (a) and (b) show the cold rolled microstructure. (c) and (d) show the microstructures after rapid heating to 830 °C followed by immediate quenching. (e) and (f) show the microstructures after annealing for 5 sec at 830 °C.

- Local strain accommodation by shear bands observed in the dual phase microstructure may reduce the strain accommodated by the unsheared ferrite regions. This is evidenced by the more ready recrystallization of ferrite along the highly deformed shear band regions.
- The material flow during plane straining of the fully ferritic microstructure remains more or less laminar. When martensite is present too, the laminar flow of ferrite is disturbed. The EBSD orientation maps of Fig. 7.4 demonstrate the differences in the microstructure of ferritic and dual phase steels cold rolled to a thickness of 0.5 mm. Activation of a lower number of operative slip systems in the laminar flow can lead to the accumulation of more dislocations on the few active glide planes which can potentially lead to a higher driving force for recrystallization.

The limited spatial resolution and the non-uniform etching of the martensite phase make it difficult to study of the evolution, upon annealing, of the martensite phase by means of the optical microscopy alone. Therefore, the recrystallization behavior of martensite was followed by a combination of sequential EBSD and TEM. EBSD orientation maps of Fig. 7.5 show the microstructure in an area of the dual phase cold rolled sheet after annealing for different times at 830 °C, in a vacuum of better than  $5 \times 10^{-5}$  mbar. This measure was taken to minimize the surface oxidation after each annealing step. Heating and cooling rates, of the order of 50 °C/s, were applied. The location of the martensite and ferrite phases is indicated approximately by the delineations on the micrographs in Fig. 7.5(a). The recrystallization initiates in the ferritic regions in the vicinity of martensite and then quickly spreads to the rest of the ferrite. No clear recrystallization nuclei were found in the martensite and the restoration from the dislocated microstructure of martensite took place by the penetration of the recrystallization front in to the martensitic substructure. As the arrows on the orientation maps of Fig. 7.5 indicate, the penetration direction tends to be aligned with the length of the martensite blocks.

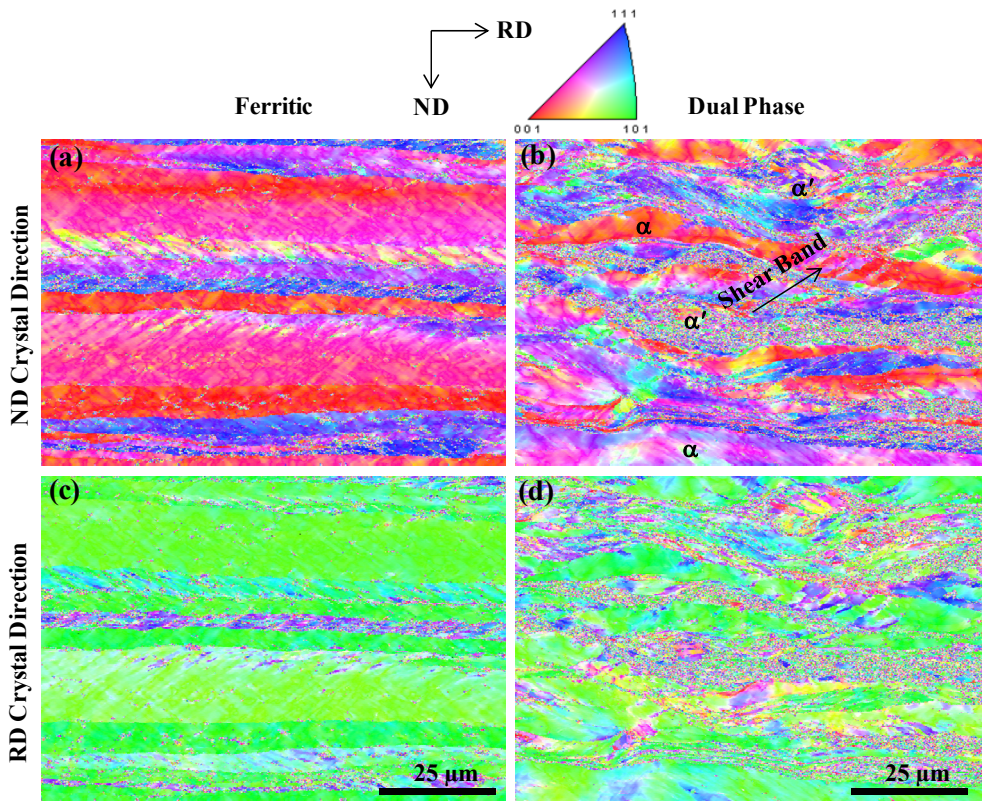


**Fig. 7.4.** EBSD orientation maps denoting the crystal directions parallel to the normal direction (top) and the rolling direction (bottom) of 0.5 mm-thick cold rolled sheets of ferritic (left) and dual phase (right) steels.



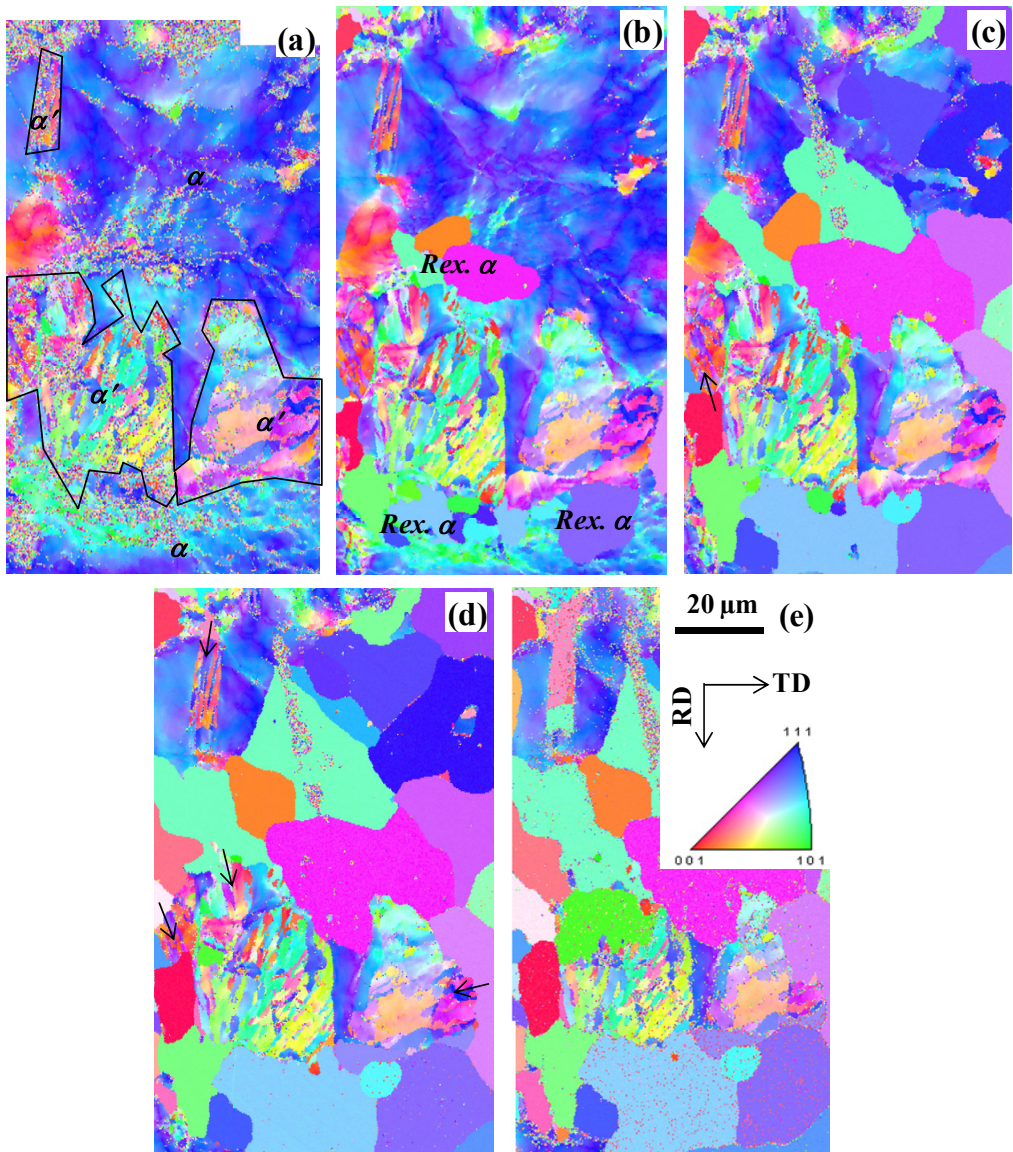


**Fig. 7.5.** EBSD orientation maps denoting the crystal directions parallel to the normal direction of dual phase steel with a thickness of 1.3 mm. The as cold rolled sheet without annealing (a) and after annealing at 830 °C for 0 s (b), 2 s (c), 17 s (d), and 197 s (e) are shown. Arrows indicate the growth direction of the ferrite recrystallization front into the martensite.

TEM micrographs of Fig. 7.6 show the microstructure of dual phase cold rolled sheet after rapid heating to 750 °C followed by quenching to room temperature. This

treatment caused the occurrence of partial recovery (Fig. 7.6(a)) and recrystallization (Fig. 7.6(b)) in the ferritic regions. In accordance with the EBSD results, the martensite phase, which occasionally contained internal twins, retained its morphology (Fig. 7.6(c)) and did not recrystallize. The relatively straight martensite lath boundaries are indicative of a small deformation of martensite and strain concentration in the ferrite phase. Very fine precipitates were observed in the martensitic parts of the microstructure. Examples of in-lath and twin boundary precipitates are shown in Fig. 7.6(d,e).

TEM examinations were also performed on the dual phase steel sheets with a cold rolled thickness of 0.5 mm after salt bath annealing for 15 sec at 830 °C. TEM micrographs of Fig. 7.7(a,b) show that the growth, to the martensite phase, of the ferrite recrystallization front preferentially takes place parallel to the length of the martensite plates rather than normal to them. This is due to the high density of the lath boundary precipitates which act as obstacles to the lateral bulging, to the martensite laths, of the recrystallization front. The precipitates are mainly  $M_{23}C_6$  type carbides (M denoting Cr and Fe) although the presence of  $M_2N$  type nitrides is also possible. The formation of these precipitates from the supersaturated martensite is kinetically very fast so that, as shown in Fig. 7.6(d,e), they form even upon quick heating to 750 °C and immediate quenching. As demonstrated in Fig. 7.7(c), precipitates are not limited to the lath boundaries but can also be found within the laths. However, the lateral bulging of the recrystallization front to the lath boundaries would require an additional pinning force to be overcome. Fig. 7.7(c) also shows the occurrence of recovery within the martensite. This reduces the energy difference between the recrystallized ferrite and martensite, i.e. the driving force for the propagation of recrystallized ferrite into the martensite. Therefore, after the initial fast recrystallization of martensite through the bulging mechanism, the remaining martensite will restore from the dislocated substructure by a recovery mechanism.

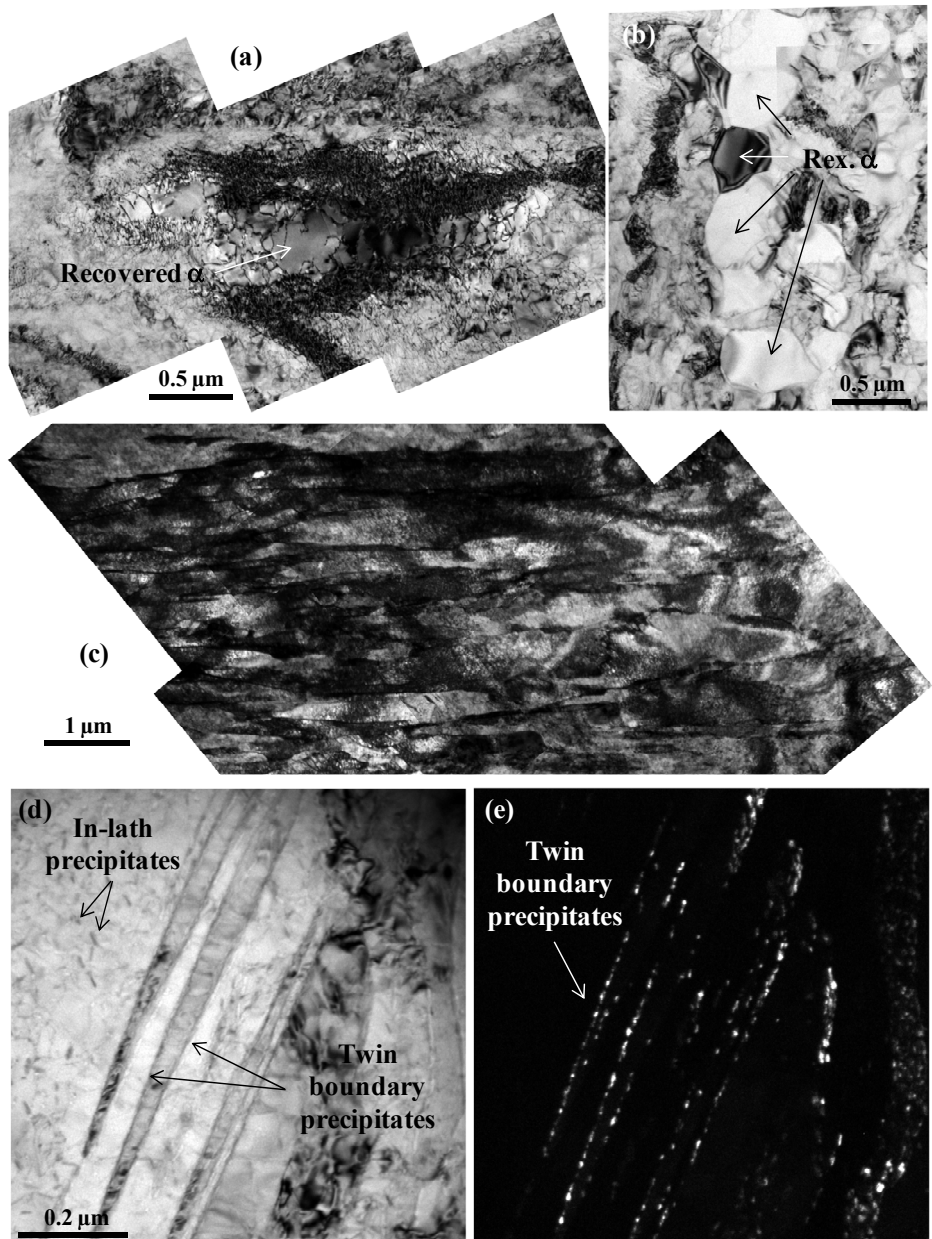


**Fig. 7.6.** TEM micrographs of the RD-TD plane of 1.3 mm-thick dual phase ( $\alpha+\alpha'$ ) steel after fast heating to 750 °C and immediate quenching. (a) and (b) show areas of recovery and recrystallization in the deformed ferrite, respectively. (c) shows the lath structure of the martensite. The bright field image of internal twins in a martensitic lath and the precipitates within the lath and in the twin boundaries are shown in (d). (e) is the dark field image of (d) indicating the presence of the twin boundary precipitates.

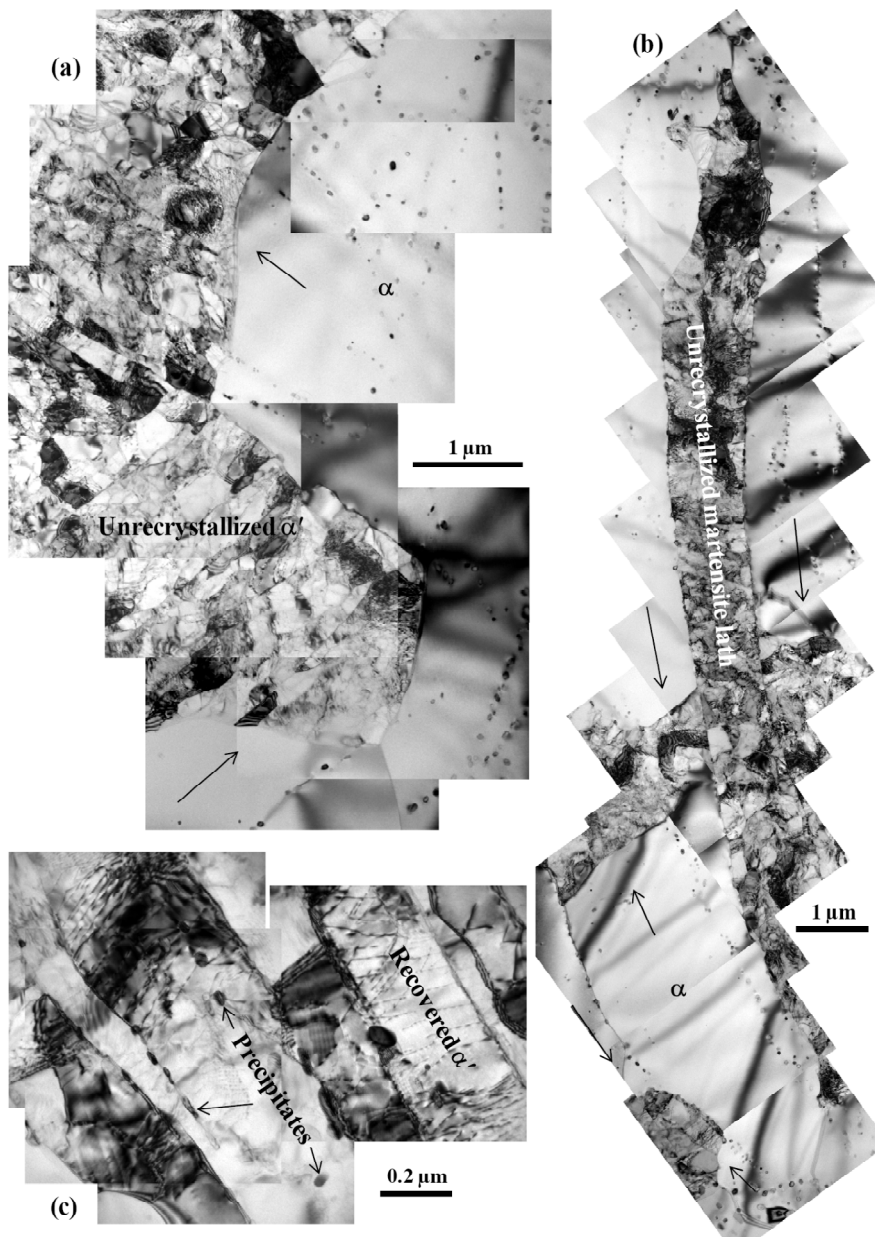


**Fig. 7.7.** TEM montages of the RD-TD plane of 0.5 mm-thick dual phase steel after salt bath annealing at 830 °C for 15 sec. (a) and (b) illustrate the longitudinal bulging of the recrystallized ferrite into the martensite laths. Arrows indicate the propagation direction of the ferrite/martensite boundary. (c) Microstructure of unrecrystallized martensite showing lath boundary and in-lath precipitates as well as recovered martensite.

#### 7.4. Conclusions

The following conclusions were drawn about the annealing response of cold rolled sheets of the AISI type 430 transformable ferritic stainless steel with a fully ferritic and a dual phase ferritic-martensitic microstructures:

1- Recrystallization of the dual phase microstructure was significantly slower than for the fully ferritic microstructure. This was mainly due to the slow recrystallization and recovery of the martensite phase. Nevertheless, even the ferrite in the dual phase steel showed a slightly delayed recrystallization compared to the ferrite in the fully ferritic steel.

2- Shear bands were observed in the cold rolled microstructure of the dual phase steel. This indicates the instability of strain accommodation by a pure glide mechanism during cold rolling of the dual phase steel.

3- The sluggish recrystallization of the martensite is very likely related to the immediate formation of fine precipitates upon annealing. These precipitates, which form both within the laths and in the lath boundaries, can pin the martensite boundaries and dislocations and interfere with the recrystallization of martensite.

4- Recrystallization of martensite in the early annealing stage was found to take place by bulging of the recrystallized ferrite grains into the martensitic substructure. The presence of arrays of lath boundary precipitates caused bulging to preferentially take place parallel to the length of the laths. At later stages of annealing, the stored energy of unrecrystallized martensite decreased as a result of the partial annihilation of dislocations, and recovery became the dominant restoration mechanism.

#### 7.5. References

- [1] H. J. Shin, *et al.*, "The effect of texture on ridging of ferritic stainless steel," *Acta Materialia*, vol. 51, pp. 4693-4706, 2003.
- [2] J. Mola, *et al.*, "Influence of texture on ridging and formability of 16%Cr ferritic stainless steel," *Solid State Phenomena*, vol. 160, pp. 153-158, 2010.



- [3] M. Natori, *et al.*, "Difference in recrystallization behavior between lath martensite and deformed ferrite in ultralow carbon steel," *Scripta Materialia*, vol. 53, pp. 603-608, 2005.
- [4] S. Takaki, *et al.*, "Influence of cold working on recovery and recrystallization of lath martensite in 0.2%C steel," *Nippon Kinzoku Gakkaishi/Journal of the Japan Institute of Metals*, vol. 55, pp. 1151-1158, 1991.
- [5] T. Maki, "Recent advances in understanding martensite in steels," in *The 1st International Symposium on Steel Science*, Kyoto, Japan, 2007, pp. 1-10.
- [6] T. Tsuchiyama, *et al.*, "Conditions for grain boundary bulging during tempering of lath martensite in ultra-low carbon steel," *ISIJ International*, vol. 50, pp. 771-773, 2010.
- [7] T. Tsuchiyama, *et al.*, "Recrystallization of Lath martensite with bulge nucleation and growth mechanism," *ISIJ International*, vol. 41, pp. 1047-1052, 2001.
- [8] F. Abe, *et al.*, "Stabilization of martensitic microstructure in advanced 9Cr steel during creep at high temperature," *Materials Science and Engineering A*, vol. 378, pp. 299-303, 2004.
- [9] B. C. De Cooman and J. G. Speer, *Fundamentals of Steel Product Physical Metallurgy*. Warrendale: Association for Iron and Steel Technology, 2011.
- [10] F. J. Humphreys and M. Hatherly, *Recrystallization and Related Annealing Phenomena*, 2nd ed. Oxford: Elsevier Ltd, 2004.



## Chapter VIII

# Recrystallization Behavior in Fully Ferritic and Dual-Phase ( $\alpha+\alpha'$ ) Microstructures

### 8.1. Introduction

Introduction of fresh martensite during cold rolling of AISI 430 ferritic stainless steel (HAQCA route) was shown in chapter 6 to be associated with a significant improvement in the ridging resistance. The r-values associated with the HAQCA route were not, however, satisfactory. Double step cold rolling with an intermediate annealing step has been reported to improve both the ridging resistance and the r-value for a transformable [1] and a non-transformable [2] ferritic stainless steel. This chapter evaluates the influence, on the ridging and formability characteristics, of the presence of  $\alpha'$  martensite prior to double step cold rolling of the AISI type 430 transformable ferritic stainless steel.

### 8.2. Experimental Procedure

A 3 mm-thick hot rolled strip of standard AISI 430 composition was used for the processing routes schematically shown in Fig. 8.1. Hot rolled strips were heat treated so as to obtain two distinct microstructures prior to cold rolling. The first heat treatment (Fig. 8.1(a,b)) involved annealing for 5 hrs at 820 °C, slightly below the  $A_{c1}$  temperature of 850 °C, in order to achieve a microstructure composed of a fully

ferritic matrix and embedded precipitates, typically in the size range of 0.1-0.5  $\mu\text{m}$ . The second heat treatment procedure (Fig. 8.1(c,d)) was similar to the first heat treatment but involved an additional one-minute soaking at the intercritical temperature of 950 °C as the final step. This treatment caused partial dissolution of precipitates and formation of approximately 25 vol. % austenite, which transformed to  $\alpha'$  martensite upon cooling to room temperature. Optical light micrographs of the annealed hot strips used for the cold rolling operations were shown in Fig. 7.2 (chapter 7). The 3 mm-thick hot strips with and without  $\alpha'$  martensite, which will be referred to as dual phase and ferritic in the text, were subsequently cold rolled to a final thickness of 0.5 mm, through Single Step Cold Rolling (SCR) and Double Step Cold Rolling with an intermediate anneal (DCR) as sketched in Fig. 8.1. In the DCR processing, the intermediate annealing times at 830 °C of 30 s, 30 min, and 5 hrs were applied. Intermediate annealing treatments were performed by placing sheets in a box furnace already taken to the annealing temperature. A salt bath annealing for 30 s was also carried out to examine the influence of a higher heating rate in the intermediate annealing step.

The r-value was computed manually by measuring the width change, after straining by 15%, of ASTM E8 standard tensile specimens. For ridging assessment, 25 mm-wide tensile specimens parallel to RD were used.

Electron Backscattering Diffraction (EBSD) technique was used to determine the texture of sheets. Due to the likelihood of through-thickness texture inhomogeneities, full RD sections of sheets were used in the EBSD measurements. The microstructural examinations were performed in a JEOL JEM-2100 Transmission Electron Microscope (TEM) operating at 200 kV.

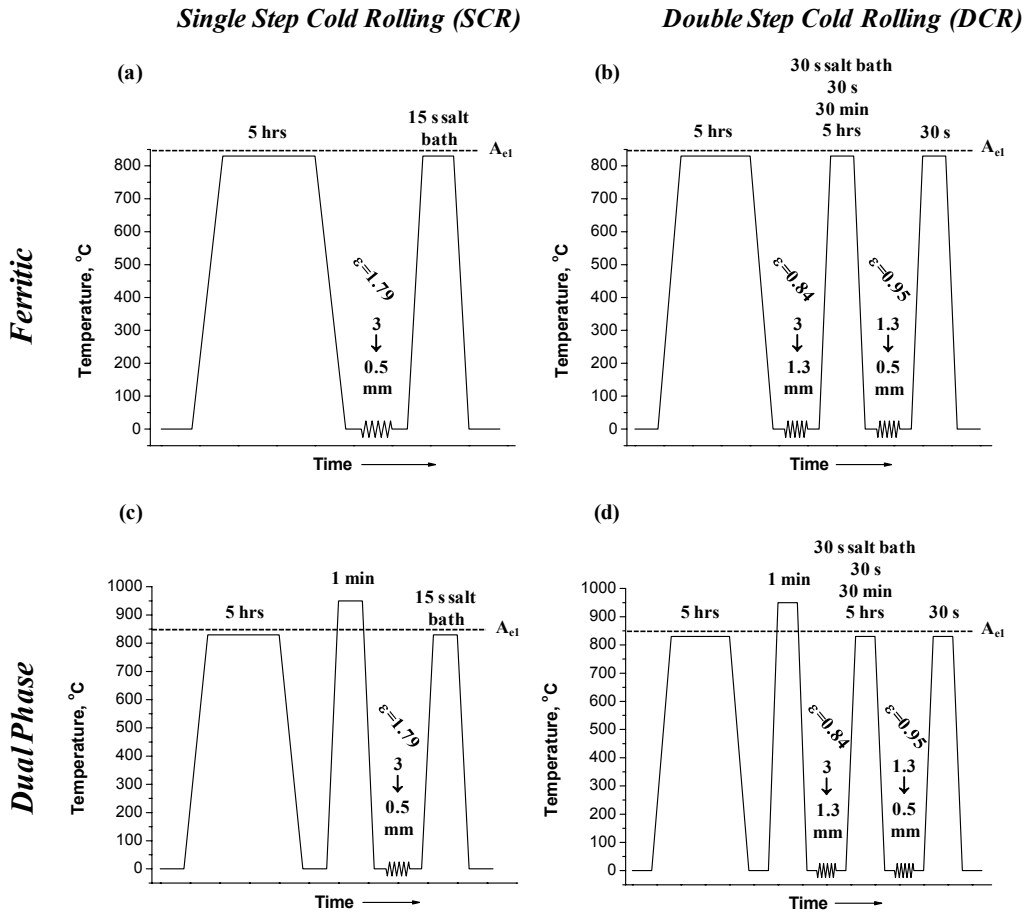


**Fig. 8.1.** Schematic representation of the thermal cycles to obtain ferritic **(a,b)** and dual phase **(c,d)** microstructures in the hot rolled strips prior to the SCR **(a,c)** and DCR **(b,d)** thermomechanical processing routes.

### 8.3. Results and Discussion

Fig. 8.2 shows the angular dependence of r-value and dependence on the processing conditions of the mean r-value and  $\Delta r$  for the SCR and DCR sheets of ferritic and dual phase microstructures.

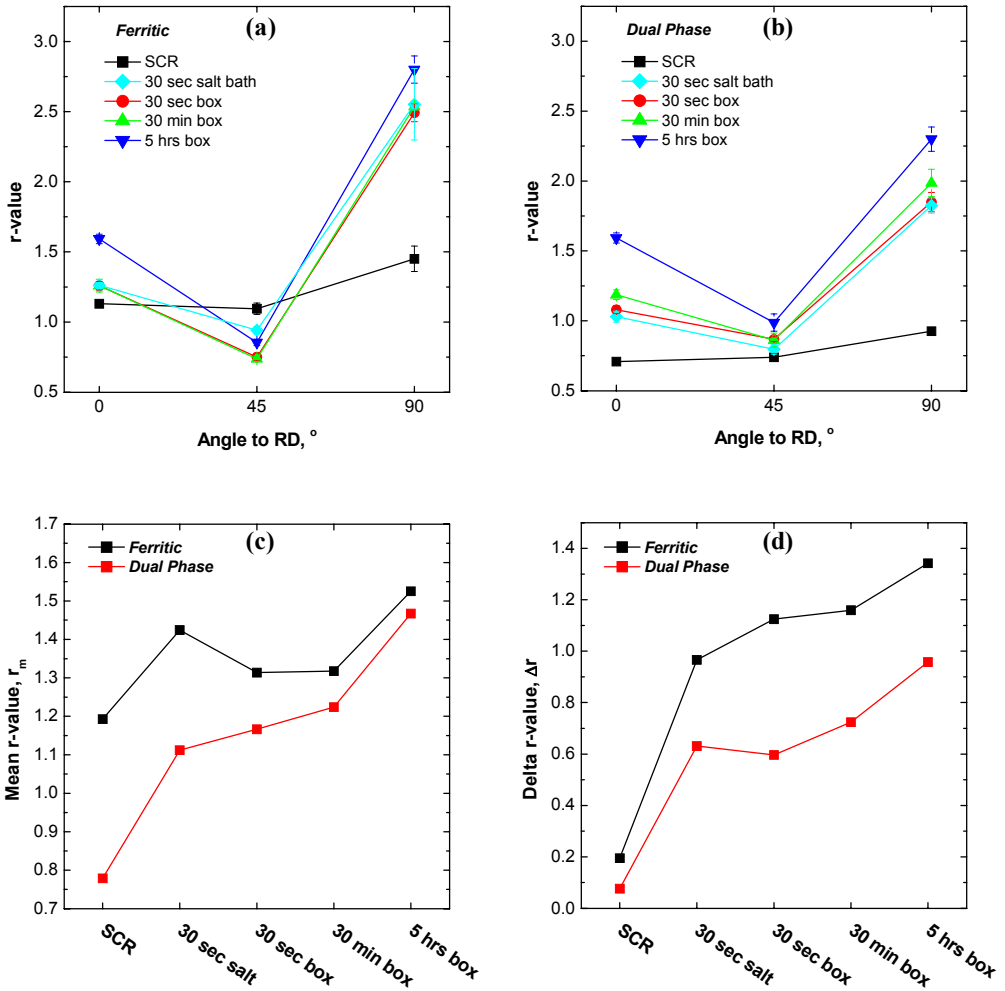


**Fig. 8.2.** Angular dependence of r-value for the ferritic (a) and the dual phase (b) steels after different processing conditions. (c) and (d) show the mean r-values and  $\Delta r$ -values.

High mean r-values and  $\Delta r$ -values close to zero are desirable in view of the formability. A high normal anisotropy allows high deep drawing ratios to be applied and a low  $\Delta r$ -value ensures that the earing will be minimized during deep drawing. In ferritic steels, these conditions can best be achieved in sheets possessing a strong  $\gamma$ -fiber texture, *i.e.* with  $\langle 111 \rangle //$  Normal Direction (ND) [3].

According to Fig. 8.2, dual phase and ferritic steels processed according to SCR both display very small  $\Delta r$ -values. The SCR processed ferritic steel, however, shows a significantly higher  $r_m$  than the dual phase steel. EBSD examination of the SCR processed dual phase steel indicated the presence of unrecrystallized martensite in the microstructure (Fig. 8.3). This is in agreement with the well-documented resistance to the recrystallization of martensite [4-5] although mechanical deformation is known to aid the recrystallization of martensite [6]. As discussed in detail in chapter 7, the presence of martensite in the dual phase steel resulted in the formation of shear bands during cold rolling which act as favorable nucleation sites in the ferrite. Ferritic regions adjacent to the hard martensite also exhibit an enhanced recrystallization. The nucleation of recrystallized grains within the martensite, on the other hand, is very limited. In such cases, recrystallization of martensite takes place through the bulging of recrystallized ferrite grains into the martensitic substructure. Concurrently, recovery proceeds in the regions of martensite distant from the martensite/ferrite boundary. Therefore, the driving force for the bulging of the recrystallization front into the martensite decreases at later stages of annealing and makes recovery the dominant restoration mechanism.

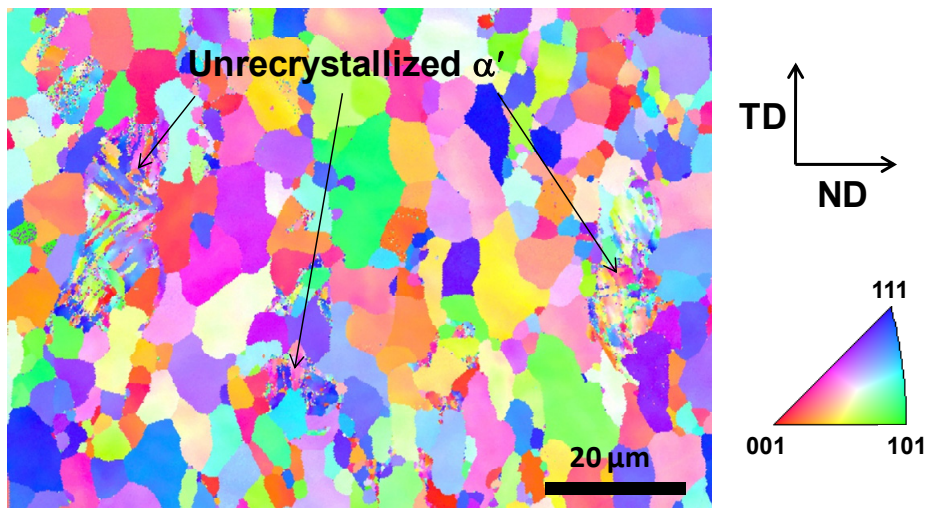


**Fig. 8.3.** EBSD orientation map indicating crystal directions parallel to the ND of the SCR processed dual phase steel.

The  $\phi_2=45^\circ$  section of the Orientation Distribution Function (ODF) based on the EBSD scan of full RD section of final sheets is shown in Fig. 8.4. In comparison with the ferritic sheet, the SCR processed sheet of the dual phase steel exhibits a weaker texture as evidenced by a lower maximum intensity and a wider distribution of the texture component intensities across the ODF section. The weak texture associated with the low  $r$ -values observed in the case of the SCR processed dual phase steel can be partly attributed to the incomplete recrystallization of martensite with multiple crystallographic variants. Another important contribution to the weak texture could arise from the recrystallization within the shear bands and in the ferritic regions adjacent to the martensite.

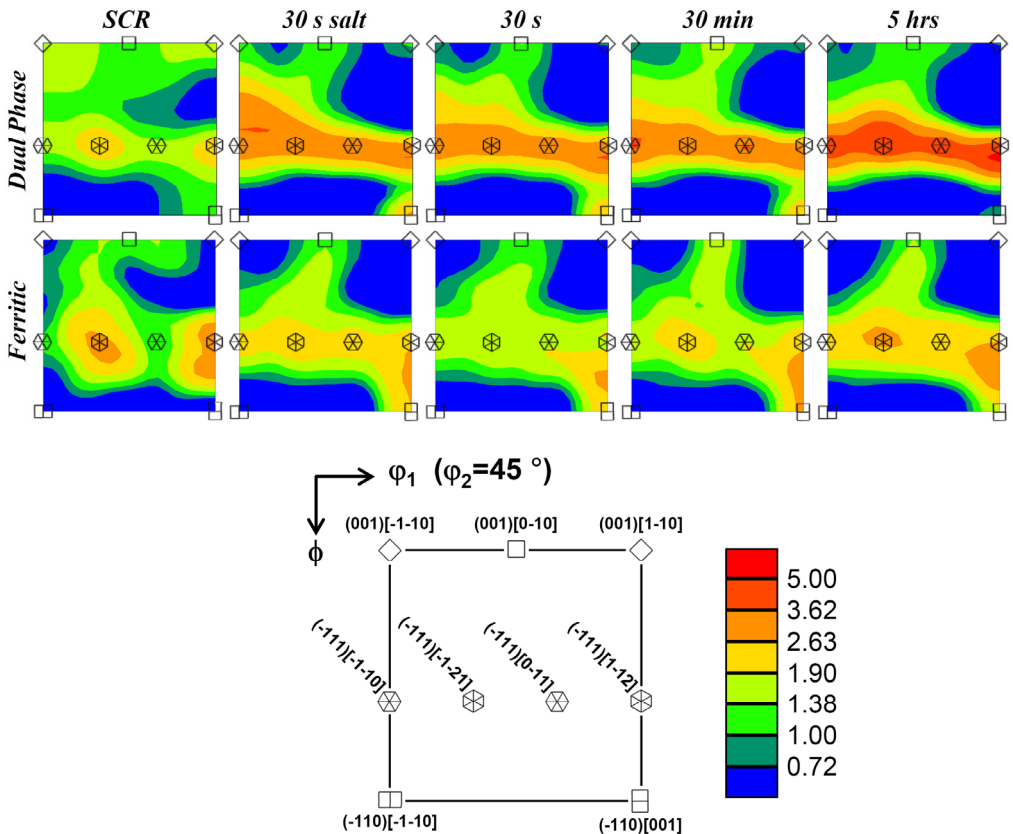


**Fig. 8.4.** ODF of final sheets obtained from the EBSD scan of full RD sections.



Referring to Fig. 8.2(a,b), the DCR processing of both steels results in r-value profiles characterized by  $r_{45} < r_0 < r_{90}$ . This r-value trend is associated with higher  $\Delta r$ -values compared to the SCR processing (Fig. 8.2(d)). The high  $\Delta r$ -values in the DCR processing route are compensated by higher mean r-values which are caused by higher  $r_0$  and  $r_{90}$  values in comparison with the SCR processing route. In the DCR processed sheets, r-values at  $90^\circ$  to RD are higher for the ferritic than for the dual phase microstructure. The r-value is known to be closely controlled by texture. The angular dependence of r-value for various texture components of importance to ferritic steels was previously shown in Fig. 5.21 of chapter 5. These trends were redrawn from the existing crystal plasticity calculations based on the relaxed constraint method [7-8]. According to Fig. 5.21, the r-value at  $90^\circ$  to RD increases for the texture components belonging to the TD-fiber ( $\langle 110 \rangle //$  Transverse Direction (TD)) as the Goss orientation ( $\{110\} \langle 001 \rangle$ ) is approached. Therefore, as the ODFs in Fig. 8.4 show, the higher intensity of the TD-fiber texture components between the  $(\bar{1}11)[1\bar{1}2]$  and the Goss orientation is responsible for the higher  $r_{90}$  values in the case of the ferritic microstructure. One of the mechanisms by which the Goss texture component may arise is the application of low cold rolling reductions prior to the recrystallization [9]. Comparison of the ODFs for the SCR and DCR processing routes indicates that the distribution of the texture components along the  $\gamma$ -fiber of the DCR steel is more uniform than for the SCR steel. Favoring of a uniform  $\gamma$ -fiber texture by means of the DCR processing has been reported in several previous studies [1, 10-11]. The  $\{111\} \langle 112 \rangle$  orientation is known to be the most prominent recrystallization texture component after relatively large cold rolling reductions [9]. In such cases, however, the texture prior to cold rolling of ferrite is dominated by orientations belonging to the  $\alpha$ -fiber ( $\langle 110 \rangle //$  RD) in the midthickness and shear components such as Goss near the surface. This kind of texture is often found in the case of hot rolled AISI 430 [1]. In contrast, as exemplified in Fig. 8.5, the texture prior to the second cold rolling in the DCR processing is dominated by  $\gamma$ -fiber orientations in the case of the ferritic steel. Even in the dual phase steel, the texture is very different from the texture typical of an annealed hot strip. The texture after the second cold rolling of the DCR route sheets

should therefore be very different from the typical cold rolling textures obtained after cold rolling of a hot strip, because the crystallographic rotations which occur during cold rolling strongly depend on the initial texture. The uniform distribution of texture components along the  $\gamma$ -fiber in the DCR route can thus be attributed to the recrystallization of an unconventional cold rolling texture.

The thermal restoration mechanisms during annealing of cold rolled sheets with dissimilar initial microstructures are different. The influence of intermediate annealing conditions on the r-value and microstructure development of ferritic and dual phase sheets will be discussed separately. For the ferritic steel, according to the mean r-value results of Fig. 8.2, increasing the intermediate annealing time in the box furnace causes a gradual increase in the r-values. The increase is particularly pronounced in the case of a 5 hrs annealing. The higher r-values at longer intermediate annealing times can be attributed to the changes in the microstructure and the texture prior to the second cold rolling. The most important changes in this case are the ferrite grain growth and coarsening of the precipitates. Preferred growth of grains with certain orientations can modify the texture as well. This explains the stronger  $\gamma$ -fiber texture in the DCR processed ferritic steel with an intermediate annealing time of 5 hrs.

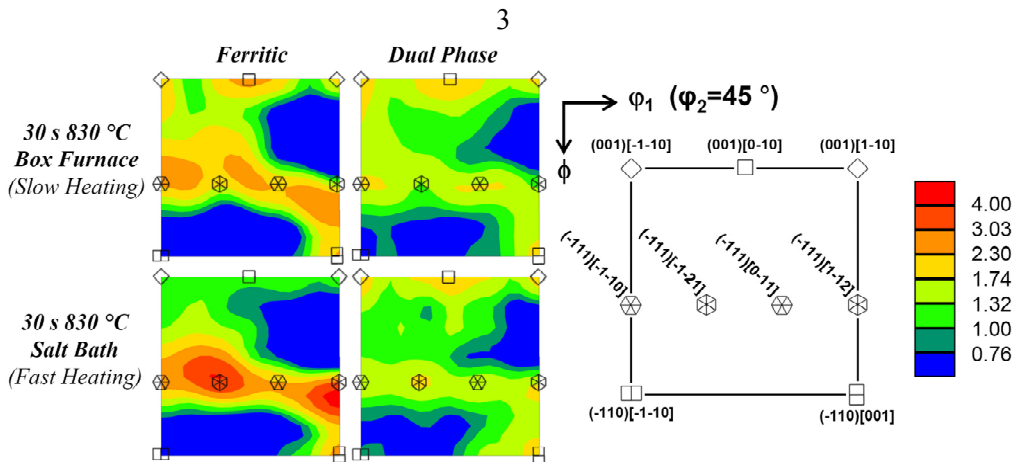


**Fig. 8.5.** ODFs of the 1.3 mm-thick intermediately annealed sheets prior to the second cold rolling step, obtained from the EBSD scan of full RD sections.

Applying a higher heating rate in the intermediate annealing step was found to strengthen the  $\gamma$ -fiber texture components in the final DCR processed ferritic sheet. As illustrated in the ODFs of Fig. 8.4, the final DCR processed sheet of the ferritic steel intermediately annealed in the salt bath developed a stronger  $\gamma$ -fiber texture compared to its box furnace annealed counterpart. This is in agreement with the superior mean  $r$ -values obtained in the case of salt bath intermediate annealing (Fig. 8.2). The effect of heating rate on the texture development during the intermediate annealing step can be understood more clearly by referring to the ODFs in Fig. 8.5. These represent the texture right after the intermediate annealing. The 1.3 mm-thick ferritic sheet annealed for 30 s at 830 °C develops a stronger  $\gamma$ -fiber texture when annealed in a salt bath than in a box furnace. Rapid heating has been reported to increase the recrystallization temperature and make it take place over a narrower temperature range [12-13] which can modify the prominence of recovery and recrystallization phenomena, thereby influencing the final recrystallization texture.

Due to the presence of martensite with a sluggish recrystallization behavior in the dual phase steel, the effect of intermediate annealing conditions on the  $r$ -value and texture evolution of the DCR processed dual phase steel is more pronounced than the ferritic steel. In this case, the intermediate anneal is additionally associated with a phase transformation as the precipitates form from the supersaturated martensite. According to Fig. 8.2, extending the intermediate annealing time results in higher mean  $r$ -values in the final sheets. In contrast to the ferritic microstructure where salt bath intermediate annealing caused improvement of the  $r$ -values, box furnace annealing of the dual phase steel results in higher mean  $r$ -values than the salt bath annealing. This arises because the lower heating rate in a box furnace increases the exposure time to temperatures which are high enough for the occurrence of thermal restoration processes. As a result, the extent of bulging recrystallization of martensite is larger during annealing in a box furnace. The bulging mechanism is especially dominant in the early stages of annealing, before depletion of the stored energy of the martensite through the competing recovery. The continued bulging recrystallization of martensite, recovery, and grain growth are the possible mechanisms to account for the texture

evolution upon extending the intermediate box annealing time from 30 s to 30 min. The microstructure after the intermediate anneal for 30 min of the cold rolled sheet with a thickness of 1.3 mm is shown in Fig. 8.6. This treatment caused the martensitic morphology to disappear but the precipitate size distribution remained broad. The large precipitates in Fig. 8.6 are the ones which persisted after the intercritical treatment while the finer ones have formed from the supersaturated martensite after the first cold rolling and annealing. At longer annealing times, recovery and grain growth become the only mechanisms governing the microstructure and texture evolution of the dual phase steel because of the reduced driving force for the bulging recrystallization of martensite.

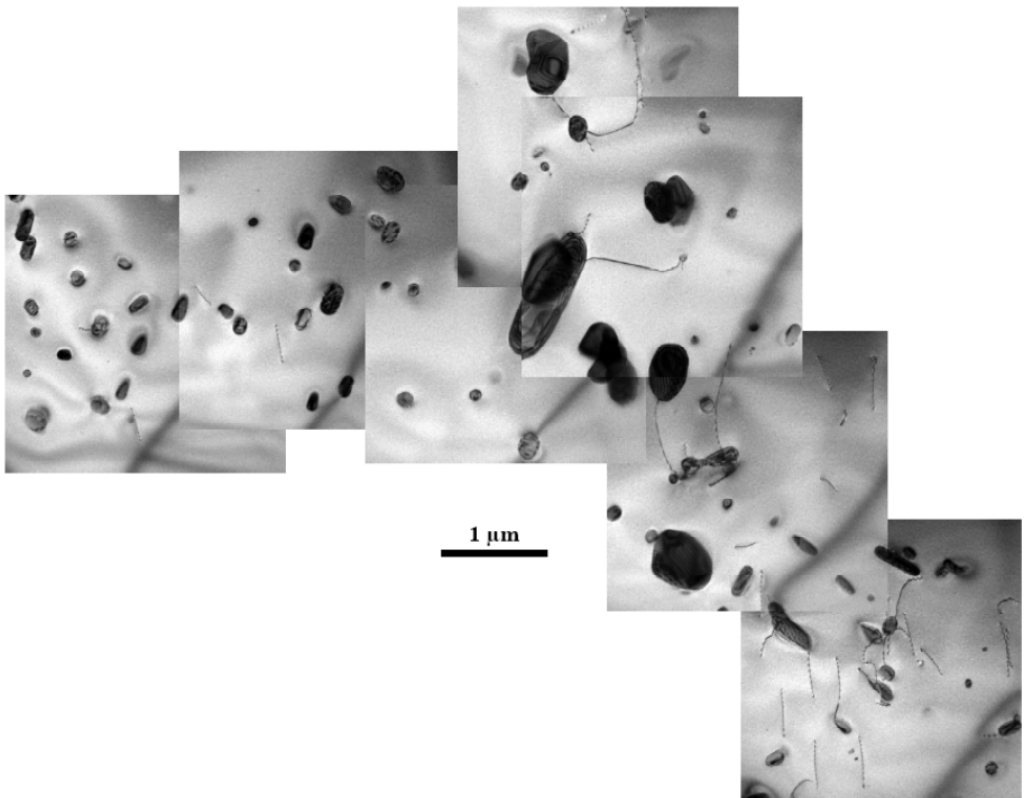


**Fig. 8.6.** TEM micrograph of the 1.3 mm-thick dual phase steel after intermediate annealing for 30 min in a box furnace.

When the intermediate annealing time of the dual phase steel is too short, for instance, after salt bath annealing for 30 s, there is still a fraction of unrecrystallized martensite in the microstructure. Martensite is, on the other hand, absent at the end of the DCR processing, *i.e.* after the second cold rolling and annealing treatment. The martensitic regions which do not recrystallize after the intermediate anneal undergo softening due to recovery and loss of tetragonality because of the formation of precipitates. Therefore, the martensite retained after the intermediate anneal will behave more similarly to the ferrite during the second cold rolling and the final anneal, *i.e.* it will show a promoted recrystallization. This could explain for the absence of martensite at the end of the DCR processing. The microstructure in a formerly martensitic region of the final DCR processed dual phase steel with a salt bath intermediate annealing time of 30 s is shown in Fig. 8.7. The fine precipitates visible in the micrograph have formed from the supersaturated ferrite after the intermediate anneal and might have slightly coarsened during the final anneal. Given that the final recrystallization anneal wipes off the dislocations, the dislocations tangled at the fine precipitates are likely quenched-in dislocations formed due to the thermal stresses generated during quenching to room temperature of the annealed sheet.

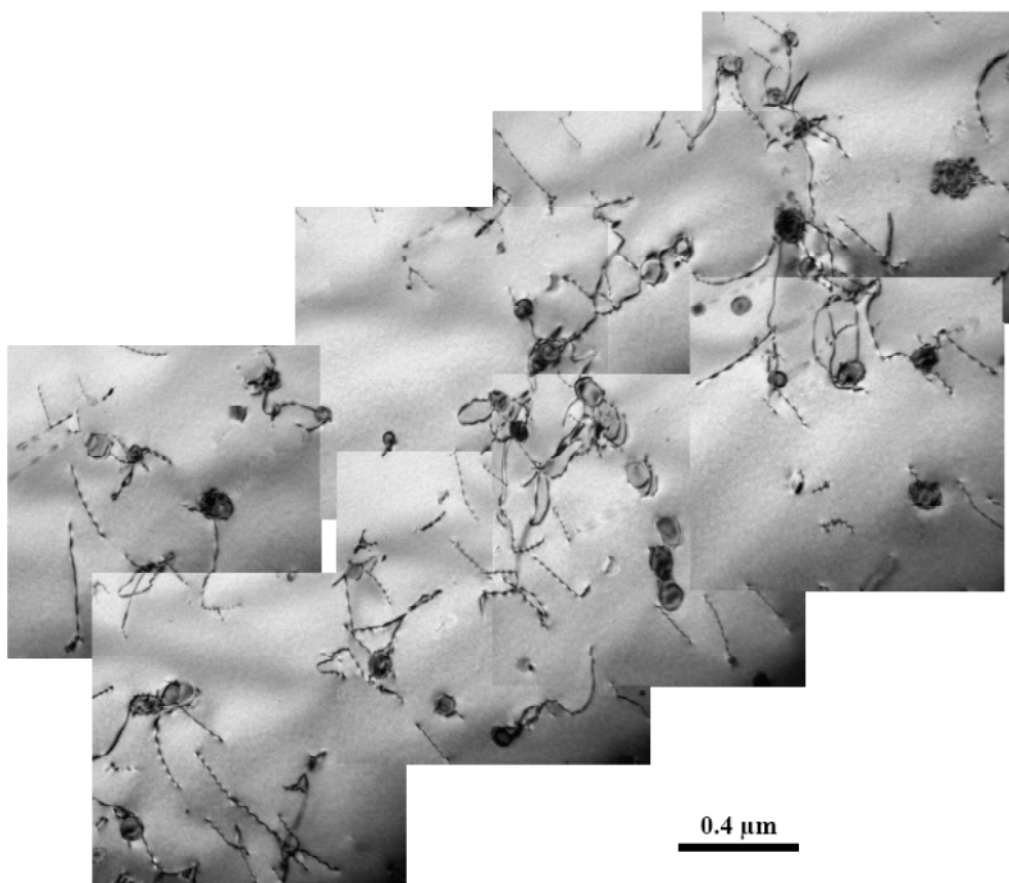


**Fig. 8.7.** TEM micrograph of the final DCR processed dual phase steel with an intermediate annealing of 30 s in a salt bath type furnace.

One of the striking differences in the texture of DCR processed sheets of ferritic and dual phase steels is the clearly higher intensity of the  $\gamma$ -fiber orientations in the dual phase steel (Fig. 8.4). The r-value results however indicate that the ferritic steel has higher mean r-values compared to the dual phase steel. This is in contrast to the general consensus that the r-value is proportional to the density of the  $\gamma$ -fiber oriented grains. The reason for this apparent discrepancy could be the influence of other texture components with relatively high intensities in the ODFs of both steels. Especially, the presence of  $\alpha$ -fiber oriented grains in the dual phase steel can counteract the high intensity of the  $\gamma$ -fiber.

An alternative mechanism to explain the lower r-values of the DCR processed dual phase steel is the following. The r-value is known to decrease with plastic strain when instantaneously measured in the tensile test. This is due to the reorientation of crystals which leads to activation of a larger number of dislocation glide systems. The fine precipitates present in the DCR processed sheets can pin the dislocations and limit the glide on the initially activated glide systems. This can accelerate the activation of less favorably oriented glide systems and decrease the r-value. Indeed, the contribution to the r-value of this mechanism decreases at longer intermediate annealing times which are associated with coarser precipitates.

Profilometry results for the final sheets are shown in Fig. 8.8. Considering the SCR processed sheets only, the dual phase microstructure shows a much better ridging resistance than the ferritic microstructure. This could be related to the effect that the martensite has on the material flow during the cold rolling. The formation of shear bands during cold rolling as discussed in chapter 7 is thought to be an important mechanism contributing to the superior ridging resistance of the dual phase steel. Since ridging originates from the presence of texture colonies as well as their type and geometrical arrangement, a texture close to random is desirable in view of the ridging resistance. Accordingly, the weaker texture of the SCR processed dual phase steel compared to the ferritic steel agrees with its better ridging resistance.

In the case of the ferritic steel, DCR with an intermediate annealing brings about an improved ridging resistance which is in agreement with other literature reports [1, 11]. The best ridging resistance was obtained when an intermediate annealing time in the box furnace of 30 s was applied. This intermediate annealing condition, on the other hand, was associated with the lowest r-value and the weakest  $\gamma$ -fiber intensity. Jung *et al.* [11] argue that ridging in ferritic stainless steels with texture bands parallel to RD increases as the intensity of the  $\gamma$ -fiber oriented grains increases, because of the significant difference in the flow properties of  $\gamma$ -fiber oriented matrix grains and differently oriented texture bands.

For the dual phase steel, transition to the DCR processing is accompanied by a decrease in the ridging resistance. This is due to the fact that the strain range over

which the hard martensite and soft ferrite coexist during cold rolling is larger for the SCR processed sheet of the dual phase steel because the intermediate annealing acts to recrystallize or recover the martensite and causes homogenous deformation in the second cold rolling step. In contrast to the ferritic steel where intermediate annealing for 5 hrs was associated with the lowest ridging resistance, increasing the box furnace intermediate annealing time for the dual phase steel improves the ridging resistance. This is in spite of the strong  $\gamma$ -fiber texture development in the dual phase steel annealed for 5 hrs in the box furnace. The more uniform distribution of  $\gamma$ -fiber grains is the most likely explanation for the good combination of ridging resistance and r-value in the dual phase steel intermediately annealed for 5 hrs.

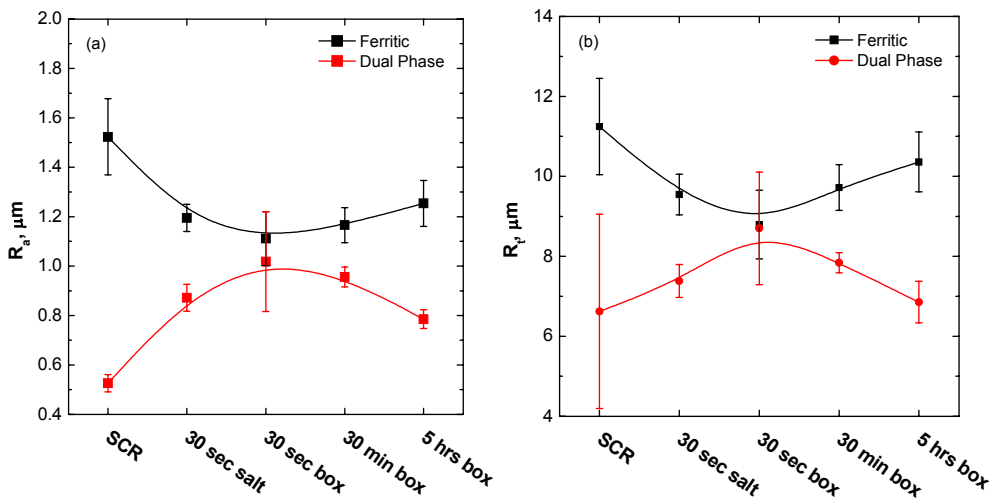


**Fig. 8.8.** Roughness parameters  $R_a$  (a) and  $R_t$  (b) for the differently processed ferritic and dual phase steels.

#### 8.4. Conclusions

Single step cold rolling and double step cold rolling with an intermediate annealing step processing routes were performed in the case of annealed hot rolled strips with two different microstructures denoted ferritic and dual phase. The ferritic steel had a fully ferritic matrix while the dual phase steel had a microstructure consisting of a ferritic matrix and approximately 25% of martensite. The following conclusions were drawn:



1- Single step cold rolled ferritic steel shows a higher mean r-value and a lower ridging resistance compared the similarly processed dual phase steel. The formation of shear bands during cold rolling and the incomplete recrystallization of martensite give rise to a weak texture in the dual phase steel with the consequence of a low r-value and a high ridging resistance.

2- Double step cold rolling of the ferritic steel improves both the ridging resistance and the mean r-value. In the dual phase steel, however, the double step cold rolling improves the r-value but deteriorates the ridging resistance. The negative impact on the ridging resistance of the double step cold rolled dual phase steel is related to the smaller strain range over which hard martensite and soft ferrite coexist during cold rolling.

3- In both initial microstructures, double step cold rolling results in a more uniform intensity distribution along the  $\gamma$ -fiber of ODF plots.

4- Both initial microstructures, especially the ferritic microstructure, were associated with high r-values at 90 ° to rolling direction after double step cold rolling which is related to the presence of grains belonging to the TD-fiber, notably the Goss texture component.

## 8.5. References

- [1] M. Y. Huh and O. Engler, "Effect of intermediate annealing on texture, formability and ridging of 17%Cr ferritic stainless steel sheet," *Materials Science and Engineering A*, vol. 308, pp. 74-87, 2001.
- [2] I. Jung, "Influence of the Cold Rolling Conditions on the Texture Development and Formability of Ti stabilized 18% Cr Ferritic Stainless Steel," MS, Graduate Institute of Ferrous Technology, POSTECH, Pohang, 2009.
- [3] B. C. De Cooman and J. G. Speer, *Fundamentals of Steel Product Physical Metallurgy*. Warrendale: Association for Iron and Steel Technology, 2011.

- [4] T. Tsuchiyama, *et al.*, "Recrystallization of Lath martensite with bulge nucleation and growth mechanism," *ISIJ International*, vol. 41, pp. 1047-1052, 2001.
- [5] M. Natori, *et al.*, "Difference in recrystallization behavior between lath martensite and deformed ferrite in ultralow carbon steel," *Scripta Materialia*, vol. 53, pp. 603-608, 2005.
- [6] S. Takaki, *et al.*, "Influence of cold working on recovery and recrystallization of lath martensite in 0.2%C steel," *Nippon Kinzoku Gakkaishi/Journal of the Japan Institute of Metals*, vol. 55, pp. 1151-1158, 1991.
- [7] R. K. Ray, *et al.*, "Transformation textures in steels," *ISIJ International*, vol. 34, pp. 927-942, 1994.
- [8] R. K. Ray, *et al.*, "Cold rolling and annealing textures in low carbon and extra low carbon steels," *International Materials Reviews*, vol. 39, pp. 129-172, 1994.
- [9] W. B. Hutchinson, "Recrystallisation textures in iron resulting from nucleation at grain boundaries," *Acta Metallurgica*, vol. 37, pp. 1047-1056, 1989.
- [10] H. Yan, *et al.*, "Effect of two-step cold rolling and annealing on texture, grain boundary character distribution and r-value of Nb + Ti stabilized ferritic stainless steel," *Materials Characterization*, vol. 60, pp. 65-68, 2009.
- [11] I. Jung, *et al.*, "Influence of the Cold Rolling and Annealing Sequence on the Ridging Behaviour of Ti-Stabilized 18% Cr Ferritic Stainless Steel," *Steel Research International*, vol. 81, pp. 1089-1096, 2010.
- [12] D. Muljono, *et al.*, "Influence of heating rate on anisothermal recrystallization in low and ultra-low carbon steels," *Materials Science and Engineering: A*, vol. 303, pp. 90-99, 2001.
- [13] M. Atkinson, "Bifurcation of thermal restoration processes in deformed iron and steel," *Materials Science and Engineering: A*, vol. 262, pp. 33-38, 1999.



# Chapter IX

## Quenching and Partitioning (Q&P) Processing of AISI 430

### 9.1. Introduction

Quenching and partitioning (Q&P) processing of low carbon steel is a relatively new concept to obtain a multi-phase steel microstructure containing retained austenite, and make use of the TRIP (transformation-induced plasticity) effect to achieve a high strength [1-3]. It is based on quenching austenite to a temperature below the martensite-start temperature ( $M_s$ ), commonly referred to as QT, followed by an isothermal hold at a partitioning temperature, PT, equal to or higher than the QT, to allow for the diffusion of C atoms from the supersaturated martensite into austenite, thereby stabilizing it against martensitic transformation during subsequent cooling to room temperature. The choice of the QT is of primary importance in obtaining the maximum attainable retained austenite fraction. Too high a QT leads to large fractions of austenite with insufficient C enrichment and stability after the partitioning step, and its subsequent transformation upon cooling to room temperature. On the other hand, when the QT is too low, the fraction of remaining austenite will be too low though it will show enough stability against the martensitic transformation during the final quenching step [4]. Appropriate alloying elements must be utilized to ensure that the competing carbide precipitation reactions, which can lead to C depletion, are suppressed. In TRIP steels, elements with limited solubilities in cementite, *i.e.* Si, Al,

and P, are added to suppress the cementite formation [1-7]. Some of the prospects for the Q&P process in comparison with the conventional austempering treatment of TRIP steels, in which bainitic ferrite formation causes the austenite enrichment, were reviewed by Speer *et al.* [1].

The AISI 430 type stainless steel is a widely used transformable ferritic grade composed of a ferritic matrix and embedded  $M_{23}C_6$  precipitates in the final sheet form. C and N are usually considered detrimental in most stainless steels as the former leads to sensitization during certain thermal cycles while the latter brings about static strain aging in the absence of strong nitride forming elements as Al and Ti. The present chapter reports on the applicability, by means of the C and N diffusion, of the Q&P process to a standard AISI 430 type stainless steel, to obtain a new type of multi-phase stainless steel.

## 9.2. Experimental Procedure

AISI 430 type ferritic stainless steel specimens with a standard composition were used for the Q&P processing. Dilatometry experiments were performed either in vacuum or in an Ar atmosphere. Since dimensional changes due to transformations are more noticeable in the normal direction (ND) of hot rolled products with a banded microstructure (chapter 4), 4 mm-diameter cylindrical dilatometry specimens with a length of 10 mm were machined parallel to the ND of rough rolled bars with a thickness of 30 mm. Dilatometry specimens were initially annealed for 5 minutes at 1000 °C to ensure full dissolution of  $M_{23}C_6$  precipitates. To minimize decarburization, the intercritical annealing time at 1000 °C was 5 seconds during which approximately 38% of austenite formed in the ferritic matrix. Estimation of the austenite fraction of Q&P processed sheet type dilatometry specimens was done by magnetic saturation measurements.

Specimens for Transmission Electron Microscope (TEM), Electron Backscattering Diffraction (EBSD), and tensile measurements were obtained from cold rolled sheets with a thickness of 0.6 mm after the following heat treatment cycle. Using a box type furnace, sheets were intercritically annealed at 1000 °C, quenched in an oil bath at

150 °C, and reheated to 400 °C in a salt bath, before air cooling to room temperature. Holding times in the box furnace, oil bath, and salt bath were 5 minutes, 30 minutes, and 30 minutes, respectively. TEM foils were prepared by mechanical polishing down to a thickness of 70 μm, followed by twin-jet polishing at a temperature of -5 °C. EBSD was used to estimate the austenite fraction in the Q&P processed sheet. To avoid the transformation of austenite due to mechanical polishing, a jet polished TEM foil was used for the EBSD measurement. Mechanical properties were measured using ASTM E8 standard tensile specimens. For comparison of mechanical properties with the Q&P processed sheet, one specimen was directly water quenched from 1000 °C after 5 minutes of holding to obtain a dual-phase microstructure composed of ferrite and martensite, and another an additional specimen was annealed for 5 hrs at 820 °C to obtain the conventional microstructure of AISI 430 type stainless steel consisting of a ferrite matrix with embedded  $M_{23}C_6$  precipitates.

### 9.3. Results and Discussion

The calculated pseudo-binary phase diagram of the steel studied is shown in Fig. 9.1. Austenite formation in the ferritic matrix takes place in the temperature range of 840-1240 °C. Whereas Thermo-Calc predicts a peak austenite fraction of 48% at about 950 °C, the image analysis results indicate that the austenite fraction reaches a maximum of only 38% in the vicinity of 1000 °C. The presence of substantial amounts of Cr, which is very effective at suppressing the formation of epitaxial ferrite during cooling from the intercritical annealing temperature [8-9], ensures that the room temperature martensite fraction is identical to the high temperature austenite fraction. Although both  $M_{23}C_6$  and  $Cr_2N$  precipitates are predicted to form in this steel, there is indication for the absence of  $Cr_2N$  even after prolonged annealing treatments in its stability range, which will be discussed later. Fig. 9.1 also shows schematically the microstructural evolution of the AISI 430 in the different steps of the Q&P processing. Fig. 9.2(a) shows the relative length change of a dilatometry specimen during direct and interrupted quenching to room temperature. The interruptedly quenched specimens were held at 160 °C for times of 1, 5, and 60 minutes prior to quenching to

room temperature. As soon as the temperature reaches 160 °C upon cooling, the specimen expands instantly due to the presence of a thermal gradient within the specimens. The temperature variations within the sample are estimated to be approximately 8 °C. After this initial expansion, the specimen size change remained close to zero which implies the absence of isothermal martensite formation. As the specimen continued to cool after each isothermal holding section at 160 °C, the martensitic transformation in the retained austenite was observed to occur at temperatures lower than 160 °C. Increased holding time at 160 °C resulted in a larger depression of the  $M_s$  temperature of the remaining austenite. The increased stability of untransformed austenite at longer holding times indicates the partitioning of C and N atoms from the supersaturated martensite into the austenite. The absence of other competing precipitation reactions is due to the very limited low temperature diffusivity of Cr which prevents the formation of carbides and nitrides and makes stainless steels ideal candidates for the application of the Q&P processing route. Whereas C is the only interstitial element of interest to stabilize austenite in TRIP steels, presence of high Cr levels in stainless steels increases the solubility limit of N [10-11] and allows for the utilization of the austenite stabilizing effect of N as well, without the use of any special nitriding technique. As Cr is also known to retard effectively the bainitic transformation [12], a constant austenite fraction before and after the partitioning treatment in the Q&P processed stainless steels is ensured.

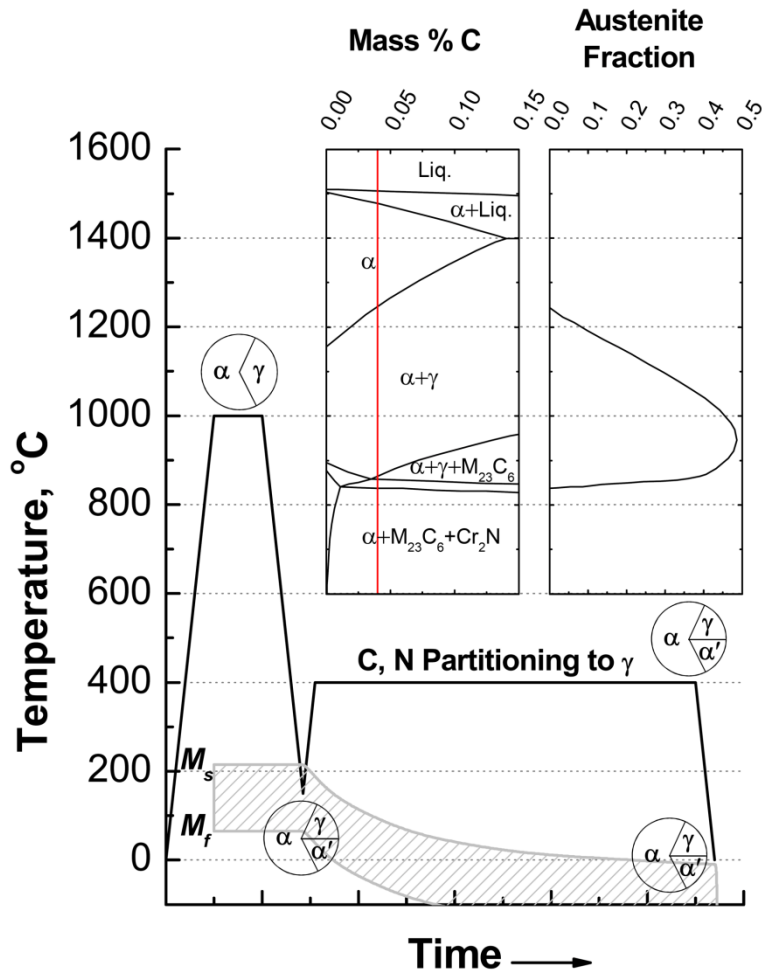


**Fig. 9.1.** Pseudo-binary Fe-C phase diagram and the austenite phase fraction profile for the 16%Cr stainless steel used in the present study superimposed on the schematic of the Q&P processing route. The C content of the steel was 0.04 mass-%.

The applicability of the Q&P concept to the AISI 430 stainless steel was further investigated by quenching an intercritically annealed dilatometry specimen to 160 °C prior to soaking for 1 minute at various partitioning temperatures in the range of 160-600 °C. The results of Fig. 9.2(b) indicate that as the partitioning temperature was increased in the range of 160-500 °C, the austenite stability also increased as evidenced by a lower transformation temperature for the remaining austenite and a smaller expansion. At the highest partitioning temperature, *i.e.* 600 °C, however, Cr



had enough mobility to form carbides and/or nitrides concurrent with the austenite enrichment. Therefore, the reduced stability of austenite after partitioning at 600 °C can be attributed to the partial stabilization of interstitials in the retained austenite. Fig. 9.2(c) shows the austenite fraction based on magnetic saturation measurements on dilatometry specimens Q&P processed at different quenching temperatures. At quenching temperatures below 160 °C, the austenite enrichment at the end of the partitioning treatment is large enough to suppress its transformation to martensite in the final cooling step. At quenching temperatures higher than 160 °C, the insufficient stability of the austenite after the partitioning step causes formation of fresh martensite in the final cooling step.

TEM examination of the Q&P processed sheet indicated the presence of a ferrite matrix, martensite, and retained austenite in the microstructure. Most of the austenite grains formed during intercritical annealing were found to have partially or fully transformed to internally twinned martensite. The TEM montage of Fig. 9.3(a) is an example of a twinned austenite grain containing multiple stacking faults. EBSD analysis (Fig. 9.3(b)) indicated the presence of about 6 vol.% of retained austenite in the microstructure of the specimen jet polished at -5 °C, where further transformation of austenite may have caused an underestimated austenite fraction. The untransformed austenite grains were found to have a smaller grain size than the transformed grains. The higher stability of fine-grained retained austenite is well known and it has been reported in TRIP steels [6-7].

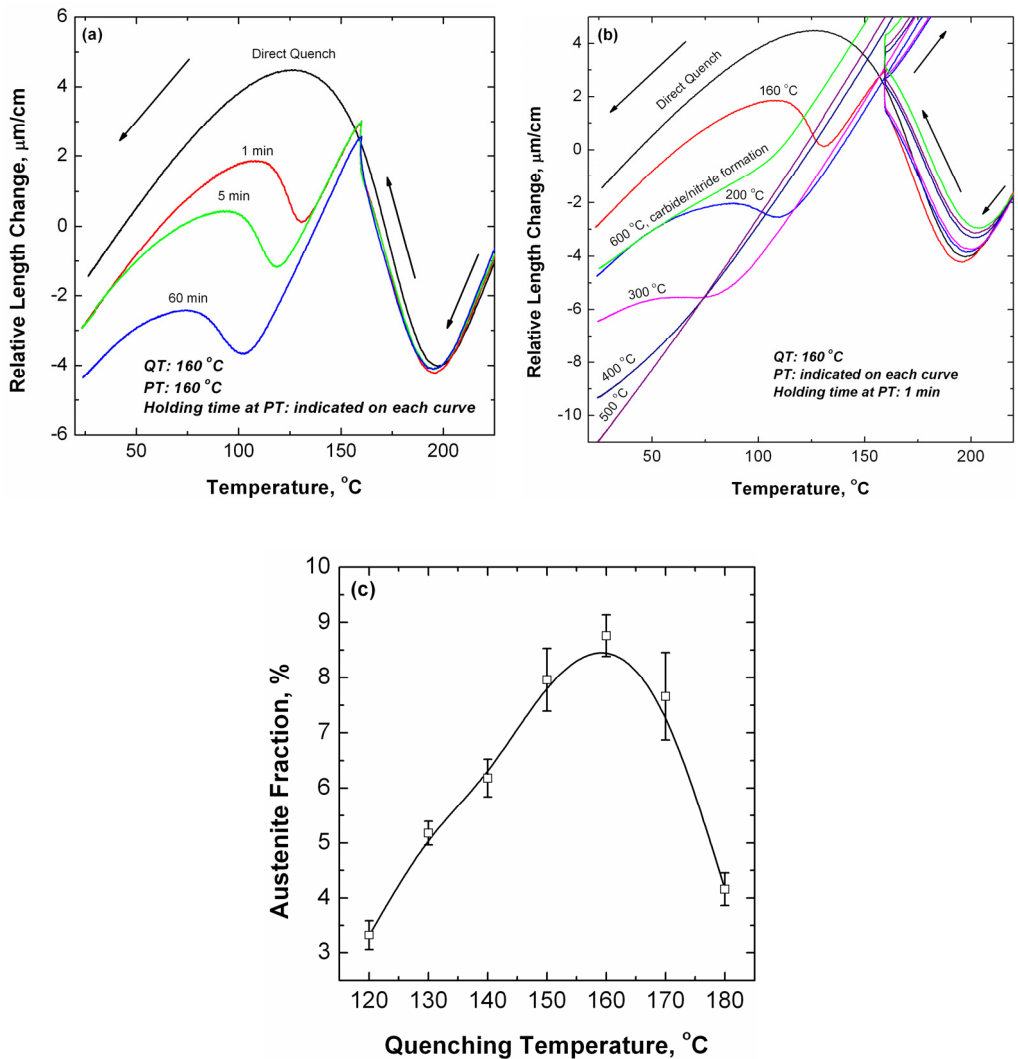


**Fig. 9.2.** (a) Relative length change during direct and interrupted quenching of a dilatometry specimen from 1000  $^{\circ}\text{C}$  to room temperature at a cooling rate of 10  $^{\circ}\text{C}/\text{s}$ . Isothermal holding at 160  $^{\circ}\text{C}$  for 1, 5, and 60 minutes was used for the interrupted quenching. (b) Dilatometry traces of specimens quenched from 1000  $^{\circ}\text{C}$  to 160  $^{\circ}\text{C}$  followed by soaking for 1 minute at the partitioning temperature indicated on each curve. (c) Austenite fraction in specimens quenched from 1000  $^{\circ}\text{C}$  to quenching temperatures in the range of 120-180  $^{\circ}\text{C}$  and partitioned at 450  $^{\circ}\text{C}$  for 5 minutes.

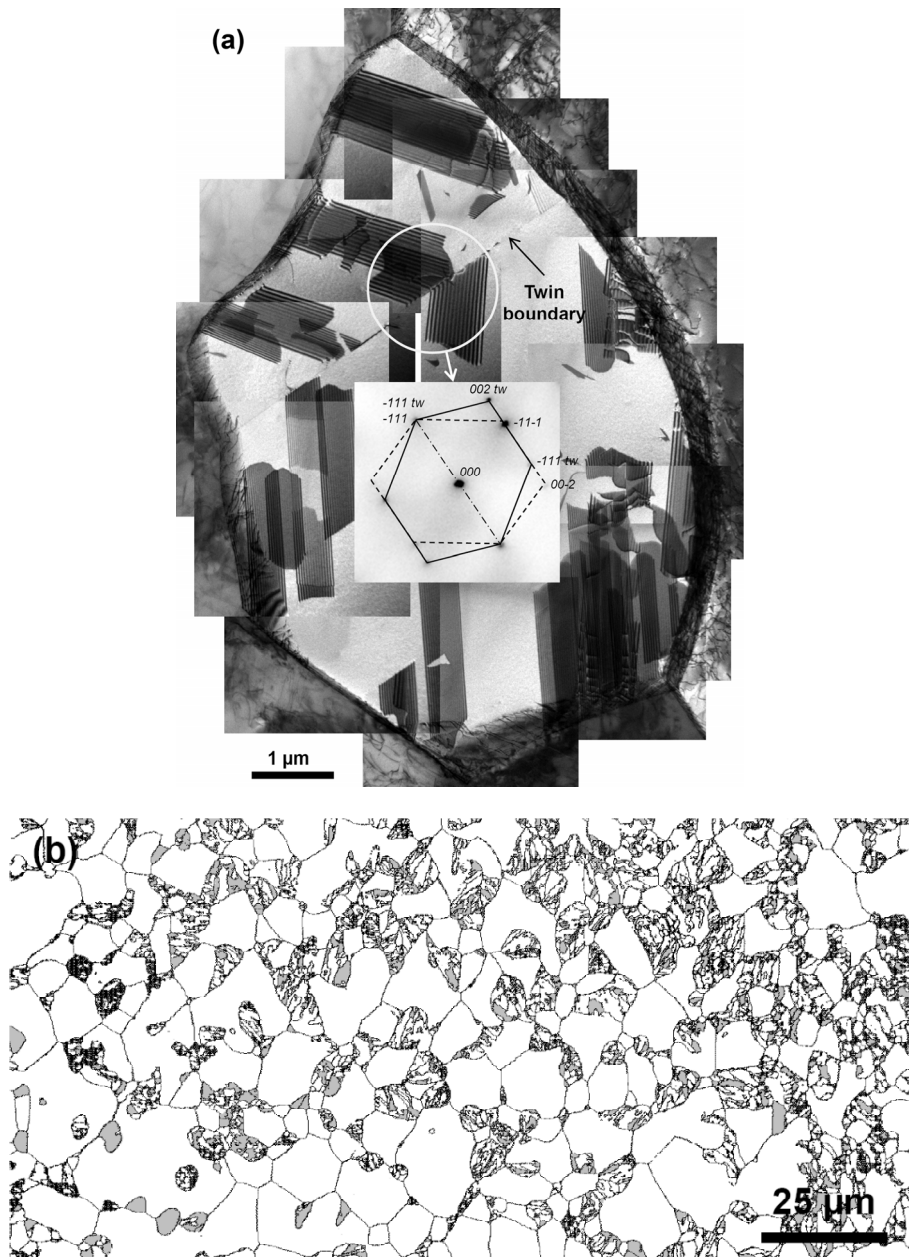


**Fig. 9.3. (a)** TEM microstructure showing a twinned grain of untransformed austenite containing wide stacking faults. The inset shows the Selected Area Diffraction (SAD) pattern taken parallel to the common  $\langle 110 \rangle$  zone axis of parent and twin. **(b)** EBSD map of a jet polished TEM specimen highlighting boundaries with misorientations larger than  $15^\circ$  in black and the austenite phase in gray.

Fig. 9.4 compares the tensile test results for Q&P processing, direct quenching, and after a conventional prolonged anneal at below the equilibrium austenite start temperature ( $A_{e1}$ ). The numbers next to each curve indicate the average work hardening exponent in the indicated engineering strain range. Compared to the direct quenching, the Q&P process results in a superior work hardening exponent at low strains and a more favorable combination of tensile strength and elongation. This is related to TRIP effect, the strain-induced transformation of the retained austenite to  $\alpha'$  martensite. The other difference in the stress-strain curves of the sheets lies in their yielding mode; whereas the conventionally processed specimen exhibits about 3% of yield elongation, there is no noticeable yielding discontinuity in the intercritically annealed specimens (direct quench and Q&P). Since C forms  $M_{23}C_6$  in the conventional sheet, the occurrence of static strain aging in the conventionally processed sheet can be attributed to the solute N. This is plausible because the addition of Al, a strong nitride former, reduces the strain aging significantly indicating that  $Cr_2N$  formation is unlikely even though the equilibrium phase diagram of Fig. 9.1 suggests its presence at below 850 °C. In the case of the directly quenched and the Q&P processed sheets, however, the partitioning of C and N to martensite and austenite respectively, leaves the ferritic matrix free of interstitials and eliminates the strain aging.

The retained austenite stabilized through Q&P processing has far higher C and N contents than the average steel composition. Assuming a zero solubility for C and N in the ferrite and martensite, stabilizing 10 vol.% of austenite is associated with a 10-fold increase of the C and N contents in the austenite. High N levels in turn facilitate the formation of  $Cr_2N$  which is a common occurrence in high nitrogen stainless steels [13-14]. Therefore, Q&P processing can potentially also be used as a pre-treatment to eliminate the static strain aging in the transformable ferritic stainless steels, if it is followed by an anneal below the  $A_{e1}$  temperature.

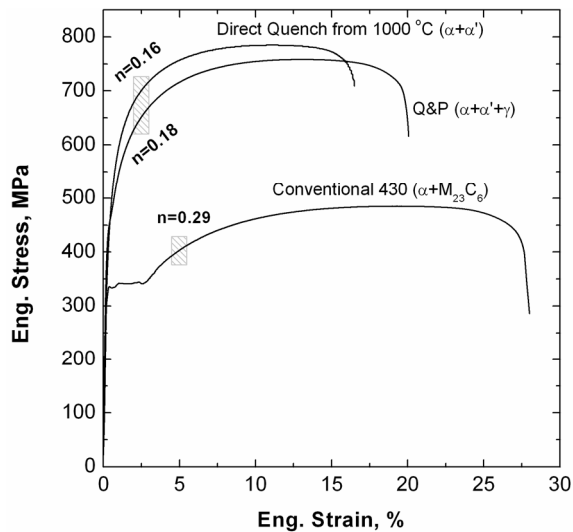


**Fig. 9.4.** Engineering stress-strain curves for quenched, Q&P processed, and conventionally processed AISI 430. The numbers indicate the work hardening exponent in the highlighted strain range.

#### 9.4. Conclusions

The applicability of the Q&P process to stainless steels was demonstrated using a transformable type of ferritic stainless steel. The presence of substantial amounts of Cr in stainless steels guarantees that, without any special alloying additions, enrichment of austenite with respect to C and N takes place, without other competing reactions, at temperatures as high as 500 °C. The concept can be extended to martensitic stainless steels where higher C levels will allow to stabilize even larger austenite fractions at room temperature. The presence of retained austenite in turn eliminates the static strain aging and its transformation upon deformation provides an additional contribution to the work hardening.

#### 9.5. References

- [1] J. Speer, *et al.*, "Carbon partitioning into austenite after martensite transformation," *Acta Materialia*, vol. 51, pp. 2611-2622, 2003.
- [2] J. G. Speer, *et al.*, "Partitioning of carbon from supersaturated plates of ferrite, with application to steel processing and fundamentals of the bainite

- transformation," *Current Opinion in Solid State and Materials Science*, vol. 8, pp. 219-237, 2004.
- [3] D. V. Edmonds, *et al.*, "Quenching and partitioning martensite--A novel steel heat treatment," *Materials Science and Engineering: A*, vol. 438-440, pp. 25-34, 2006.
- [4] J. G. Speer, *et al.*, "The "quenching and partitioning" process: Background and recent progress," *Materials Research*, vol. 8, pp. 417-423, 2005.
- [5] A. J. Clarke, *et al.*, "Carbon partitioning to austenite from martensite or bainite during the quench and partition (Q&P) process: A critical assessment," *Acta Materialia*, vol. 56, pp. 16-22, 2008.
- [6] L. Samek, *et al.*, "Influence of alloying elements on the kinetics of strain-induced martensitic nucleation in low-alloy, multiphase high-strength steels," *Metallurgical and Materials Transactions A: Physical Metallurgy and Materials Science*, vol. 37, pp. 109-124, 2006.
- [7] B. C. De Cooman, "Structure-properties relationship in TRIP steels containing carbide-free bainite," *Current Opinion in Solid State and Materials Science*, vol. 8, pp. 285-303, 2004.
- [8] D.-W. Suh, *et al.*, "Influence of Cr and Ni on Microstructural Evolution during Heat Treatment of Low-Carbon Transformation Induced Plasticity Steels," *Metallurgical and Materials Transactions A*, vol. 39, pp. 2015-2019, 2008.
- [9] M. Gomez, *et al.*, "The role of new ferrite on retained austenite stabilization in Al-TRIP steels," *ISIJ International*, vol. 50, pp. 139-146, 2010.
- [10] A. Poulalion and R. Botte, "Nitrogen addition in steelmaking using nitriding ferroalloys," in *High Nitrogen Steels*, Lille, France, 1988, pp. 49-52.
- [11] F. B. Pickering, "Some beneficial effects of nitrogen in steels," in *High Nitrogen Steels*, Lille, France, 1988, pp. 10-31.
- [12] B. C. De Cooman and J. G. Speer, *Fundamentals of Steel Product Physical Metallurgy*. Warrendale: Association for Iron and Steel Technology, 2011.

- [13] S. J. Kim, *et al.*, "Crystallographic features of Cr<sub>2</sub>N precipitation in high-nitrogen austenitic 18Cr-18Mn-2Mo-0.9N steel during isothermal aging at 900 °C," in *High Nitrogen Steels*, Ostend, Belgium, 2004, pp. 197-204.
- [14] D. Peckner and I. M. Bernstein, *Handbook of stainless steels*. New York: McGraw-Hill, 1977.





# Chapter X

## General Conclusions

1- A considerable length change anisotropy was observed during both the austenitization and the martensitic reactions of rough rolled bars of AISI 430 with a ( $\alpha+\alpha'$ ) banded microstructure. In the case of the martensitic transformation, dilatations along the ND were considerably larger than along the RD after quenching from the intercritical temperature range. Coefficient of thermal expansion (CTE) during cooling from the intercritical annealing temperature also showed a significant direction dependence, with CTEs measured along the RD smaller than those along the ND in the temperature range between the Curie temperature ( $T_c$ ) and the martensite start temperature ( $M_s$ ). The accumulation of thermal stresses due to the difference between  $CTE_\alpha$  and  $CTE_\gamma$  leads to the plastic yielding of  $\gamma$ -phase which is the minor phase because of a smaller volume fraction and a lower strength (below  $T_c$ ) compared to  $\alpha$ -phase.

2- Cold rolling of as-hot rolled strip with a banded microstructure consisting of  $\alpha$ -phase and  $\gamma$ -phase transformation products ( $\alpha$ ,  $M_{23}C_6$ , and  $\alpha'$ ) results in an improved ridging resistance compared to when annealed hot rolled strip with a homogenous microstructure of  $\alpha+M_{23}C_6$  is cold rolled. The presence of hard  $\gamma$ -phase transformation products including a small fraction of  $\alpha'$  during cold rolling facilitates the breakdown of untransformed  $\alpha$ -phase grains elongated in the RD.

3- The presence, during hot rolling, of the  $\gamma$ -phase, which has a higher strength than the  $\alpha$ -phase at high temperatures, is beneficial to the ridging resistance. The higher strains and strain rates applied to the  $\alpha$ -phase, as a result of the presence of the  $\gamma$ -phase, will promote its dynamic recrystallization and improve the ridging resistance. Not only the  $\gamma$ -phase fraction, but also its evolution during hot rolling, plays an essential role in the development of ridging. A small  $\gamma$ -phase fraction at the slab reheating temperature that increases considerably in the early stage of hot rolling is desirable. The  $\gamma$ -phase fraction evolution is very much controlled by the amount and the status of interstitial C and N atoms.

4- Presence of hard  $\alpha'$  during cold rolling enhances the ridging resistance of cold rolled and annealed sheets. No apparent evidence of grain colonies of any type was found when a hot strip containing about 35%  $\alpha'$  was cold rolled. Presence of hard  $\alpha'$  during cold rolling leads to shear band formation and thus fragmentation of elongated ferrite grains. Later on, recrystallization of this microstructure causes formation of fine grains with a weak texture which is favorable in view of the ridging resistance. Nevertheless, the associated r-values are not satisfactory.

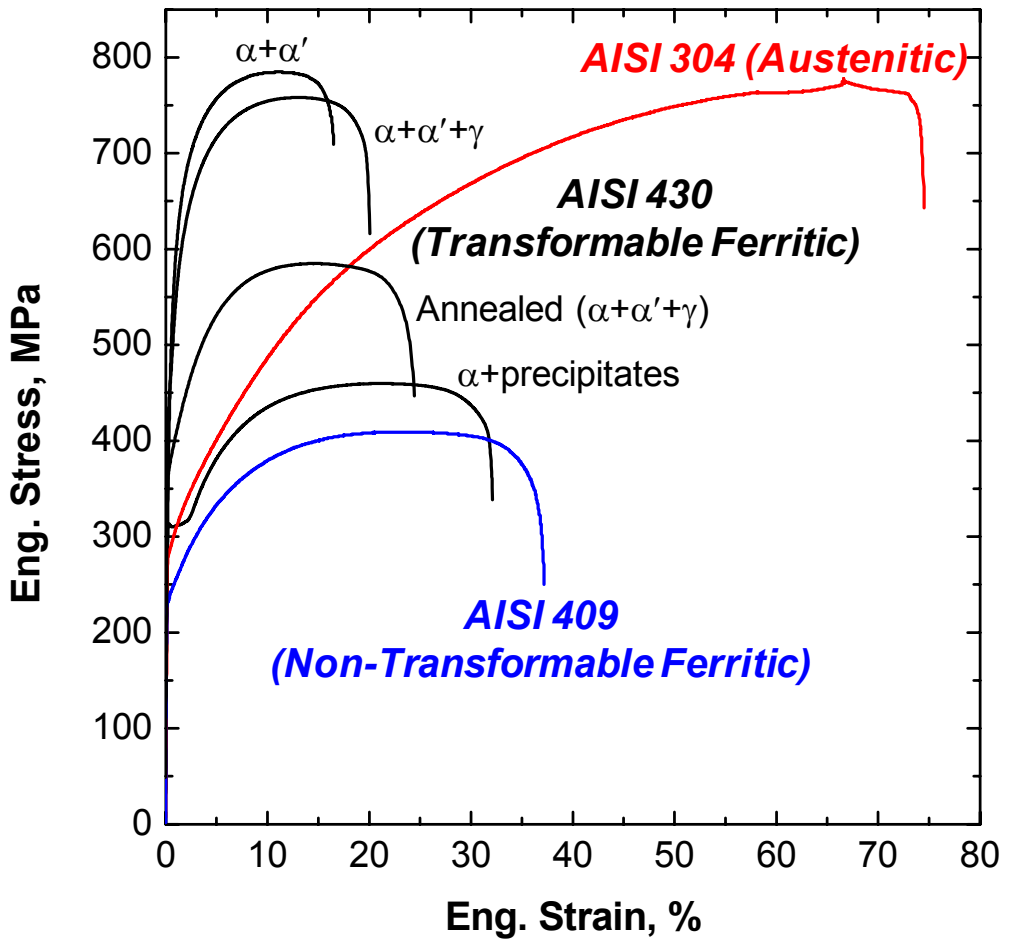
5- Double step cold rolling of hot strips containing  $\alpha'$  improves the r-value although associated with a decrease in the ridging resistance compared to the single step cold rolled sheets with an identical total reduction. The combination of ridging resistance and r-value in this case is, however, satisfactory.

6- The applicability of the Q&P process to stainless steels was demonstrated using the AISI 430. The presence of substantial amounts of Cr in stainless steels guarantees that, without any special alloying additions, enrichment of austenite with respect to C and N takes place, without other competing reactions, at temperatures as high as 500 °C. In contrast to carbon steel in which only C is used to enrich the austenite, the higher solubility of N in stainless steels allows to use both C and N to stabilize austenite at room temperature.

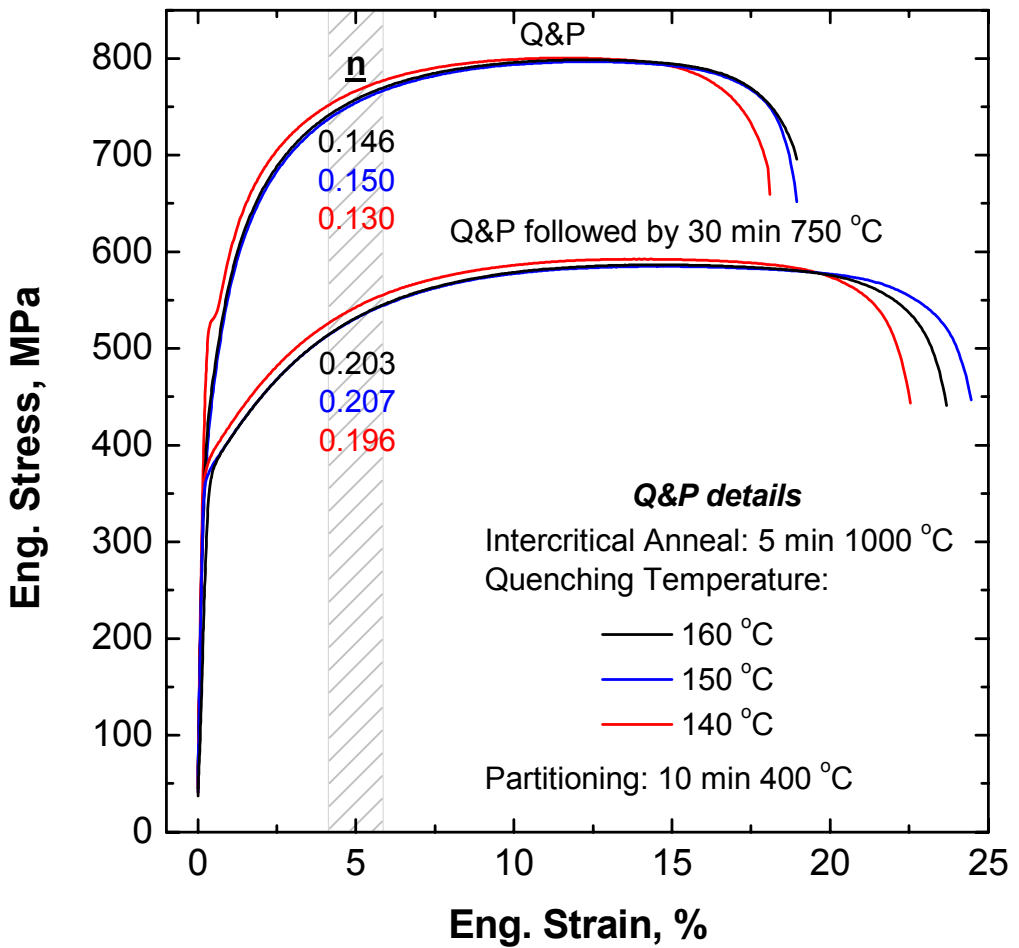


# Appendix

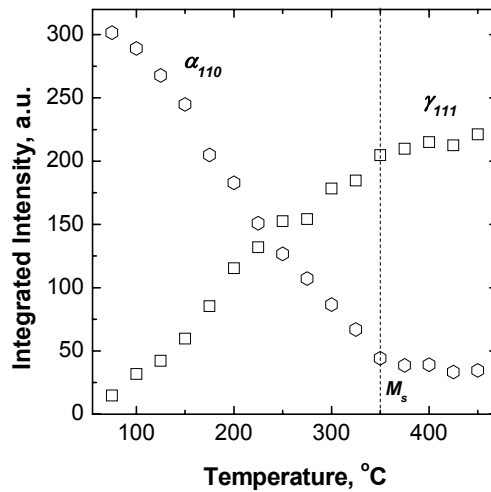
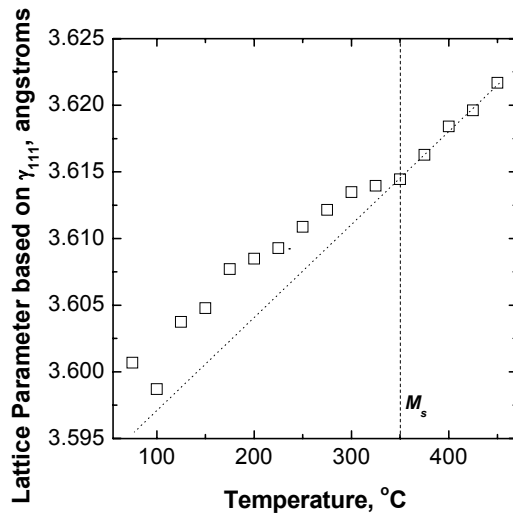
This appendix is intended to provide some of the research results which were not covered in the main chapters but might be of use for future reference.



**A1.** Comparison of stress-strain curves for the AISI 304 as the representative austenitic stainless steel grade and the ferritic stainless steel grades AISI 409 and AISI 430. The transformable ferritic stainless steel 430 can reach different strength levels depending on the microstructure.

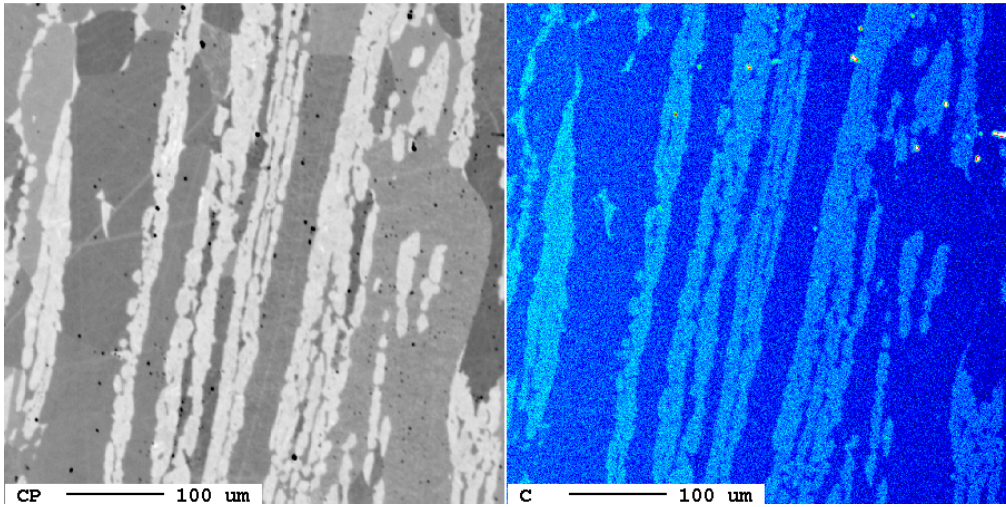


**A2.** Stress-strain curves for the AISI 430 grade sheets after Q&P processing at quenching temperatures of 140 °C, 150 °C, and 160 °C and after an additional 30 minute annealing at 750 °C.

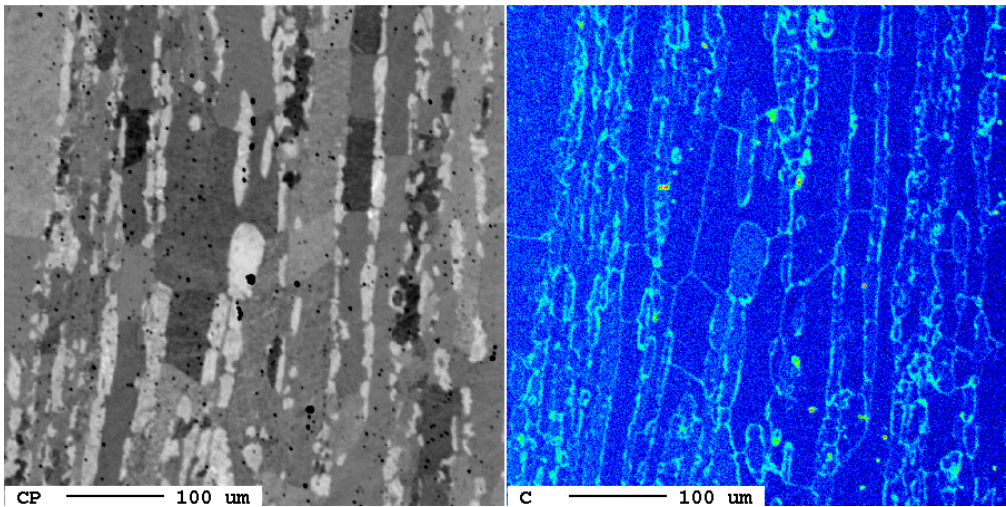


**A3.** In-situ XRD measurements on the polished RD plane of rough rolled bar of standard composition. Results are for a specimen soaked at 1000 °C for 5 minutes and cooled at a rate of 0.9 °C/s to 450 °C. The  $M_s$  temperature is higher than a dilatometry specimen quenched from 1000 °C which is because of precipitation during relatively slow cooling of XRD specimen which reduces the C and N content of the austenite. Below the  $M_s$  temperature, the lattice parameter of austenite decreases at a smaller rate which implies its enrichment with respect to C and N. Although  $\alpha$  is the dominant phase at all temperatures, its integrated intensity is low at temperatures above the  $M_s$  which could be related to the presence of surface oxides. The increase in the integrated intensity of  $\alpha_{110}$  below the  $M_s$  is due to the martensite formation.

2 min 1200 °C → Quenched to RT ↓

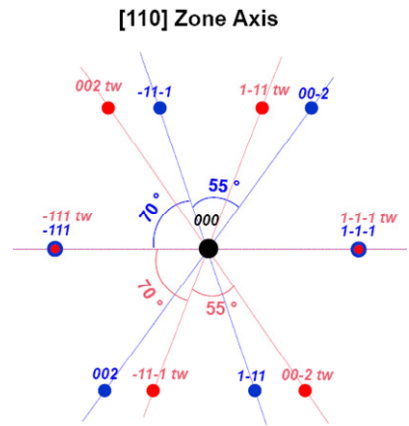
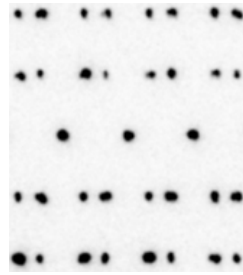
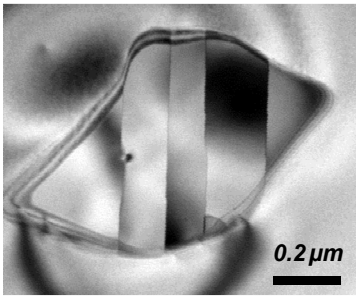


2 min 1200 °C → Quenched to 700 °C at soaked for 10 minutes → Quenched to RT ↓

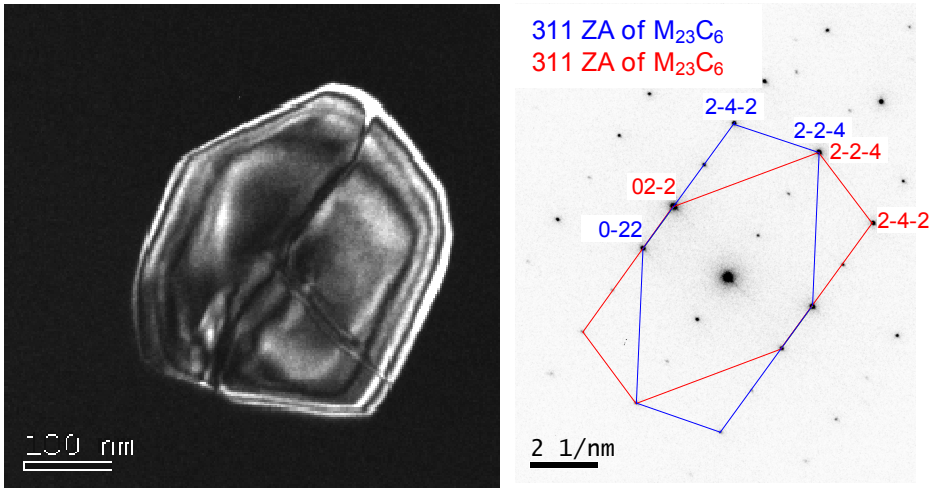


**A4.** EPMA maps showing the distribution of carbon in the rough rolled bar of Al-added composition after direct quenching and interrupted quenching from 1200 °C to RT. The C distribution in the  $\gamma$ -phase (bright) is very uniform in the sample directly quenched from 1200 °C to RT. Soaking at 700 °C results in the carbide formation which initiates in the  $\alpha$ - $\gamma$  phase boundaries and grain boundaries. The boundaries in the latter case are therefore decorated with carbides.

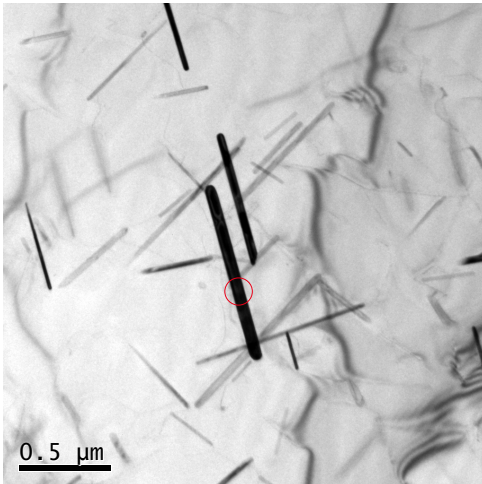




**A5.** TEM image and the corresponding SAD pattern parallel to the common  $\langle 110 \rangle$  zone axis of a twinned  $M_{23}C_6$  precipitate (M representing Cr and Fe) with an  $fm\bar{3}m$  space group and a lattice parameter of approximately 1.05 nm. The twin characteristics are similar to twins in fcc metals.



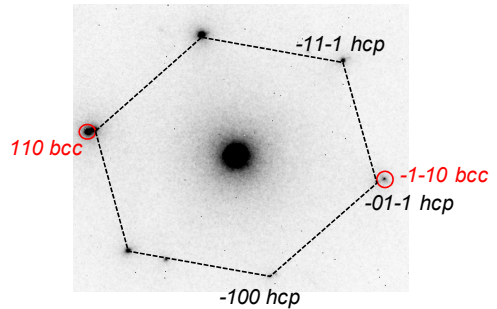
**A6.** TEM image and the corresponding SAD pattern parallel to the common  $\langle 311 \rangle$  zone axis of a twinned  $M_{23}C_6$  precipitate (M representing Cr and Fe) with an  $fm\bar{3}m$  space group. The twin characteristics are similar to twins in fcc metals.



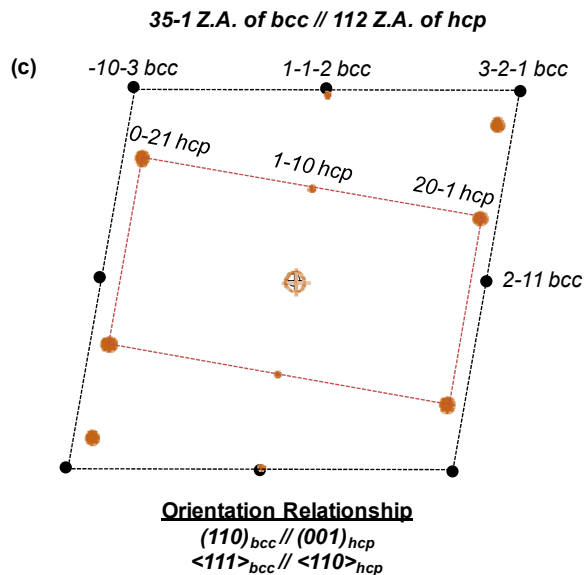
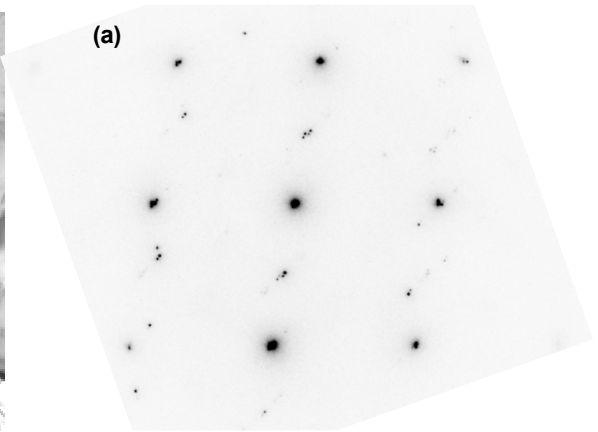
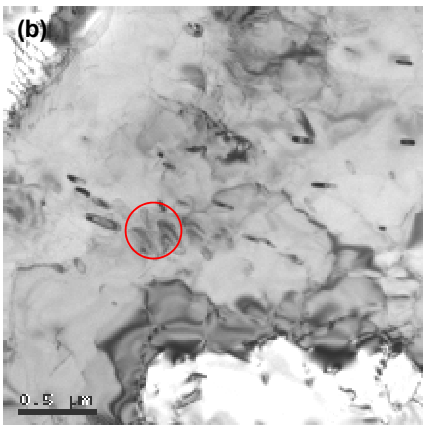
**Orientation Relationship**

$$(110)_{bcc} // (001)_{hcp}$$

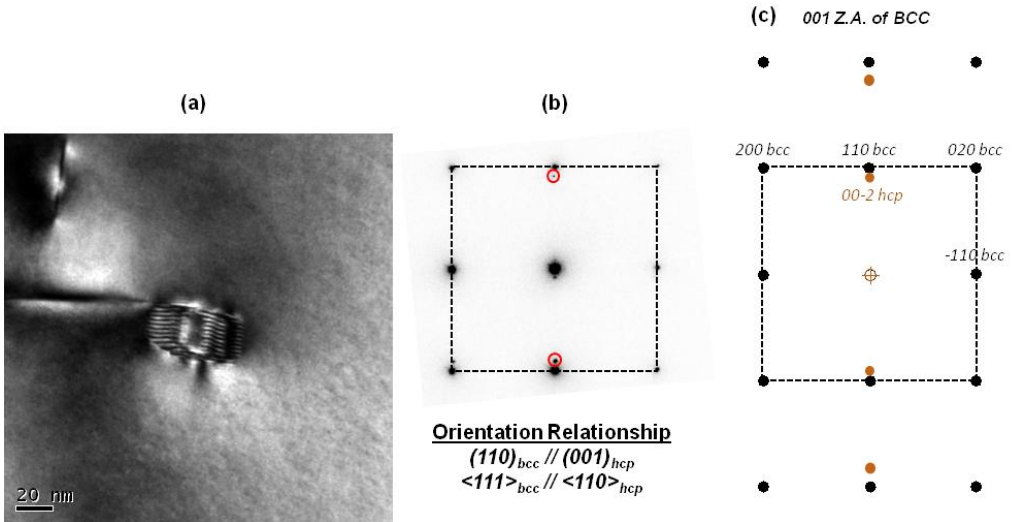
$$\langle 111 \rangle_{bcc} // \langle 110 \rangle_{hcp}$$



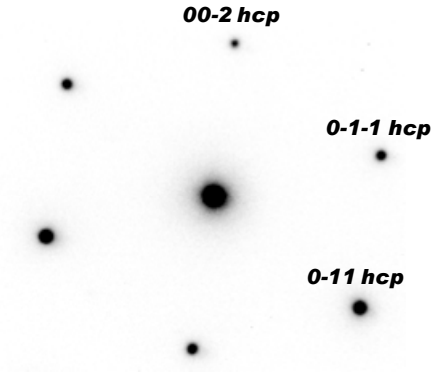
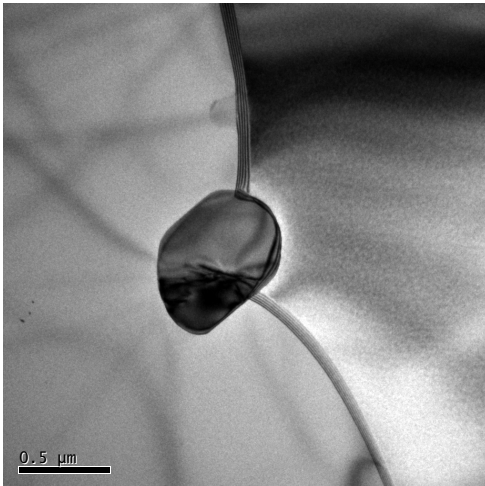
A7. Elongated chromium nitride precipitates with a hexagonal crystal system ( $a=b=0.274$  nm,  $c=0.444$  nm) formed in the ferrite phase after annealing for 30 minutes at  $750$  °C of a Q&P processed sheet containing approximately 8% austenite. The SAD pattern was taken parallel to the  $\langle 011 \rangle$  zone axis of the  $\text{Cr}_2\text{N}$ . The indicated orientation relationship was found between the bcc ferrite and the hexagonal  $\text{Cr}_2\text{N}$ .



**A8.** (a) Chromium nitride precipitates with a hexagonal crystal system ( $a=b=0.274$  nm,  $c=0.444$  nm) formed in the ferrite phase after annealing for 30 minutes at  $750$  °C of a Q&P processed sheet containing approximately 8% austenite. (b) SAD pattern of the encircled area in the BF image of (a). It can be used to specify the orientation relationship between the ferrite and the  $\text{Cr}_2\text{N}$  precipitates in the frame. The simulated SAD pattern on the basis of the indicated orientation relationship between the hexagonal  $\text{Cr}_2\text{N}$  and bcc ferrite is shown in (c). Based on the literature data, the space group of  $\text{Cr}_2\text{N}$  was assumed to be  $P6_3/mmc$  for the simulation. The extra spots in the experimental SAD pattern must have arisen due to double diffraction.



**A9.** (a) A chromium nitride precipitate with a hexagonal crystal system ( $a=b=0.274$  nm,  $c=0.444$  nm) formed in the ferrite phase after annealing for 30 minutes at  $750^\circ\text{C}$  of a Q&P processed sheet containing approximately 8% austenite. (b) SAD pattern of the  $\text{Cr}_2\text{N}$  precipitate and the ferritic matrix. The simulated SAD pattern on the basis of the indicated orientation relationship between the hexagonal  $\text{Cr}_2\text{N}$  and bcc ferrite is shown in (c).



**A10.** A coarse chromium nitride with a hexagonal crystal system ( $a=b=0.274$  nm,  $c=0.444$  nm) and its corresponding SAD pattern. This was found in the microstructure of a conventionally processed AISI 430. This direct observation of  $\text{Cr}_2\text{N}$  was made in the final stage of this project and proved that the  $\text{Cr}_2\text{N}$  can form during batch annealing of industrial products. However, it probably does not lead to total depletion of N because unless Al (or other strong nitride former) is added, the static strain aging in the final recrystallized sheets of the AISI 430 will remain large (of the order of 3%) which is likely related to the solute N.

## Acknowledgements

It was a real privilege to work under supervision of Prof. Bruno De Cooman who continuously supported my research and study by his immense knowledge. He helped me get the most out of my PhD studies and inspired me to set more ambitious goals. His lessons for me were not just about steels but also about life.

Support of the stainless steel research group of POSCO, particularly Dr Dongchul Chae with whom I had many fruitful discussions, is sincerely acknowledged. My thanks also go to Dr Jieon Park for his time and help.

I would like to give thanks to former and present MDL professors namely, Prof. Han-Soo Kim, Prof. Sam-Kyu Chang, and Prof. Seok-Jae Lee. Thanks are also due to those professors who taught me in the GIFT curriculum.

I extend my thanks to Prof. Sung-Joon Kim, Prof. Jae Sang Lee, and Prof. Dong-Woo Suh for serving on my thesis committee.

Thank you to my fellow MDL labmates and GIFT friends. Ilchan Jung was a big help to my research scientifically and helped me in many of the experiments. Assistance of Eunjung Seo in the Q&P part of my research is also appreciated. I would also like to acknowledge the help, during his internship period in MDL, of Alnahyan Damang Tohir from Institut Teknologi Bandung.

I would like to extend my thanks to the GIFT technical staff especially Mr Keun Chang Park in RFC and Mr Tae Yong Park in MDL for their technical support.

Last but not the least, I thank my family especially my wife, Solmaz, who was always there for me and who had the huge responsibility of looking after our baby alone when I was at work.

Finally, though nothing compared to their care and support, I dedicate this work to my wife, my mother, and to the memory of my father.

## Publications

### Journals

J. Mola, B.C. De Cooman, 'Quenching and partitioning processing of transformable ferritic stainless steels', *Scripta Materialia* (2011), doi:10.1016/j.scriptamat.2011.07.041

J. Mola, I. Jung, J. Park, D. Chae, B.C. De Cooman, 'Ridging Control in Transformable Ferritic Stainless Steels', *Metallurgical and Materials Transactions A* (2011), DOI: 10.1007/s11661-011-0824-7

J. Mola, D. Chae, B.C. De Cooman, 'Dilatometric Analysis of Anisotropic Dimensional Changes in a 16 Pct Cr Stainless Steel with a Planar Banded Structure', *Metallurgical and Materials Transactions A* (2010), Vol. 41, pp. 1429-1440.

I. Jung, J. Mola, D. Chae, B.C. De Cooman, 'Influence of the cold rolling and annealing sequence on the ridging behaviour of Ti-stabilized 18% Cr ferritic stainless steel', *Steel Research International* (2010), 81 (12), pp. 1089-1096

### International Conferences

J. Mola, D. Chae, B.C. De Cooman, 'Influence of texture on ridging and formability of 16%Cr ferritic stainless steel', *Solid State Phenomena* (2010), Vol. 160, pp. 153-158.

J. Mola, E. Seo, I. Jung, J. Park, B.C. De Cooman, 'Cold rolling of  $\alpha+\alpha'$  dual-phase microstructure in transformable ferritic stainless steel', *7<sup>th</sup> European Stainless Steel Conference*, Como, Italy, Sept. 2011.

J. Mola, J. Park, B.C. De Cooman, 'Recrystallization behavior of  $\alpha'$  martensite in transformable ferritic stainless steels', *7<sup>th</sup> European Stainless Steel Conference*, Como, Italy, Sept. 2011.



# Curriculum Vitae

**Name:** Javad Mola

**Date of Birth:** Aug. 11<sup>th</sup>, 1981

**Place of Birth:** Neyshaboor, Iran

**Address:** Materials Design Laboratory, Graduate Institute of Ferrous Technology,  
POSTECH San 31, Hyoja-dong, Nam-gu, Pohang, Gyeongbuk 790-784, South Korea

## Academic Information:

- |                 |  |
|-----------------|--|
| 2008.03-2011.12 | Doctoral Degree<br>Graduate Institute of Ferrous Technology (GIFT)<br>Pohang University of Science and Technology (POSTECH)<br>Pohang, South Korea |
| 2006.09-2008.3  | Withdrawn Doctoral Program<br>School of Metallurgy & Material Engineering<br>University of Tehran<br>Tehran, Iran                                  |
| 2003.09-2006.01 | Master's Degree<br>Materials Science and Engineering Department<br>Sharif University of Technology<br>Tehran, Iran                                 |
| 1999.09-2003.09 | Bachelor's Degree<br>Materials Engineering Department<br>Isfahan University of Technology<br>Isfahan, Iran   |